On the Connection Between Zonal Current Variability and Oxygen Supply of the Eastern Tropical North Atlantic Focussing on the North Equatorial Undercurrent

Dissertation

zur Erlangung des Doktorgrades

der Mathematisch-Naturwissenschaftlichen Fakultät
der Christian-Albrechts-Universität zu Kiel

vorgelegt von

Kristin Burmeister

Kiel, 2019

Erste Gutachterin:	Prof. Dr. Joke F. Lübbecke
Zweiter Gutachter:	Prof. Dr. Arne Biastoch

Tag der mündlichen Prüfung: 9. September 2019

Abstract

The upwelling regions in the eastern tropical Atlantic and Pacific are co-located with zones of oxygen-poor water masses at intermediate depth. The so-called Oxygen Minimum Zones (OMZs) are a consequence of high biological productivity combined with weak ventilation. Within the last few decades, an expansion of the OMZs was observed. Until now it is unclear to what extent variations of the OMZs are attributed to the anthropogenic climate change or to the natural variability of the climate system. This thesis examines changes of the ventilation of the OMZ in the Eastern Tropical North Atlantic (ETNA) focusing on the variability of the North Equatorial Undercurrent (NEUC). The NEUC has been suggested to act as an important oxygen supply route of the ETNA OMZ. Observational estimates of the mean NEUC strength are uncertain due to the presence of elevated mesoscale activity and models have difficulties in simulating a realistic NEUC. This thesis investigates the intraseasonal to multidecadal variability of the NEUC and its impact on oxygen concentrations in the ETNA based on both, observational data and model output. An unique data set of 24 meridional ship sections and multiyear moored observations along 23°W is used. Furthermore, this thesis analyses the output of a high-resolution Ocean General Circulation Model (OGCM) and performs experiments with a conceptual model.

For the first time a multiyear NEUC transport time series is reconstructed from direct velocity observations at about 5°N, 23°W. In contrast to previous studies that were mainly based on model output or hydrographic data, hardly any seasonal cycle of NEUC transports can be found. The NEUC transport variability is instead dominated by sporadic intraseasonal events. Both, observations and model output suggest that, on intraseasonal to interannual time scales, a stronger NEUC is not necessarily associated with a higher oxygen supply of the eastern basin. Idealized experiments with the conceptual model suggest that the impact of NEUC variability on oxygen depends on the pathway of its source waters. A strengthening of the NEUC supplied out of the western boundary acts to increase oxygen levels within the NEUC. A strengthening of the NEUC driven by enhanced recirculations within the ocean interior results in a reduction of oxygen levels within the NEUC. This is supported by the moored velocity and oxygen observations. Only some of the observed intraseasonal events are associated with high oxygen levels suggesting an occasional eastward oxygen supply by NEUC transport events. Nevertheless, they are found to be responsible for the local

oxygen maximum in the mean shipboard section along 23°W at the NEUC core position. Finally the decadal to multidecadal variability of the NEUC and its impact on oxygen is investigated. Keeping in mind that a change of the NEUC transport has not been observed throughout the last decade, the results of the OGCM and the conceptual model indicate that a change in the large-scale wind field on decadal to multidecadal time scales may lead to a NEUC transport variability and associated changes of the ventilation of the ETNA OMZ.

Zusammenfassung

Unterhalb der Auftriebsgebiete im östlichen tropischen Atlantik und Pazifik befinden sich Zonen mit sauerstoffarmen Wassermassen. Diese sogenannten Sauerstoffminimumzonen (OMZs) resultieren aus einem hohen Sauerstoffverbrauch auf der einen Seite und einer schwachen Ventilation auf der anderen Seite. Während der letzten Jahrzehnte wurde beobachtet, dass sich die OMZs ausbreiten. Bis jetzt ist unklar, in welchem Umfang die Änderung der OMZs mit dem anthropogenen Klimawandel oder mit der natürlichen Variabilität des Klimasystems zusammenhängt. Diese Arbeit untersucht die Variabilität der Ventilation der OMZ im östlichen tropischen Nordatlantik (ETNA) und nimmt dabei die Variabilität des nördlichen äquatorialen Unterstroms (NEUC) in den Fokus. Vorherige Studien deuten an, dass der NEUC eine wichtige Rolle für die Sauerstoffversorgung der ETNA OMZ spielt. Abschätzungen der mittleren Stärke des NEUCs aus Beobachtungen sind wegen der Präsenz erhöhter mesoskaliger Aktivität unsicher und Modelle haben Schwierigkeiten den NEUC realistisch zu simulieren. Diese Arbeit untersucht die intrasaisonale bis multidekadische Variabilität des NEUCs und die dadurch resultierenden Auswirkungen auf die Sauerstoffkonzentrationen im ETNA. Die Analyse basiert auf einem einzigartigen Datensatz bestehend aus 24 meridionalen Schiffsschnitten sowie mehrjährigen Verankerungsdaten entlang 23°W und Modelldaten eines allgemeinen Ozeanzirkulationsmodelles. Des Weiteren werden Experimente mit einem konzeptionellen Modell ausgeführt.

Zum ersten Mal wird eine Transportzeitserie des NEUCs aus direkt gemessenen Geschwindigkeitsdaten rekonstruiert. Im Gegensatz zu vorherigen Studien, die hauptsächlich auf Modelldaten oder hydrographischen Daten basieren, zeigt die hier rekonstruierte NEUC-Transportzeitserie kaum Anzeichen eines saisonalen Zyklus. Stattdessen ist die Variabilität des NEUC-Transportes dominiert von intrasaisonalen, ostwärts gerichteten Transportereignissen. Sowohl in den Beobachtungen als auch in den Modelldaten geht ein stärkerer NEUC auf intrasaisonaler bis interannualer Zeitskala nicht zwangsläufig mit höheren Sauerstoffwerten einher. Idealisierte Experimente mit dem konzeptionellen Modell suggerieren, dass der Einfluss der Stärke des NEUCs auf den Sauerstoffgehalt vom zurückgelegten Weg seiner Wasserzufuhr abhängt. Wenn eine Verstärkung des NEUCs mit einer erhöhten Wasserversorgung aus der westlichen Randregion des Atlantiks hervorgeht, ist ein höherer Sauerstoffgehalt innerhalb des NEUCs zu finden.

Verstärkt sich der NEUC dagegen durch erhöhte Rezirkulationen mit dem Ozeaninneren, werden sauerstoffärmere Wassermassen innerhalb des NEUCs nach Osten transportiert. Dies wird durch die verankerten Geschwindigkeits- und Sauerstoffbeobachtungen bestätigt. Die beobachteten intrasaisonalen Transportereignisse sind nur teilweise mit erhöhten Sauerstoffkonzentrationen verbunden was eine gelegentliche Sauerstoffversorgung des Ostens durch den NEUC andeutet. Nichtsdestotrotz scheinen diese Ventilationsereignisse für das lokale Sauerstoffmaximum im mittleren Schiffsschnitt im Bereich des NEUC-Kerns verantwortlich zu sein. Abschließend wird die Auswirkung einer dekadischen bis multidekadischen Variabilität des NEUCs auf die Sauerstoffversorgung der ETNA OMZ untersucht. Die Analyse basiert auf Modelldaten des allgemeinen Ozeanzirkulationsmodelles sowie Experimenten mit dem konzeptionellen Modell. Die Ergebnisse suggerieren, dass auf dekadischen bis multidekadischen Zeitskalen eine Variation des großskaligen Windfeldes im tropischen Atlantik zu einer Variabilität des NEUCs führen kann, welche mit Änderungen der Ventilation des östlichen Beckens einhergeht. Allerdings konnte während den letzten zehn Jahren in den Beobachtungen keine solche Veränderung des NEUC-Transportes festgestellt werden.

Contents

List of Figures **vi**

List of Tables **viii**

List of Abbreviations **x**

1 Motivation and Study Aim **1**

2 Scientific Background **4**

2.1 Important Momentum Balances and Conservation Concepts 4

2.2 Upper tropical Atlantic circulation 7

2.3 Tropical Atlantic variability 9

2.4 Oxygen minimum zones 13

2.5 The North Equatorial Undercurrent 16

2.5.1 Flow characteristics and variability 16

2.5.2 Potential driving mechanisms 18

3 Interannual variability of the Atlantic NEUC and its impact on oxygen 20

3.1 Introduction 22

3.2 Data and Methods 27

3.2.1 Observations 27

3.2.2 High-resolution global ocean circulation model TRATL01 28

3.2.3 NEUC characterization 29

3.2.4 Conceptual model 30

3.3 Results 32

3.3.1 Mean velocity and oxygen section along 23°W 32

3.3.2 Seasonal cycle of NEUC intensity (INT) and central position (Y_{CM}) 35

3.3.3 Interannual variability of NEUC 38

3.3.4 NEUC impact on oxygen 41

3.3.5 Conceptual model 47

3.4 Discussion and Conclusion 53

3.5 SI for "Variability of the Atlantic NEUC and its impact on oxygen" . . 58

4 Reconstructed NEUC transport at 5°N, 23°W 62

4.1 Introduction 64
4.2 Data 65
4.3 Observed velocity variability at 5°N, 23°W 65
4.4 NEUC transport estimates at 23°W 66
4.5 NEUC variability 68
4.6 NEUC and oxygen 70
4.7 Summary and Discussion 71
4.8 SI for "Ventilation of the ETNA by intraseasonal flow events of the NEUC" 75
4.9 Excursus: Resonant equatorial basin modes & zonal velocities at 5°N, 23°W 88
4.9.1 Shallow Water Model 88
4.9.2 Deriviation of the wind stress projection coefficients 90
4.9.3 Results 93
4.9.4 Summary and Discussion 93

5 Decadal to mulditdecadal variability of the NEUC 96

5.1 Introduction 96
5.2 Data and Methods 98
5.3 Results 99
5.3.1 Multidecadal variability NEUC 99
5.3.2 Conceptual model 101
5.4 Summary and Discussion 105

6 Synthesis 108

6.1 Scientific progress and its integration in the current state of research . . 108
6.2 Outlook 113

Bibliography I

Acknowledgments XVII

Declaration XIX

List of Figures

1.1 Oxygen distribution and main wind-driven currents in the tropical Atlantic 2

2.1 Large-scale wind field and wind-driven gyres 6
2.2 Mean ship sections of zonal velocity and oxygen 14

3.1 Oxygen distribution and main wind-driven currents in the tropical Atlantic 24
3.2 Observed and modelled meridional velocity and oxygen sections along 23°W 33
3.3 Hovmöller diagram of seasonal variability of NEUC intesity and central position in TRATL01 36
3.4 Zonally averaged anomalies of NEUC intensity and central position in TRATL01 - interannual variability 39
3.5 Linear regression of NEUC intensity onto wind stress curl 40
3.6 SST and wind stress composites for strong and weak NEUC intensity in TRATL01 42
3.7 Mean oxygen concentrations and horizontal velocities along density surfaces in TRATL01 44
3.8 Composites of anomalous oxygen concentrations and horizontal velocity for strong and weak NEUC intensities in TRATL01 45
3.9 Linear regression of oxygen concentrations on NEUC intensity in TRATL01 47
3.10 Mean oxygen distribution simulated by experiments SIM1 and SIM2 of the conceptual model 50
3.11 Amplitude and phase of oxygen variability simulated by the experiments VAR 1-3 of the conceptual model 51
3.S1 Meridonal (23°W) and zonal (4.5°N) oxygen section simulated by the experiments SIM 1-2 of the conceptual model 58
3.S2 Atlantic Meridional Mode index and oxygen anomalies derived from ship sections 59
3.S3 Amplitude and phase of oxygen variability simulated by the modified VAR 2 experiment of the conceptual model (stronger recirculation) . . 60

3.S4 Amplitude and phase of oxygen variability simulated by the modified VAR 2 experiment of the conceptual model (variable mean flow) 61

4.1 Moored velocity observations at 5°N, 23°W 67
4.2 Reconstructed NEUC transport time series at 5°N, 23°W 69
4.3 Meridional ship sections along 23°W 70
4.4 Moored oxygen observations at 5°N, 23°W 71
4.S1 Zonal velocity observations from three moorings located between 4.5°N and 5°N as well as 22.4°W and 23.4°W 81
4.S2 Validation of NEUC transport estimation 82
4.S3 Patterns of the first four HEOFs of shipboard zonal velocity sections between 4.25°N and 5.25°N 83
4.S4 NEUC transport at 23°W calculated by different methods 84
4.S5 Patterns of the first four HEOFs of shipboard zonal velocity sections between 3.5°N and 6.0°N 85
4.S6 Linear regression of wind stress curl onto NEUC transports 86
4.S7 Composite Hovemöller diagrams of anomalous zonal wind stress and SLA 87
4.E1 Modal energy and phase of the first five baroclinic modes derived from moored zonal velocities at 0°, 23°W 92
4.E2 Annual and semi-annual cycle of observed and modelled zonal velocities at 5°N, 23°W 94

5.1 NEUC transport and central position in TRATL01 - multidecadal variability 97
5.2 Linear regression of NEUC transport onto wind stress curl in TRATL01 - mulitdecadal variability 100
5.3 Conceptual model simulations - decadal variability 103
5.4 Conceptual model simulations - multidecadal variability 104
5.5 NEUC transports, AMOC transport and AMV index - multidecadal variability 107

List of Tables

3.1 Ship sections along 23°W from 2002 to 2018. 28
3.2 Observed NEUC intesity, central position and associated oxygen concentrations 37
3.3 Overview over the different simulations performed with the conceptual model (Eq. 3.3). 49

4.1 List of cruises of the meridional ship sections between 21°W and 26°W from 2002 to 2018 80
4.2 Wind stress projections coefficients of shallow water model 92

5.1 Overview over the decadal to multidecadal variability simulations performed with the conceptual model (Eq. 3.3). 101

List of Abbreviations

ADCP	Acoustic Doppler Current Profiler
AMM	Atlantic Meridional mode
AMO	Atlantic Multidecadal Oscilation
AMOC	Atlantic Meridional Overturning Circulation
AMV	Atlantic Multidecadal Variability
ASCAT	Advanced Scatterometer
AZM	Atlantic Zonal Mode
CORE	Coordinated Ocean-Ice Reference Experiments
CMEMS	Copernicus Marine Environment and Monitoring Service
CTD	Conductivity, Temperature, and Depth
DUACS	Developing Use of Altimetry for Climate Studies
ENSO	El Niño - Southern Oscillation
ETNA	Eastern Tropical North Atlantic
EUC	Equatorial Undercurrent
HEOF	Hilbert Empirical Orthogonal Function
IPCC	The Intergovernmental Panel on Climate Change
ITCZ	Inter-Tropical Convergence Zone
JRA-55	Japanese 55-year Reanalysis
JRA55-do	driving ocean–sea-ice models based on JRA-55
MIMOC	Monthly Isopycnal & Mixed-layer Ocean Climatology
MMP	McLane Moored Profiler
NAO	North Atlantic Oscillation
NBC	North Brazil Current

NBUC	North Brazil Undercurrent
NEC	North Equatorial Current
NECC	North Equatorial Countercurrent
NEUC	North Equatorial Undercurrent
nSEC	northern branch of the South Equatorial Current
OGCM	Ocean General Circulation Model
OMZ	Oxygen Minimum Zone
OW	Optimal Width
SSALTO	Segment Sol Multimission Altimetry and Orbitography
SEC	South Equatorial Current
SEUC	South Equatorial Undercurrent
SLA	Sea Level Height Anomaly
SST	Sea Surface Temperature
SSCC	Subsurface Countercurrents
sSEC	southern branch of the South Equatorial Current
STC	Subtropical Cell
TACE	Tropical Atlantic Climate Experiment
TC	Tropical Cell
TIW	Tropical Instability Wave
WES	Wind-Evaporation-SST
XBT	High-Density Expendable Bathythermograph

1 Motivation and Study Aim

The tropical Atlantic current system plays an important role in the northward freshwater and heat transport from the equator towards the subpolar and polar regions (e.g. Hazeleger and Drijfhout, 2006) as well as for the zonal distribution of water mass properties and biogeochemical components like oxygen in the tropical Atlantic (e.g. Duteil et al., 2014; Oschlies et al., 2018). The flow field is characterized by a complex system of zonal currents that can transport oxygen-rich waters from the western boundary towards the Eastern Tropical North Atlantic (ETNA) (Fig. 1.1). The upwelling system in the eastern tropical Atlantic and Pacific are co-located with zones of oxygen-poor water masses at intermediate depth; the so-called Oxygen Minimum Zones (OMZs) result from a combination of high respiration and weak ventilation (Stramma et al., 2008b; Karstensen et al., 2008). During the last few decades, a deoxygenation of the global ocean going along with an expansion of the OMZs is observed (e.g. Stramma et al., 2010; Schmidtko et al., 2017; Oschlies et al., 2018). Within the OMZ, global warming may impact the oxygen concentrations indirectly via changes in the circulation, mixing and oxygen respiration (Oschlies et al., 2018; Brewer and Peltzer, 2017; Brandt et al., 2015; Duteil et al., 2014; Liu and Wang, 2014). However, changes in these mechanisms may be also driven by the natural variability of the climate system. The contribution from these mechanism to changes in the oxygen concentrations have not been quantified yet (Oschlies et al., 2018). This thesis investigates changes in oxygen associated with changes in the circulation and focuses on the ventilation of the ETNA OMZ.

Among the off-equatorial subsurface currents in the tropical Atlantic, the North Equatorial Undercurrent (NEUC) with a core velocity of $0.1\,\mathrm{m\,s^{-1}}$ to $0.3\,\mathrm{m\,s^{-1}}$ is one of the weakest currents but simultaneously it is associated with the highest oxygen concentrations. Consequently, it is thought to act as an important oxygen supply route of the ETNA OMZ (Stramma et al., 2008a; Brandt et al., 2010; Hahn et al., 2017) and changes of the NEUC strength may be attributed to changes of oxygen in the ETNA OMZ. Only a few studies based on model output (Hüttl-Kabus and Böning, 2008) or hydrography data (Goes et al., 2013) investigate the variability of the NEUC, which is still not well understood. In ship sections, the NEUC is likely to be obscured by mesoscale activity

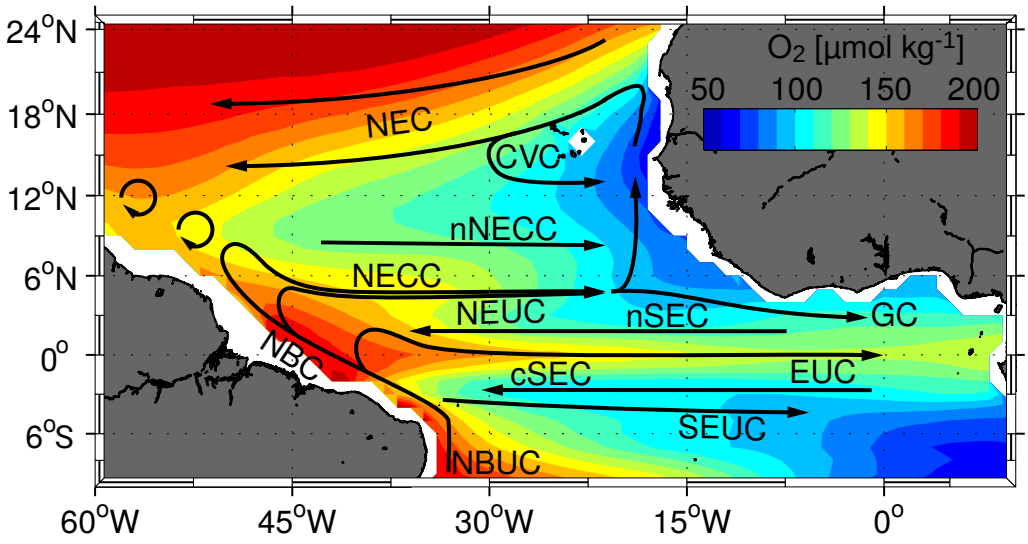

Figure 1.1: Oxygen concentration in μmol kg^{-1} (shaded colors) averaged between 100 m and 200 m depth obtained from MIMOC (Schmidtko et al., 2017). Superimposed are surface and thermocline (about upper 300 m) currents (black solid arrows; adapted from Hahn et al., 2017): the North Equatorial Current (NEC), Cape Verde Current (CVC), North Equatorial Countercurrent (NECC), northern branch of the NECC (nNECC), North Equatorial Undercurrent (NEUC), Guinea Current (GC), northern and central branches of the South Equatorial Current (nSEC, cSEC), Equatorial Undercurrent (EUC), South Equatorial Undercurrent (SEUC), North Brazil Current (NBC) and North Brazil Undercurrent (NBUC). This figure is a subfigure of Fig. 3.1 in (Burmeister et al., 2019)

(Weisberg and Weingartner, 1988) and interannual variability (Hüttl-Kabus and Böning, 2008; Goes et al., 2013) whereas state of the art general circulation models have problems to realistically simulate the equatorial and off-equatorial zonal subsurface currents (Duteil et al., 2014). Furthermore, model studies agree that the NEUC is mainly in geostrophic balance, however, the driving mechanism of the NEUC is under discussion (Marin et al., 2000; Jochum and Malanotte-Rizzoli, 2004; McCreary et al., 2002; Furue et al., 2007, 2009).

In summary, the variability of the NEUC and its impact on oxygen supply of the ETNA OMZ have not been determined yet. Therefore, this thesis aims to investigate the following research questions:

- What are the dominant time scales of NEUC variability?
- What are potential drivers of NEUC variability?
- What is the role of the NEUC variability for changes in the oxygen supply of the ETNA OMZ?

For the analysis, both observational data and the output of a state-of-the-art Ocean General Circulation Model (OGCM) are used. Chapter 2 presents scientific background information about the current system and the intraseasonal to multidecadal variability of the tropical Atlantic as well as the ETNA OMZ. Additionally, potential driving mechanisms and observed current characteristics of the NEUC are described. The NEUC variability and its connection to oxygen in a-state-of-the-art OGCM is investigated in chapter 3. In chapter 4, the NEUC transports are reconstructed based on moored and shipboard velocity observations. Here, the reconstructed transport time series is used to study the NEUC variability and its impact on oxygen based on observations. The studies presented in chapter 3 and 4 mainly focus on intraseasonal to interannual time scales. The decadal to multidecadal variability of the NEUC is investigated in chapter 5. Chapter 6 summarizes the results of this thesis with respect to the above mentioned research question and integrate the result in the current state of knowledge. Finally, new research questions arising from the results of this thesis are discussed.

2 Scientific Background

This chapter provides the scientific background of this thesis. Section 2.1 introduces important oceanographic momentum balances and conservation concepts that are fundamental for this study. The NEUC is part of the wind-driven zonal current system in the tropical Atlantic. Due to its complexity, a comprehensive description of the flow field in the upper tropical Antlantic is given in section 2.2. The tropical Atlantic exhibits variability on intraseasonal to multidecadal time scales that potentially may impact the variability of the NEUC. An overview about the tropical Atlantic variability is given in section 2.3. Section 2.4 provides the current state of research about the OMZs in the global ocean with a special focus on the OMZ in the ETNA. Finally, the current state of research about the NEUC and its potential driving mechanism is presented in section 2.5.

2.1 Important Momentum Balances and Conservation Concepts

In this section some fundamental momentum balances and conservation concepts of the physical oceanography are briefly introduced. The following sections will refer to those balances.

Geostrophic current

Geostrophy is the momentum balance of the pressure gradient and the Coriolis force (e.g. Gill, 1982). The geostrophic balance is given by:

$$\begin{aligned} fu_g &= -\frac{1}{\rho}\frac{\partial p}{\partial y} \\ fv_g &= \frac{1}{\rho}\frac{\partial p}{\partial x} \end{aligned} \tag{2.1}$$

where f is the Coriolis parameter, u_g and v_g are the zonal and meridional component

of geostrophic velocity, respectively, ρ is density and p is pressure. For example, in the Northern Hemisphere, a geostrophic current is flowing eastward parallel to isobars when the pressure is high south and low north of the current.

Ekman Transport

The mean wind-induced flow in the ocean is described by the Ekman volume transport. The Ekman volume transport can be obtained by vertically integrating the Ekman flow given as the momentum balance of the vertical gradient of wind stress and the Coriolis force (Ekman, 1905):

$$fu_E = \frac{\tau_S^y}{\rho_0 H_E} \tag{2.2}$$

$$-fv_E = \frac{\tau_S^x}{\rho_0 H_E}, \tag{2.3}$$

where u_E and v_E are the zonal and meridional components of the Ekman velocity, ρ_0 is reference density, τ_S^y and τ_S^x are the meridional and zonal components of the surface wind stress. The wind stress only acts on the upper 50 m to 100 m of the ocean, the so called Ekman layer H_E. The Ekman volume transport is directed at right angle to the right (left) of the direction of the wind stress in the northern (southern) hemisphere. For example, in the Northern Hemisphere, easterly wind stress results in a northward Ekman transport and westerly wind stress results in a southward Ekman transport. The prevailing wind pattern between 30°S and 30°N consists of north-easterly (south-easterly) trade winds in the northern (southern) hemisphere. Between 30° and 60°S/N westerly winds prevail. In the transition zone between easterlies and westerlies the Ekman volume transport converges, which results in a downward volume tranport called Ekman pumping. In the northern (southern) hemisphere Ekman pumping is associated with a negative (positive) wind stress curl, while Ekman suction (i.e. upwelling) is associated with a positive (negative) wind stress curl.

Sverdrup dynamics

The meridional Sverdrup transport relates the transport in the ocean interior below the Ekman layer to the curl of the wind stress. It can be derived from the momentum balance of the wind stress, the Coriolis force and the pressure gradient (Sverdrup, 1947).

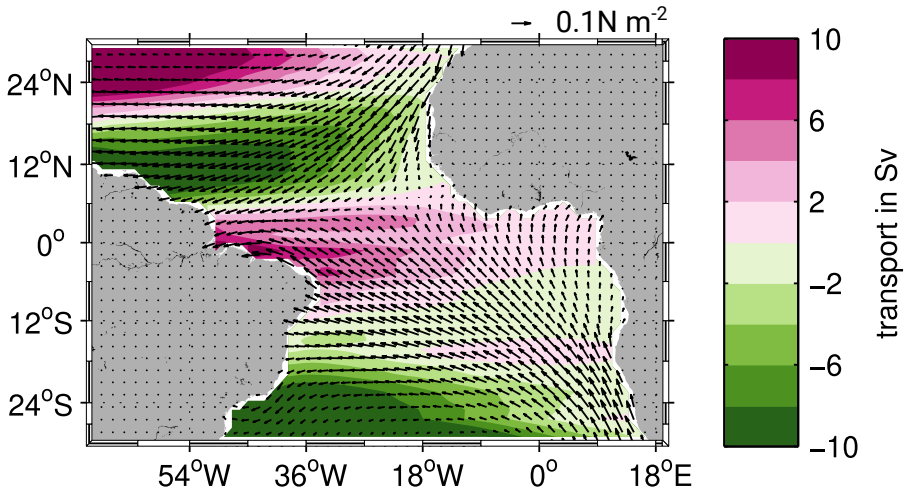

Figure 2.1: Mean ASCAT wind stress (arrows) for the period 2007 to 2018 and the streamfunction of the Sverdrup balance (color shading) estimated from the wind stress curl.

The flat bottom Sverdrup balance is given by:

$$\beta V = \frac{1}{\rho_0}\left[\frac{\partial \tau_S^y}{\partial x} - \frac{\partial \tau_S^x}{\partial y}\right], \tag{2.4}$$

where β is the meridional gradient of the Coriolis parameter and V is the meridional transport. The wind-driven ocean gyres can be explained by Sverdrup dynamics to a large extent. For example, in the Northern Hemisphere a negative wind stress curl (transition from easterlies to westerlies) would lead to a southward Sverdrup transport in the ocean interior below the Ekman layer. The volume transport streamfunction of the circulation is obtained by zonally integrating the meridional Sverdrup transport from the western to the eastern boundary (Fig. 2.1). A negative streamfunction presents an anticlockwise rotation, this means that a zero-contour of the streamfunction with negative values in the south marks maximum westward velocities. Maximum eastward velocities can be found along a zero-contour with negative values north of it. However, the Sverdrup streamlines are not closed at the western boundary. In order to maintain the mass balance, the Sverdrup transport must be balanced by a return flow, which is realized by western boundary currents. Solutions resulting in a closure of the streamlines at the western boundary can be obtained by including horizontal friction in the momentum balance (Stommel, 1948; Munk, 1950).

Potential vorticity conservation

In order to explain the structure of the thermocline, the concept of potential vorticity (Q) is of major importance. The potential vorticity relates the stretching and shrinking of a vortex to the acquisition of cyclonic and anticyclonic vorticity, respectively. For a homogeneous water mass with height h it is given by (Cushman-Roisin and Beckers, 2006):

$$Q = \frac{f + \zeta}{h}, \tag{2.5}$$

where $\zeta = \frac{\partial v}{\partial x} - \frac{\partial u}{\partial y}$ is the vertical component of relative vorticity, that is the vorticity of a fluid due to a rotation of the velocity field. In a large scale ocean where the Coriolis force dominates the flow, the potential vorticity reduces to:

$$Q = \frac{f}{h}, \tag{2.6}$$

The potential vorticity of a water mass is conserved as long as processes which change the water mass characteristics like vertical mixing are absent. In the inviscid case, a flow will follow lines of constant potential vorticity (e.g. Luyten et al., 1983).

2.2 Upper tropical Atlantic circulation

The flow field in the tropical Atlantic is part of the wind-driven equatorial gyre circulation, the shallow subtropical and tropical overturning cells, and the basin-wide Atlantic Meridional Overturning Circulation (AMOC, e.g. Schott et al., 2004). In the upper 300 m, the flow field consists of alternating eastward and westward current branches across the basin and strong western boundary currents with northward flow (black arrows in Fig. 1.1; Schott et al., 2004). The surface currents are the westward flowing North Equatorial Current (NEC) and South Equatorial Current (SEC), the eastward flowing North Equatorial Countercurrent (NECC) as well the northward flowing North Brazil Current (NBC) at the western boundary. In the subsurface, there are the eastward flowing Equatorial Undercurrent (EUC) along the equator, the eastward flowing NEUC and South Equatorial Undercurrent (SEUC) centered at about ±5°N and the northward flowing North Brazil Undercurrent (NBUC) at the western boundary.

To a large extent, the wind-driven equatorial gyre circulation can be explained by Sverdrup dynamics. The trade winds converge in the Inter-Tropical Convergence Zone (ITCZ), which is positioned slightly north of the equator. That means that the south-easterly trade winds cross the equator. Within the ITCZ only weak easterlies

prevail, the so-called Doldrums (Fig. 2.1). This weakening of the north- and south-easterly trade winds is attributed to a positive and negative wind stress curl north and south of the Doldrums, respectively. According to the Sverdrup dynamics this results in a wind-driven equatorial gyre circulation with a clockwise circulation north, and an anticlockwise circulation south of the Doldrums. As a consequence of the Ekman divergence below the Doldrums, an eastward flowing geostrophic current exists, the NECC. In the north and in the south, it is flanked by the westward flowing NEC and SEC, respectively. In the subsurface below the NECC, the eastward flowing NEUC is found.

The shallow Subtropical Cells (STCs) are confined to the upper 500 m and connect the subduction regimes in the subtropics and the upwelling regimes in the tropics (Schott et al., 2004). The complex wind-driven current system of the tropical Atlantic participates in the STCs. The upper limb of the STCs is directed poleward in both hemispheres. It is governed by the wind-induced Ekman transport that results in Ekman divergence between 10°N and 10°S and Ekman convergence poleward of about ±10°N (Schott et al., 2004, Fig. 2.1). Due to the downward Ekman pumping, water can enter the main thermocline below the Ekman layer in the subtropics, which is called subduction. Schott et al. (2004) found weak basin wide subduction poleward of 10°N and 10°S and equatorial and off-equatorial upwelling in the eastern basin. The lower limb of the STC below the Ekman layer is directed equatorward. The subducted water masses in the subtropics are attributed to relative low potential vorticity whereas in the eastern off-equatorial upwelling regions, water masses of the same density are characterized by high potential vorticity (Schott et al., 2004). In order to conserve potential vorticity, the subducted water masses are deflected toward the west (e.g Luyten et al., 1983; Zhang et al., 2003; Schott et al., 2004). However, water masses with the lowest potential vorticity in the tropical Atlantic are found along the equator as the Coriolis force vanishes here. The NEUC and SEUC flow along the boundary between low potential vorticity at the equator and the relative high potential vorticity poleward of the equator (Marin et al., 2000; McCreary et al., 2002).

The tropical overturning cells are part of the STCs and dominate the meridional flow field in the upper 100 m between 5°N and 5°S (e.g. McCreary and Lu, 1994; Schott et al., 2004; Molinari et al., 2003; Perez et al., 2014). They are governed by wind-driven equatorial upwelling, poleward Ekman transport in the upper limb, off-equatorial downwelling at about $\pm 3 - 5°$ latitude and a geostrophic flow directed equatorward in the lower limb.

The Atlantic Meridional Overturning Circulation (AMOC) is part of the global meridional overturning circulation which results from the formation of deep and cold water

masses at high latitude and the upwelling and warming of water masses elsewhere. The AMOC consists of a upper limb flowing towards the north and a lower southward limb. The main part of the upper AMOC limb enters the tropical Atlantic within the westward flowing SEC that bifurcates into the northward flowing NBUC and the southward flowing Brazil Current, before finally crossing the equator within the NBC (e.g. Schott et al., 2004; Hazeleger and Drijfhout, 2006). Here, the zonal currents form an interhemispheric buffer for the AMOC. The EUC, NEUC and NECC feed from the retroflection of the NBC (Bourlès et al., 1999a; Hüttl-Kabus and Böning, 2008; Rosell-Fieschi et al., 2015; Stramma et al., 2005). One third of the AMOC transport recirculates and upwells within the zonal currents and the shallow subtropical cells of the tropical Atlantic, gaining heat and freshwater, before it rejoins the AMOC with modified water mass properties (Hazeleger and Drijfhout, 2006). As a consequence of the northward upper limb of the AMOC, the western boundary pathway of the Southern Hemisphere is strengthened and the western boundary flow of the northern STC is hampered (Fratantoni et al., 2000). Hence, water masses with Southern Hemisphere origin can be found in the tropical North Atlantic.

2.3 Tropical Atlantic variability

The tropical Atlantic variability of Sea Surface Temperatures (SSTs), sea surface winds and ocean-currents can impact each other through different processes on various time scales. The variability of SSTs in the tropical Atlantic is generally thought to be related to rainfall anomalies of the surrounding continents and therefore of great importance for the inhabitants of the coastal regions (Xie and Carton, 2004; Buckley and Marshall, 2015; Lübbecke et al., 2018). In addition, tropical North Atlantic SSTs are crucial for the development of tropical cyclones (Trenberth and Shea, 2006). Hence, the prediction of SSTs variability on various timescales is of major importance to understand and predict rainfall anomalies and the occurrence and development of tropical storms. In this section important features and modes of tropical Atlantic variability on intraseasonal to multidecadal time scales are presented.

Tropical Instability Waves (TIWs) are an important circulation feature in the tropical Atlantic on intraseasonal time scales. They were first detected in satellite observations as westward propagating undulations of sea surface temperature fronts (Legeckis, 1977; Legeckis and Reverdin, 1987). In the Atlantic, TIWs have zonal scales of around 1100 km, and a westward phase speed of around $0.5\,\mathrm{m\,s^{-1}}$. They are generated by barotropic or baroclinic shear instabilities between the nSEC and NECC (Philander,

1978; Athie and Marin, 2008; von Schuckmann et al., 2008) and between the EUC and the nSEC (Weisberg and Weingartner, 1988; Jochum et al., 2004; von Schuckmann et al., 2008). TIWs close to the equator consist of mixed Rossby-gravity (Yanai) waves with periods of 14 to 40 days. Between 2° and 5° latitude, TIWs occur as Rossby waves with periods of 20 to 50 days (e.g. Bunge et al., 2007; Athie and Marin, 2008; von Schuckmann et al., 2008). TIWs, and the vortices that form between the TIW crests, can influence sea surface winds, the circulation as well as the distribution of e.g. temperature, salinity and oxygen from the surface down to the thermocline by transporting heat and momentum (e.g. Philander, 1978; Weisberg and Weingartner, 1988; Jochum and Malanotte-Rizzoli, 2004; Mélice and Arnault, 2017).

The seasonal cycle dominates the variability in the tropical Atlantic and is attributed to the seasonal migration of the ITCZ (Xie and Carton, 2004). The ITCZ coincides with maximum SST in the tropical Atlantic (Okumura and Xie, 2004). In boreal spring it is located close to the equator, where uniform high SSTs exist (e.g. Lübbecke et al., 2018; Xie and Carton, 2004; Schott et al., 2004). With the northward migration of the ITCZ starting in May, the south-easterly trade winds strengthen along the equator. Associated is a seasonal shoaling of the thermocline in the eastern equatorial Atlantic, where a tongue of cold water develops along the equatorial Atlantic persisting until September (e.g. Lübbecke et al., 2018; Xie and Carton, 2004; Okumura and Xie, 2004; Li and Philander, 1997).

The seasonal cycle of the wind forcing also dominates the seasonal variability of the tropical Atlantic circulation (e.g. Brandt and Eden, 2005; Artamonov, 2006). Brandt et al. (2016) studied the linear wave response to the annual wind forcing as driving mechanism of the seasonal cycle of the zonal equatorial flow field. In particular, they focused on the role of resonant equatorial basin modes for the wind-driven variability of the EUC. Resonant equatorial basin modes are low-frequency standing equatorial wave modes consisting of long equatorial Kelvin and Rossby waves (Cane and Moore, 1981). In the equatorial Atlantic, the semi-annual and annual cycle of the zonal flow is attributed to the resonance period of the gravest basin mode for the second and the forth baroclinic mode, respectively (Brandt et al., 2016; Ding et al., 2009; Thierry et al., 2004). Simulations with a shallow water model have suggested that these modes might also impact the zonal velocities within the NEUC region (Brandt et al., 2016; Kopte et al., 2018). On interannual time scales, the zonal equatorial flow is dominated by the equatorial deep jets. Various studies interpreted these jets as equatorial basin modes of higher baroclinic modes (Claus et al., 2016; Greatbatch et al., 2012; D'Orgeville et al., 2007; Ascani et al., 2006). The deep jets have a period of about 4.5 and are suggested

to affect equatorial Atlantic SSTs by the upward propagation of energy (Brandt et al., 2011).

The dominant mode of variability of equatorial SSTs on interannual time scale is the Atlantic Niño, also called the Atlantic Zonal Mode (AZM). It is characterized by an anomalous SSTs in the eastern equatorial Atlantic, peaks in boreal summer and is mainly governed by ocean dynamics. The Atlantic Niño mode is related to interannual rainfall variability over Western Africa and therefore of strong socio-economic impact (Xie and Carton, 2004). Commonly, the warm phases are called Atlantic Niño events, whereas cold phases are referred to as Atlantic Niña events (Lübbecke et al., 2018). Besides the equatorial deep jets—a relative novel driving mechanism of SSTs anomalies in the eastern equatorial Atlantic—several other mechanisms have been discussed to trigger Atlantic Niño and Atlantic Niña events (Lübbecke et al., 2018). The Atlantic Niño was long thought to be governed by ENSO-like dynamics (Zebiak, 1993; Keenlyside and Latif, 2007) where the Bjerknes feedback (i.e. feedbacks between SSTs, zonal winds and thermocline depth, Bjerknes, 1969) plays an important role. However, more recent studies found out that the Atlantic Niño can be also caused by net surface heat flux anomalies (e.g. Bunge and Clarke, 2009; Jansen et al., 2009; Polo et al., 2015; Nnamchi et al., 2016), the reflection of Rossby waves at the western boundary (Burmeister et al., 2016; Lübbecke and McPhaden, 2012; Foltz and McPhaden, 2010b,a) or the advection of off-equatorial subsurface temperature anomalies towards the equator (Richter et al., 2013). The latter two mechanisms describe an interaction between the Atlantic Niño and the Atlantic Meridional mode (AMM) which dominates the tropical Atlantic SSTs variability on interannual to decadal time scales (Nobre and Shukla, 1996).

The characteristic feature of the AMM is a meridional interhemispheric SST gradient centered around 5°N in the tropical Atlantic during boreal spring (Nobre and Shukla, 1996). The wind-induced evaporation and the wind-evaporation-SST feedback are important drivers of the AMM (Carton et al., 1996; Chang et al., 2000). A positive AMM is initiated by high SSTs in the northern tropical Atlantic that lead to a low sea level pressure anomaly. This again causes cross-equatorial sea surface wind anomalies blowing from the Southern toward the Northern Hemisphere. Consequently, the south-east trade winds are strengthened, evaporation is increased, and a negative heat flux anomaly into the ocean in the Southern Hemisphere is caused resulting in a reduction of SST here. In the Northern Hemisphere the trade winds are weakened by the anomalous atmospheric flow, and less evaporation associated with a positive heat flux anomaly into the ocean amplifies the initial warming. The negative AMM is associated with a warming and a cooling in the Southern and Northern Hemisphere, respectively.

The dominant multidecadal variability of Atlantic SSTs is characterized by anomalous SSTs in the entire North Atlantic accompanied by SST anomalies of opposite sign in the South Atlantic (Folland et al., 1986; Schlesinger and Ramankutty, 1994; Kushnir, 1994; Knight et al., 2005). It has been suggested to vary on time scale between 50 and 80 years (Folland et al., 1986; Schlesinger and Ramankutty, 1994; Knight et al., 2005), however the observational record is not long enough to proof the significance of that peak in the frequency spectrum (Buckley and Marshall, 2015). This multidecadal mode of variability is referred to as Atlantic Multidecadal Oscilation (AMO) or Atlantic Multidecadal Variability (AMV) (Kerr, 2000). The AMV affects rainfall over Africa, North America and India, Atlantic Hurricanes as well al the North American and European summer climate (Enfield et al., 2001; Folland et al., 1986; Zhang and Delworth, 2006; Knight et al., 2006; Zhang et al., 2007; Semenov et al., 2010). It can also impact the tropical Atlantic variability on shorter time scales such as the AMM and Atlantic Niño (Martín-Rey et al., 2018). Several model studies suggest a link between the AMV and the AMOC on multidecadal time scales (e.g. Kushnir, 1994; Knight et al., 2005; Latif et al., 2006; Ba et al., 2013; Zhang, 2017; Yan et al., 2019). For example, a multidecadal variability of the AMOC may result in variations of ocean heat transport convergence and hence lead to SST variability (Knight et al., 2005; Latif et al., 2007). In contrast, other studies suggest that the AMV may be triggered by external processes such as changes in the radiative forcing (Foltz and McPhaden, 2008; Booth et al., 2012). When the associated temperature anomalies reach the western boundary, variations of the AMOC are caused due to the thermal wind relation (Danabasoglu, 2008; Buckley et al., 2012). The AMV and the AMOC may also influence each other in a two-way feedback loop (Delworth et al., 1993; Delworth and Greatbatch, 2000; Msadek and Frankignoul, 2009; Buckley and Marshall, 2015). However, observational studies have not yet been able to show any link between changes in SST and AMOC variability (Buckley and Marshall, 2015; Lozier, 2010).

Observational efforts to monitor the AMOC contributed profoundly to the understanding of its variability on intraseasonal to interannual timescales as well as identifying key locations important for its variability (Cunningham et al., 2007; Srokosz and Bryden, 2015; Lozier et al., 2019). Yet, the record of AMOC observations is too short to identify long-term trends or multidecadal variability. Climate studies generally suggest a weakening of the AMOC under global warming (Intergovernmental Panel on Climate Change (IPCC) (2013), 2014) or a decadal to multidecadal variability of the AMOC (e.g. Latif et al., 2006; Biastoch et al., 2008; Rühs et al., 2015). In the tropical Atlantic, decadal AMOC variations can be driven among others by changes in the Agulhas leak-

age (Biastoch et al., 2008) or by wind-driven variability in the tropical-subtropical circulation (Hüttl and Böning, 2006). On multidecadal time scales, AMOC variability is suggested to be governed by changes in the North Atlantic Oscillation (NAO), which describes variations of the sea level pressure differences between the Icelandic Low and the Azores High (e.g. Eden and Willebrand, 2001; Böning et al., 2006; Latif et al., 2006; Robson et al., 2012; Buckley and Marshall, 2015). Separating the effects on the tropical Atlantic current system arising from multidecadal changes of the AMOC or of the wind-driven circulation may be difficult, as both covary on multidecadal time scales (Rühs et al., 2015). However, an instructive example about how AMOC variations on decadal to multidecadal time scales can affect tropical Atlantic variability is given in the model study of Chang et al. (2008). There, a forced abrupt slowdown of the AMOC results in a reversal of the NBC. The interaction between the weakened AMOC and the STCs leads to a substantial warming of SSTs in the eastern equatorial Atlantic. This again results in a weakening of both, the strength and the variability of the West African Monsoon.

2.4 Oxygen minimum zones

Open-ocean OMZs are a common feature of the world oceans (Paulmier and Ruiz-Pino, 2009). They are located at intermediate depth in the upwelling systems of the eastern tropical Atlantic and Pacific Ocean as well as in the northern tropical Indian Ocean (e.g. Brandt et al., 2015). Over the past decades, a net deoxygenation of the global ocean has been observed (e.g. Oschlies et al., 2018; Schmidtko et al., 2017; Brandt et al., 2015) going along with an expansion of the OMZs (Stramma et al., 2008b, 2010). Although the high fishing pressure in the open ocean limits the independent analysis of the effect of expanding OMZs on fisheries, it is likely that the observed oxygen trends accelerates shifts of marine animal distributions and changes in the marine ecosystem structure (Stramma et al., 2010).

The oxygen concentration in the oceans is controlled by the interaction of physical and biogeochemical processes. Oxygen is supplied to the ocean by photosynthesis or air-sea gas exchange and it is transported into the ocean interior by advection and mixing (e.g. Stramma et al., 2008a; Karstensen et al., 2008; Brandt et al., 2015). Oxygen is consumed by respiration, e.g. by remineralization of sinking particles (Matear and Hirst, 2003). The OMZs are a consequence of high respiration and a sluggish ventilation. In the tropical Atlantic and Pacific, the OMZs are located in the eastern boundary upwelling regions which are characterized by high primary productivity. Consequently the demand

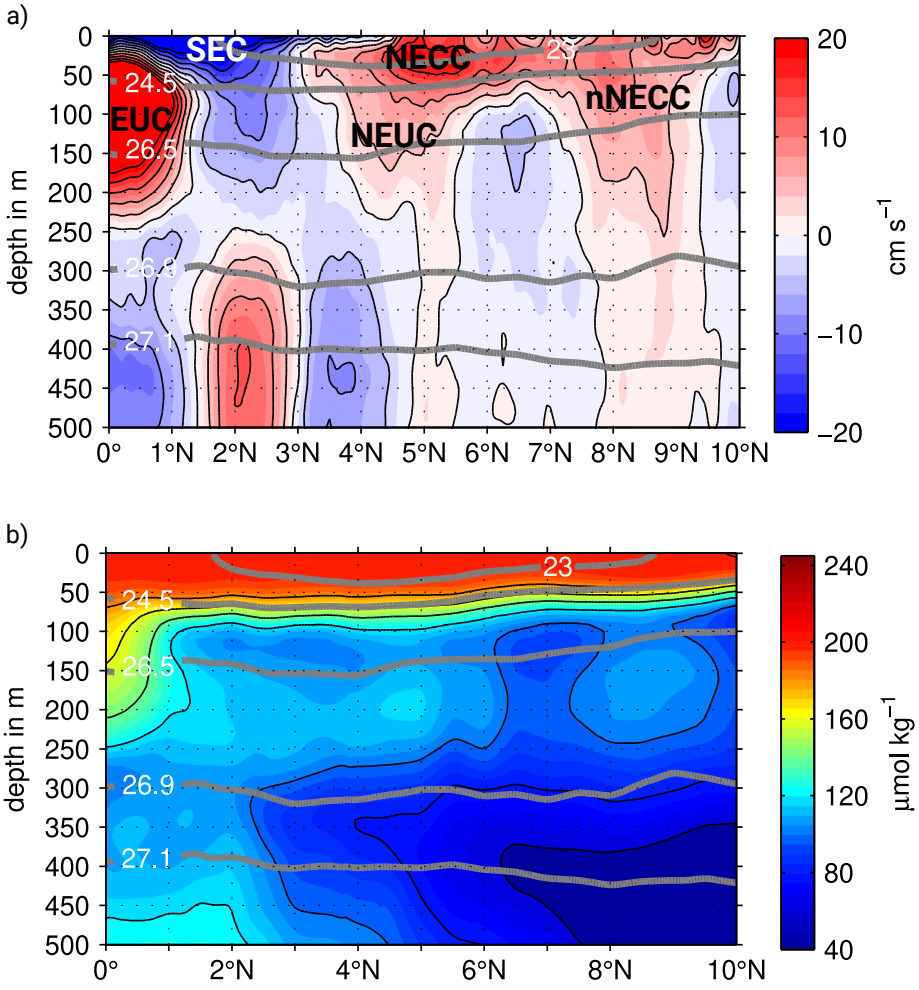

Figure 2.2: (a) Mean zonal velocities and (b) mean oxygen concentrations along 23°W taken during 24 cruises between 22°W and 26°W from 2002 to 2018.

for oxygen is high in the subsurface due to the remineralization of sinking particles (Helly and Levin, 2004). From the physical perspective, the OMZ exists in the shadow zones of the ventilated thermocline (Luyten et al., 1983). As mentioned in section 2.2, ventilated water masses, which are subducted in the subtrocpics, are deflected westwards on their way towards the equator in order to conserve potential vorticity. This leads generally to oxygen-rich water masses in the western basin ventilated by the mean wind-driven circulation while the shadow zones are poorly ventilated by weak alternating zonal currents (e.g. Brandt et al., 2015).

Substantial research about the OMZs is performed within the framework of the collaborative research center 754 'Climate-Biogeochemistry Interactions in the Tropical Ocean'. Observations and models generally agree on a deoxygenation of the global ocean, however large discrepancies exists regarding, among others, the strength of the

deoxygenation, oxygen changes in the thermocline or the temporal variability of oceanic oxygen concentrations (Oschlies et al., 2018, 2017). Near the surface, the deoxygenation is dominated by solubility effects due to global warming (Oschlies et al., 2018; Schmidtko et al., 2017; Helm et al., 2011). Below the surface, for example, within the OMZ, global warming may impact the oxygen concentrations indirectly via changes in the circulation, mixing and oxygen respiration (Oschlies et al., 2018; Brewer and Peltzer, 2017; Brandt et al., 2015; Duteil et al., 2014; Liu and Wang, 2014). However, changes in these mechanisms may be also driven by the natural variability of the climate system. The contribution of these mechanism to changes in the oxygen concentrations have not been quantified yet (Oschlies et al., 2018). This thesis investigates changes in oxygen associated with changes in the circulation and focuses on the ventilation of the ETNA OMZ.

Between 1960 and 2008, the most intense oxygen decline is found in the OMZ of the ETNA compared to the OMZs in the Pacific and Indian Ocean (Stramma et al., 2008b). Minimum oxygen levels in the ETNA OMZ are hypoxic (below $\sim 60\,\mu\mathrm{mol\,kg^{-1}}$), while in the Pacific and Indian Ocean minimum oxygen levels are suboxic (below $\sim$10 $\mu\mathrm{mol\,kg^{-1}}$) or anoxic (no dissolved oxygen). Furthermore, the relative volume of hypoxic water masses in the ETNA OMZ is small (Stramma et al., 2008a). For this reason, the ETNA OMZ has a high potential for further extension of the hypoxic water body. Many macro-organism that are important for both, ecology and economy, are stressed, migrate to more oxygenated waters or die under hypoxic conditions (Gray et al., 2002; Vagner et al., 2008). Additionally, elevated outgasing of potent greenhouse gases, in particular nitrous oxide (N_2O), above OMZs may further drive global warming and hence global oceanic oxygen decrease (Kock et al., 2012; Arévalo-Martínez et al., 2015; Oschlies et al., 2018). It is thus important to understand variability and trends of the ETNA OMZ for better adaptations of ocean and fishery management of the adjacent countries.

Hahn et al. (2014) estimated an oxygen budget for the ETNA OMZ between 6°N and 14°N covering the depth range between 120 m and 570 m. The oxygen budget is given by the oxygen tendency balanced by the oxygen consumption, the diapycnal oxygen supply, the isopycnal meridional eddy supply of oxygen and a residual term. The residual term is interpreted as the zonal advection and zonal eddy supply of oxygen. Between 120 m and 300 m, only the residual term contributes to a positive change in oxygen. Here, the ventilation is dominated by the eastward oxygen advection of the NEUC and the northern branch of the NECC (Hahn et al., 2017; Brandt et al., 2015, 2010; Stramma et al., 2008a). Below the wind-driven ocean circulation, the flow field in

the ETNA OMZ is characterized by eddy-driven, weak latitudinal alternating zonal jets (Maximenko et al., 2005; Ollitrault and Colin de Verdière, 2014; Brandt et al., 2010; Ascani et al., 2010; Qiu et al., 2013) which play a minor role in the mean ventilation of the lower OMZ (Hahn et al., 2014; Brandt et al., 2015). Here, the oxygen budget indicates that the ventilation is dominated by the diapycnal supply and the isopycnal meridional eddy supply. However, the decrease of oxygen concentration in OMZ below 300 m may be linked to a decrease of the mean eastward current strength of the eastward jets (Brandt et al., 2010).

In a more recent study, Hahn et al. (2017) investigated the change of oxygen in the ETNA OMZ from 2006 to 2015. In a depth from 200 m to 400 m they estimated a decrease of oxygen by $-5.9 \pm 3.5\,\mu\mathrm{mol\,kg^{-1}decade^{-1}}$ while oxygen concentrations increased with a rate of $4.0 \pm 1.6\,\mu\mathrm{mol\,kg^{-1}decade^{1}}$ between 400 m and 1000 m. By ruling out other ventilation processes, they suggested the observed change in oxygen is probably due to a decrease (increase) of the zonal advection of oxygen above (below) 400 m. Between 120 m and 300 m, the NEUC has been suggested to be an important oxygen supply route of the ETNA OMZ (Stramma et al., 2008a; Hahn et al., 2014; Brandt et al., 2015). Within the framework of the collaborative research center 754, repeated meridional ship section of velocity, oxygen and hydrography were taking along 23°W. In the mean ship sections, the NEUC is associated with the highest off-equatorial local oxygen maximum centered at about 200 m depth (Fig. 2.2). Hence the question arises, whether changes in the current strength of the NEUC are associated with changes in oxygen supply of the ETNA OMZ. The current state of research about the NEUC, its driving mechanism and its variability is presented in the following section.

2.5 The North Equatorial Undercurrent

This section gives an overview about observational and model studies investigating the NEUC. First, we summarize current research about its mean strength and variability before recent hypotheses on driving mechanisms of the NEUC are presented.

2.5.1 Flow characteristics and variability

The eastward flowing NEUC is located at about 5°N in the tropical North Atlantic (Fig. 1.1 and 2.2). In meridional ship sections along 38°W and 35°W, the NEUC is located between 3°N and 5°N in a depth of 50 m to 400 m (Schott et al., 1995; Bourlès et al., 1999a, 2002; Schott et al., 2003; Urbano et al., 2008). In the eastern basin (26°W-23°W),

the NEUC is positioned more northward (4°N-6°N) in 100 m to 300 m depth (Bourlès et al., 2002; Brandt et al., 2006). The poleward divergence of the NEUC core on its way towards the East was first shown in observations by Bourlès et al. (2002). They linked their findings to the eastward shoaling of the thermocline and the conservation of potential vorticity (Johnson and Moore, 1997).

The NEUC is a weak and highly variable current. Its observed core velocity varies from below $0.1\,\mathrm{m\,s^{-1}}$ (Brandt et al., 2006) to over $0.3\,\mathrm{m\,s^{-1}}$ (Urbano et al., 2008). Observational estimates of NEUC transport range from 2.7 Sv to 6.9 Sv in meridional ship sections taken between 38°W and 35°W (Schott et al., 1995; Bourlès et al., 1999a, 2002; Schott et al., 2003; Urbano et al., 2008). However, its mean strength remains uncertain as in ship sections the NEUC is likely to be obscured by mesoscale activity (Weisberg and Weingartner, 1988) or interannual variability (Hüttl-Kabus and Böning, 2008; Goes et al., 2013). Furthermore, the upper part of the NEUC and the lower part of the NECC are difficult to seperate during most of the year, especially during boreal summer and fall (Bourlès et al., 1999a, 2002; Schott et al., 2003; Brandt et al., 2006; Urbano et al., 2008; Hüttl-Kabus and Böning, 2008; Jochum and Malanotte-Rizzoli, 2004). In the following, transport estimate will be discussed which are commonly integrated between the $24.5\,\mathrm{kg\,m^{-3}}$ and $26.8\,\mathrm{kg\,m^{-3}}$ potential density layer.

Shipboard observations are still too sparse to detect a seasonal cycle of the NEUC. For boreal spring, four transport estimates, varying from 1.6 Sv to 3.6 Sv, exist between 35°W and 38°W from 1993 to 1996 (Schott et al., 1995; Bourlès et al., 1999a). Here, the NEUC position varies between 3.5° N to 5.5° N. In boreal fall, one NEUC transport estimate of 2.5 Sv between 4°N and 6°N is found (Bourlès et al., 1999a). Another method to investigate the seasonal cycle of the NEUC based on observations is used by Goes et al. (2013). They combined expendable bathythermograph (XBT) temperature with altimetric sea level anomalies to derive NEUC location, velocity and transport between 30°W and 23°W. In the potential density layers of 24.5-26.8 $\mathrm{kg\,m^{-3}}$ they found a NEUC transport varying from 2.3 Sv during August to October up to 5.5 Sv during May and June. The core position of the NEUC in the synthesis product vary between 4.5°N and 5.5°N and exhibits a semi-annual cycle with minima in April an September and maxima in August and December. Their estimated NEUC core velocities were highest in June (above $0.3\,\mathrm{m\,s^{-1}}$) and lowest during boreal fall (below $0.2\,\mathrm{m\,s^{-1}}$). In line with the findings by Goes et al. (2013), Hüttl-Kabus and Böning (2008) found a clear seasonal cycle of the NEUC in a eddy-permitting OGCM. Here, the NEUC reaches maximum transports (4.5-7 Sv) at 23°W and 35°W between May and June, and mimimum transports (1.2-4.2 Sv) between September to October. The authors

found a westward propagation of the seasonal cycle consistent with the annual Rossby wave patterns (Thierry et al., 2004; Böning and Kröger, 2005; Brandt and Eden, 2005).

Until now, less is known about the interannual to multidecadal variability of the NEUC. In the model study of Hüttl-Kabus and Böning (2008) the interannual variability of the seasonal cycle of the NEUC is up to 2 Sv, which is nearly as strong as the amplitude of the seasonal cycle (3 Sv) and may obscure the mean strength of the NEUC derived from observations. The results of Goes et al. (2013) indicate an anticorrelation between NEUC transport variability and the AMM. Goes et al. (2013) highlight the inverse SST anomalies in the Guinea Dome region and the equatorial Atlantic associated with the AMM. This can alter the north-south density gradient in the NEUC region and strengthen (negative AMM, increased density gradient) or weaken (pos AMM, decreased density gradient) the NEUC core (McCreary et al., 2002; Furue et al., 2007).

2.5.2 Potential driving mechanisms

Until now, the underlying dynamics of the NEUC have not been studied in particular. Potential driving mechanisms for the NEUC are based on numerical and theoretical studies investigating its southern counterpart in the Atlantic, the SEUC (Jochum and Malanotte-Rizzoli, 2004), or its Pacific counterparts, the so-called Tsuchiya jets or Subsurface Countercurrents (SSCC) (Marin et al., 2000; McCreary et al., 2002; Furue et al., 2007, 2009). Common features of currents like the NEUC consist in their geostrophic balance and their co-location with meridional potential vorticity gradients. However, the numerical studies do not agree on the driving mechanism of these currents which may be forced by local (Marin et al., 2000; Jochum and Malanotte-Rizzoli, 2004) or large-scale processes (McCreary et al., 2002; Furue et al., 2007, 2009).

Marin et al. (2000) studied the SSCCs in the Pacific. They suggest that the meridionally shoaling of the thermocline at the equator drives ageostrophic meridional overturning cells to advect angular momentum poleward generating eastward currents, the SSCCs, at the poleward edges of these cells. For their analysis, they developed a simple 2-D model to simulate the SSCCs. In their model they added a local diapycnal forcing driving the ageostrophic cells. Follow-up studies (Hua et al., 2003; Marin et al., 2003) show that similar ageostrophic meridional overturning cells develop in an eddy-permitting OGCM, however the diapycnal transfer process driving the ageostrophic cells remains unclear.

Jochum and Malanotte-Rizzoli (2004) investigated the dynamics of the SEUC in the Atlantic using an eddy-permitting OGCM. To explore the momentum balance of the SEUC, they reformulated the transformed Eulerian mean equations (Eliassen and Palm, 1960). Based on this framework, they found that in their model the convergence of the Eliassen-Palm flux of TIWs maintained the SEUC against dissipation. They propose, that the meridional heat flux of the TIWs steepens the meridional slope of isopycnals causing a geostrophic flow, the SEUC.

Another driving mechanism for the the SSCCs in the Pacific acting on a larger-scale was introduced by McCreary et al. (2002). They used a hierarchy of idealized numerical simulations based on $2\frac{1}{2}$- to $4\frac{1}{2}$-layer models. They suggest that the SSCCs are forced by the Indonesian throughflow and the upwelling of the doming regions in the eastern basin. In their simulations, the SSCCs are geostrophic currents along arrested fronts. Such fronts are generated by the convergence or intersection of Rossby wave characteristics in the ocean interior, carrying information about the density structure away from the eastern boundary. Furue et al. (2007) and Furue et al. (2009) investigated the SSCCs in a non-eddy-permitting OGCM, supporting the theory of McCreary et al. (2002) that the SSCCs are geostrophic currents along arrested fronts drawn by the upwelling of the domes in the eastern basin.

In summary, the driving mechanism of the NEUC are still under discussion (Marin et al., 2000; McCreary et al., 2002; Jochum and Malanotte-Rizzoli, 2004; Furue et al., 2007, 2009). Mean NEUC transport estimates derived from shipboard observations are uncertain as they are obscured by mesoscale (Weisberg and Weingartner, 1988) and interannual variability (Hüttl-Kabus and Böning, 2008; Goes et al., 2013). A seasonal cycle of the NEUC has been found in the model study by Hüttl-Kabus and Böning (2008) and in the study by Goes et al. (2013) based on hydrographic data. Goes et al. (2013) observed also a link between the interannual variability of the NEUC and the AMM. However, the variability of the NEUC has not yet been studied by direct velocity observations. Hence, this study aims to investigate the dominant time scales of NEUC variability and its potential driving mechanisms.

3 Interannual variability of the Atlantic North Equatorial Undercurrent and its impact on oxygen

This chapter focuses on the interannual variability of the NEUC and its impact on oxygen in a state of the art OGCM. Due to discrepancies between the OGCM and observations, important conclusions about the impact of the NEUC variability on the oxygen distribution could be drawn. The results of this study suggest that only an elevated NEUC supply from the western boundary acts to increase oxygen levels within the NEUC. However, the NEUC can also be strengthened by recirculations with the northern branch of the westward flowing South Equatorial Undercurrent which is associated with a reduction of oxygen levels within the NEUC.

The manuscript was published in *Journal of Geophysical Research: Oceans* in March 2019.

Citation: **Burmeister K.**, Lübbecke, J. F., Brandt, P., & Duteil, O. (2019). Interannual variability of the Atlantic North Equatorial Undercurrent and its impact on oxygen. Journal of Geophysical Research: Oceans, 124.
https://doi.org/10.1029/2018JC014760

The candidate carried out the analysis of observational data sets and model output. She performed all simulations with the conceptual model based on the model developed by Brandt et al. (2010). The candidate produced all figures and authored the manuscript from the first draft to the final version.

Abstract

The North Equatorial Undercurrent (NEUC) has been suggested to act as an important oxygen supply route towards the oxygen minimum zone in the Eastern Tropical North Atlantic. Observational estimates of the mean NEUC strength are uncertain due to the presence of elevated mesoscale activities, and models have difficulties in simulating a realistic NEUC. Here we investigate the interannual variability of the NEUC and its impact onto oxygen based on the output of a high-resolution ocean general circulation model (OGCM) and contrast the results with an unique data set of 21 ship sections along 23°W and a conceptual model. We find that the interannual variability of the NEUC in the OGCM is related to the Atlantic Meridional Mode (AMM) with a stronger and more northward NEUC during negative AMM phases. Discrepancies between OGCM and observations suggest a different role of the NEUC in setting the regional oxygen distribution. In the model a stronger NEUC is associated with a weaker oxygen supply towards the east. We attribute this to a too strong recirculation between the NEUC and the northern branch of the South Equatorial Current (nSEC) in the OGCM. Idealized experiments with the conceptual model support the idea that the impact of NEUC variability on oxygen depends on the source water pathway. A strengthening of the NEUC supplied out of the western boundary acts to increase oxygen levels within the NEUC. A strengthening of the recirculations between NEUC and the nSEC results in a reduction of oxygen levels within the NEUC.

Plain Language Summary

In the eastern tropical North Atlantic a zone of low-oxygen waters exists between 100 m and 700 m due to high oxygen consumption in that region and a weak exchange of water masses with the surroundings. Long-term oxygen changes in this zone have been reported with potential impacts on, e.g., biogeochemical cycles and ecosystems including fish populations. The water masses in that region are exchanged among others via weak eastward and westward currents. Based on the mean background oxygen distribution the mean eastward flowing North Equatorial Undercurrent (NEUC) transports oxygen-rich waters from the western basin into the eastern low-oxygen zone suggesting that a stronger NEUC supplies more oxygen-rich water from the western towards the eastern basin.

In this study we investigate the year-to-year variability of the NEUC and its impact on oxygen. For our analysis, we are using ship observations and model simulations. We find some discrepancies between them that we attribute to a too strong recirculation

between the NEUC and the westward flowing current just south of it in the model. This recirculation also impacts the variability in eastward oxygen supply as the westward current is transporting low-oxygen waters. In the model, a higher recirculation between the currents results in a stronger NEUC transporting lower-oxygen waters, a mechanism for oxygen variability that could not be conjectured from observations so far.

3.1 Introduction

The oxygen concentration in the oceans is controlled by the interaction of physical and biogeochemical processes. Oxygen is supplied to the ocean by photosynthesis or air-sea gas exchange and it is transported into the ocean interior by advection and mixing (e.g. Stramma et al., 2008a; Karstensen et al., 2008; Brandt et al., 2015). Oxygen is consumed by respiration, e.g. by remineralization of sinking particles (Matear and Hirst, 2003). Locally advection and mixing can also act to decrease oxygen levels, depending on the background oxygen field (Brandt et al., 2010; Hahn et al., 2014).

The tropical Atlantic is characterized by a complex system of zonal currents that can transport oxygen-rich waters from the western boundary eastwards towards the Eastern Tropical North Atlantic (ETNA) Oxygen Minimum Zone (OMZ) or oxygen-poor waters westward (Fig. 3.1). Consequently, the zonal advection of oxygen-rich water masses from the western boundary by eastward flowing ocean currents has been identified as an important ventilation process for the ETNA OMZ, especially in the upper 130 to 300 m (Hahn et al., 2014, 2017; Brandt et al., 2015). The most important currents are the main wind-driven ones such as the Equatorial Undercurrent (EUC), the North Equatorial Undercurrent (NEUC) and the northern branch of the North Equatorial Countercurrent (nNECC) (e.g. Bourlès et al., 2002; Schott et al., 2004; Peña-Izquierdo et al., 2015). Below the wind-driven ocean circulation, the flow field in the ETNA OMZ is characterized by eddy-driven, weak latitudinal alternating zonal jets (Maximenko et al., 2005; Ollitrault and Colin de Verdière, 2014; Brandt et al., 2010; Ascani et al., 2010; Qiu et al., 2013).

Oxygen levels in the ETNA OMZ are declining in accordance with global deoxygenation (Stramma et al., 2008b; Schmidtko et al., 2017). Superimposed on this multidecadal trend are interannual to decadal variations. The identification of the mechanisms of long-term oxygen changes is challenging because of large uncertainties in the observed oxygen budget terms (Hahn et al., 2017; Oschlies et al., 2018). Furthermore, large biases in the oxygen distribution in ocean models hamper the analysis of OMZ variability (e.g. Oschlies et al., 2018, 2017; Cabré et al., 2015; Duteil et al., 2014; Stramma et al., 2012;

Dietze and Loeptien, 2013). One reason for an insufficient representation of eastern tropical OMZs in models is that state of the art general circulation models have problems to realistically simulate the equatorial and off-equatorial zonal subsurface currents (Duteil et al., 2014).

Among the off-equatorial eastward subsurface current bands, the NEUC is associated with the highest oxygen levels in the eastern Tropical Atlantic basin (Fig. 3.1). The NEUC is centered at 5°N (Fig. 3.1a,b) and is located at depth where zonal advection plays an important role in ventilating the ETNA OMZ (Hahn et al., 2014). The western boundary regime is ventilated by oxygen-rich water masses supplied by the North Brazil Current (NBC). The EUC, NEUC and nNECC feed from the retroflection of the NBC (Bourlès et al., 1999b; Stramma et al., 2005; Hüttl-Kabus and Böning, 2008; Rosell-Fieschi et al., 2015). The NEUC thus can supply oxygen-rich water masses from the western boundary towards the ETNA OMZ (Stramma et al., 2008a; Brandt et al., 2010). Although its mean velocity is comparable to that of the nNECC, its associated oxygen maxima along 23°W has been observed to be several μmol kg^{-1} higher (Fig.3.1b,c).

The underlying dynamics of the NEUC are still not fully understood. Several model studies show that the NEUC is mainly in geostrophic balance but they do not agree on its driving mechanism. Marin et al. (2000) studied the Pacific counterparts of the NEUC, the so called Tsuchiya jets or Subsurface Countercurrents and compared their dynamics with the atmospheric zonal jets of the Hadley Cell at around 30°N. They suggest that the tropical cells are the oceanic dynamical equivalent to the Hadley Cells, where the conservation of angular momentum plays a key role in explaining the zonal jets. Jochum and Malanotte-Rizzoli (2004) investigated the dynamics of the SEUC, the southern counterpart of the NEUC in the Atlantic. Their model results show that the Eliassen-Palm flux associated with the propagation of Tropical Instability Waves (TIWs) can be one possible driver of such zonal currents. Other model studies in the Pacific suggest that the oceanic jets are pulled by the upwelling within domes in the eastern basin or by the eastern boundary upwelling (McCreary et al., 2002; Furue et al., 2007, 2009).

The NEUC is a weak and highly variable current. Its observed core velocity varies from below 0.1 m s^{-1} (Brandt et al., 2006) to over 0.3 m s^{-1} (Urbano et al., 2008). In ship sections the NEUC is likely to be biased by the high mesoscale activity present in the tropical Atlantic (e.g. Weisberg and Weingartner, 1988; Goes et al., 2013). Furthermore, estimates of NEUC transport are difficult because a clear separation of the current cores of the NEUC and North Equatorial Countercurrent (NECC) above is not possible (Fig. 3.2a). Observational estimates range from 2.7 Sv to 6.9 Sv in meridional ship sections

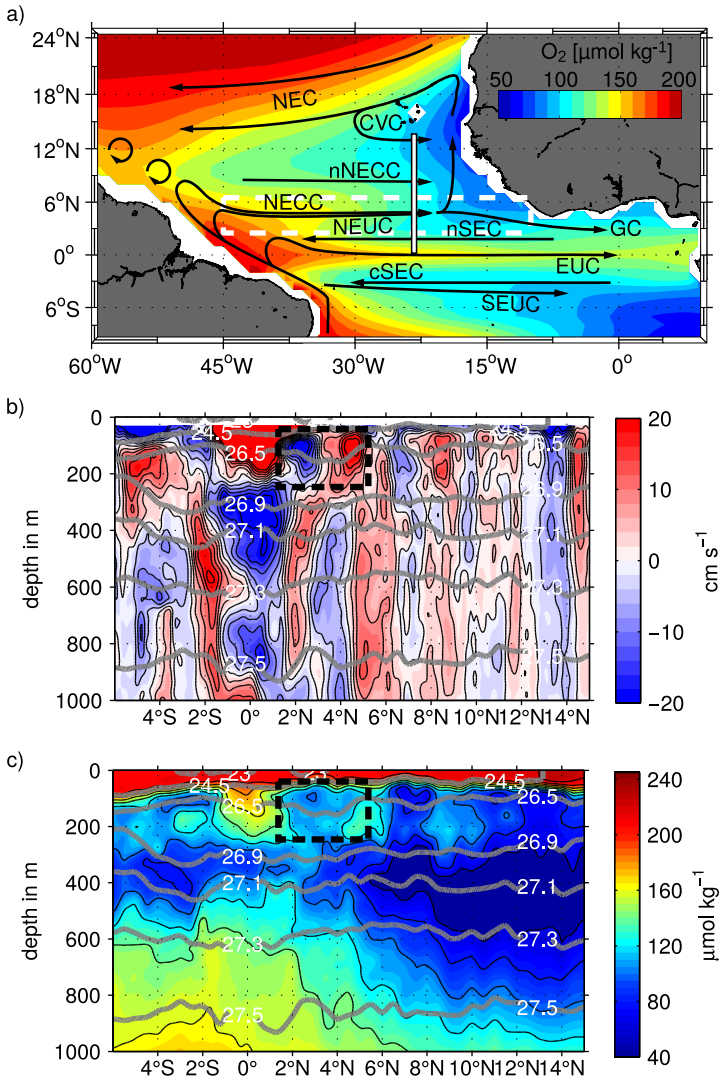

Figure 3.1: (a) Oxygen concentration in μmol kg^{-1} (shaded colors) in the tropical Atlantic averaged between 100m and 200m depth (depth range of NEUC core) obtained from MIMOC (Schmidtko et al., 2017). Superimposed are surface and thermocline (about upper 300 m) currents (black solid arrows; adapted from Hahn et al. (2017)): the North Equatorial Current (NEC), Cape Verde Current (CVC), Mauritania Current/poleward undercurrent (MC/PUC), Guinea Dome (GD), North Equatorial Countercurrent (NECC), northern branch of the NECC (nNECC), North Equatorial Undercurrent (NEUC), northern and central branches of the South Equatorial Current (nSEC, cSEC), Equatorial Undercurrent (EUC), South Equatorial Undercurrent (SEUC) and North Brazil Current (NBC). The white bar denotes the 23°W section between 0° and 14°N. The white dashed rectangle marks the model domain of the conceptual model.
(b) Zonal velocity and (c) oxygen observations along 23°W obtained during Meteor cruise M145 from February to March 2018. The black dashed rectangles marks the region of a potential recirculation between the nSEC and NEUC.

taken between 38°W and 35°W (Schott et al., 1995; Bourlès et al., 1999a, 2002; Schott et al., 2003; Urbano et al., 2008). Another problem is that some transport estimates from observations only cover part of the NEUC, as for example Brandt et al. (2006) calculated zonal current transports from a mean ship section along 26°W. They found a transport of only 0.8 Sv for the eastward flow in the region of the NEUC along 26°W, but only covered the flow south of 5°N.

Goes et al. (2013) used a synthetic method to estimate the NEUC transport between 30°W and 23°W. They combined expendable bathythermograph (XBT) temperature with altimetric sea level anomalies to derive NEUC location, velocity and transport. In the potential density layers of 24.5-26.8 $\mathrm{kg\,m^{-3}}$ they found a NEUC transport varying from 2.3 Sv during August to October to up to 5.5 Sv during May and June. The core position of the NEUC in the synthesis product varies between 4.5°N and 5.5°N and exhibits a semiannual cycle with minima in April and September and maxima in August and December. Their estimated NEUC core velocities were highest in June (above 0.3 $\mathrm{m\ s^{-1}}$) and lowest during boreal fall (below 0.2 $\mathrm{m\ s^{-1}}$). In a model study, Hüttl-Kabus and Böning (2008) found a clear seasonal cycle of the NEUC at 35°W and 23°W with maximum NEUC transports (4.5-7.0 Sv) between May and June, and minimum transports (1.2-4.2 Sv) between September to October. They found a westward propagation of the seasonal cycle consistent with annual Rossby wave patterns (Thierry et al., 2004; Böning and Kröger, 2005; Brandt and Eden, 2005).

In ship sections the NEUC shows no clear seasonal cycle. Four transport estimates exist between 35°W and 38°W during boreal spring from 1993 to 1996 (Schott et al., 1995; Bourlès et al., 1999a). In the same depth range as in Goes et al. (2013) and Hüttl-Kabus and Böning (2008) they vary from 1.6 Sv to 3.6 Sv and the NEUC position varies between 3.5°N to 5.5°N. For boreal fall there is one NEUC transport estimate of 2.5 Sv between 4°N and 6°N (Bourlès et al., 1999a). Note that especially during boreal summer and fall as well as in the mean ship sections the NEUC and the NECC are difficult to distinguish (Bourlès et al., 1999a, 2002; Schott et al., 2003; Brandt et al., 2006; Urbano et al., 2008). As the NEUC is likely to be obscured by the high mesoscale activity (Weisberg and Weingartner, 1988; Goes et al., 2013) the mean is uncertain and the seasonal cycle cannot be estimated reliably from ship sections.

Only few studies have investigated the interannual variability of the NEUC. In a model study Hüttl-Kabus and Böning (2008) estimated an interannual variability of the seasonal cycle of 2 Sv, which is almost as strong as the amplitude of the seasonal cycle (3 Sv). The results of Goes et al. (2013) indicate an anticorrelation between NEUC transport variability and the Atlantic Meridional Mode (AMM). The AMM is

characterized by a meridional inter-hemispheric gradient of sea surface temperature (SST) in the tropical Atlantic centered around 5°N (Nobre and Shukla, 1996). Important drivers of the AMM are wind-induced evaporation and the wind-evaporation-SST (WES) feedback (Carton et al., 1996; Chang et al., 2000). Initially high SSTs in the northern tropical Atlantic lead to a low sea level pressure anomaly which causes cross equatorial sea surface wind anomalies blowing from the southern towards the northern hemisphere. This strengthens the southeast trade winds, increases evaporation and leads to a negative heat flux anomaly into the ocean in the southern hemisphere, i.e. a reduction of SST here. In the northern hemisphere the trade winds are weakened by the anomalous atmosphere flow, and less evaporation associated with a positive heat flux anomaly into the ocean amplifies the initial warming here. This is referred to a positive AMM. The negative AMM is associated with a warming and a cooling in the southern and northern hemisphere, respectively.

Goes et al. (2013) hypothesized that changes in the meridional density gradient driven by the AMM is a possible mechanism that can drive NEUC variability. They highlight the inverse SST anomalies in the Guinea Dome region and in the equatorial Atlantic associated with the AMM. This can alter the north-south density gradient in the NEUC region and strengthen (negative AMM, increased density gradient) or weaken (positive AMM, decreased density gradient) the NEUC core (McCreary et al., 2002; Furue et al., 2007; Goes et al., 2013).

In summary, the interannual variability of the NEUC and its potential drivers are still not fully understood. As the NEUC is suggested to act as an important oxygen supply route towards the ETNA OMZ, it is crucial to understand possible mechanisms by which the NEUC variability impacts the oceanic oxygen distribution. As observations are still too sparse, we will use a state of the art ocean general circulation model (OGCM) in combination with a conceptual model to study these mechanisms.

In this study we investigate the interannual variability of the NEUC and the associated oxygen response in a state of the art OGCM and a conceptual model. The study aims to improve (1) the understanding of oceanic processes that impact the mean distribution and interannual variability of dissolved oxygen in the NEUC region and (2) the understanding of discrepancies between simulated and observed NEUC variability and associated oxygen changes. For our analysis we are using the output of the high-resolution OGCM TRATL01 (Duteil et al., 2014) in combination with an unique data set of 21 ship section along 23°W from 2002 to 2018. We utilize an algorithm developed by Hsin and Qiu (2012) to estimate the NEUC position and intensity in both the observational data and the output of TRATL01. To better understand the contradicting

results between the observations and the TRATL01 output we extend our analysis with a conceptual model simulating an eastward current and its westward return flow with an oxygen source at the western boundary following Brandt et al. (2010).

3.2 Data and Methods

3.2.1 Observations

Velocity data of 21 ship sections along 23°W obtained from 2002 to 2018 are used. For 13 and 11 of this sections also hydrographic and oxygen data are available, respectively. A detailed overview of the cruises is shown in Table 3.1. All ship sections cover at least the upper 400 m between 0° and 8°N.

Velocity data are acquired by vessel-mounted and lowered Acoustic Doppler Current Profilers (ADCPs). Vessel-mounted ADCPs (vm-ADCPs) are continuously recording velocities throughout the section. The accuracy of 1 h averaged vm-ADCP data is better than 2-4 $\mathrm{cm\,s^{-1}}$ (Fischer et al., 2003). Lowered ADCPs (l-ADCPs) are attached in pairs of upward and downward looking instruments to a CTD (Conductivity-Temperature-Depth) rosette and record velocities during CTD casts typically performed on a uniform latitude grid with half-degree resolution. This enables velocity measurements throughout the whole water column. The accuracy of full-depth l-ADCP velocity profiles is better than 5 $\mathrm{cm\,s^{-1}}$ (Visbeck, 2002). Hydrographic and oxygen data are obtained during CTD casts. The data accuracy for a single research cruise is generally assumed to be better than 0.002°C, 0.002 and 2 $\mu\mathrm{mol\,kg^{-1}}$ for temperature, salinity, and dissolved oxygen, respectively (Hahn et al., 2017). The final ship sections and mean sections along 23°W are obtained from the observational data as described in Brandt et al. (2010). First all velocity data are merged accounting for their different accuracy and resolution. Then the velocity, hydrographic and oxygen data are mapped on a regular grid (0.05° latitude × 10 m) using a Gaussian interpolation scheme. All data are averaged at each grid point to derive the mean sections which are smoothed by a Gaussian filter (horizontal and vertical influence (cutoff) radii: 0.05° (0.1°) latitude and 10 m (20 m), respectively). For the mean velocity, temperature, salinity and oxygen section the standard error in the NEUC region ($100 - 300$ m depth, $3° - 6.5°$N) are 1.4 $\mathrm{cm\,s^{-1}}$, 0.12°C, 0.01 and 3.4 $\mu\mathrm{mol\,kg^{-1}}$, respectively.

Table 3.1: Ship sections along 23°W from 2002 to 2018. All sections cover at least the upper 400 m from 0°N to 8°N. For all sections ADCP data is available. Sections including oxygen (O_2) or hydrography (CTD) measurements are marked accordingly.

cruise	Expocode	date	lon	lat	O_2	CTD
Meteor 55	06MT20021013	2002 Oct	24°W	0–10°N	no	no
Ronald H. Brown	33RO20030619	2003 Aug	27°W	-6-10°N	no	no
Ronald H. Brown	33RO20060527	2006 Jun	23°W	-5-13.5°N	yes	yes
Meteor 68/2	06M320060606	2006 Jun	23°W	-4-14°N	yes	yes
Ronald H. Brown	33RO20060622	2006 Jun	23°W	-5-14°N	yes	yes
L'Atalante	35A320080223	2008 Mar	23°W	-2-14°N	yes	yes
L'Atalante	35A320080223	2008 Mar	23°W	-2-14°N	no	no
Ronald H. Brown PNE09	33RO20090711	2009 Jul	23°W	0-14°N	no	no
Meteor 80/1	06M320091026	2009 Nov	23°W	-6-14°N	yes	yes
		2009 Nov	23°W	-6-14°N	no	no
Meteor 81/1	06M320100204	2010 Feb	22°W	-6-13°N	no	no
Ronald H. Brown PNE10	33RO20100426	2010 May	23°W	0-14°N	no	yes
Maria S. Merian 18/2	06MM20110511	2011 May	23°W	0-14°N	no	no
Ronald H. Brown PNE11	33RO20110721	2011 Aug	23°W	0-14°N	no	no
Maria S. Merian 22	06MM20121024	2012 Nov	23°W	-6-8°N	yes	yes
		2012 Nov	23°W	0-14°N	no	no
Meteor 106	06M320140419	2014 May	23°W	-6-14°N	yes	yes
Polarstern PS88.2	06AQ20141102	2014 Nov	23°W	-2-14°N	yes	yes
Meteor 119	06M320150908	2015 Sep	23°W	-5.5-14°N	yes	yes
Meteor 130	06M320160828	2016 Aug	23°W	-6-14°N	yes	yes
Meteor 145	06M320180213	2018 Feb	23°W	-6-14°N	yes	yes

3.2.2 High-resolution global ocean circulation model TRATL01

We are using the output of the global ocean circulation model TRATL01, in which a 1/10° nest covering the tropical Atlantic from 30°S to 30°N is embedded into a global 1/2° model (Duteil et al., 2014). TRATL01 reproduces the tropical zonal jets more realistically compared to a coarser resolution model, resulting in an improved representation of the low oxygenated regions in the ETNA (Duteil et al., 2014). The model is based on the Nucleus for European Modeling of the Ocean (NEMO) v3.1 code (Madec, 2008). The thickness of its 46 vertical levels increases from 6 m at the surface to 250 m at depth. The model is forced with momentum, heat and freshwater fluxes from the Coordinated Ocean-Ice Reference Experiments (CORE) v2 data set

for the time period from 1948 to 2007 (Griffies et al., 2009). A simple biogeochemical model is coupled with the global ocean circulation model. The biogeochemical model contains 6 compartments (dissolved oxygen, phosphate, phytoplankton, zooplankton, particulate and dissolved organic matter). The parameter set (e.g. phytoplankton growth rate, mortality, grazing) has been optimized to realistically reproduce the oxygen and phosphate distribution in a global model (Kriest et al., 2010).

We are analyzing the monthly mean model output from 1958-2007. In TRATL01, oxygen concentrations in the NEUC region ($100-300\,\mathrm{m}$ depth, $3°-6.5°\mathrm{N}$, $45°-15°\mathrm{W}$) are drifting on average by $-0.5\,\mu\mathrm{mol\,kg^{-1}\,yr^{-1}}$ from 1958-2007; reaching an equilibrium state would take several hundred years. The spurious drift is very strong in the first 30 years (144 % of the averaged drift). Therefore, the analysis of the oxygen variability is restricted to the period 1990-2007 where the drift is only 11 % of the averaged drift. For the mean velocity, temperature, salinity and oxygen section along 23°W from 1990 to 2007 in TRATL01 the standard errors in the NEUC region ($100-300\,\mathrm{m}$ depth, $3°-6.5°\mathrm{N}$) are $1.02\,\mathrm{cm\,s^{-1}}$, 0.09°C, 0.01 and $0.81\,\mu\mathrm{mol\,kg^{-1}}$, respectively.

3.2.3 NEUC characterization

For both, TRATL01 and the observational data we calculate the central position Y_{CM} and along-pathway intensity INT of the NEUC using the algorithm of Hsin and Qiu (2012).

$$Y_{CM}(x,t) = \frac{\int_{Z_l}^{Z_u}\int_{Y_S}^{Y_N} y\ u(x,y,z,t)\ dy\ dz}{\int_{Z_l}^{Z_u}\int_{Y_S}^{Y_N} u(x,y,z,t)\ dy\ dz} \tag{3.1}$$

$$INT(x,t) = \int_{Z_l}^{Z_u}\int_{Y_{CM}-W}^{Y_{CM}+W} u(x,y,z,t)\ dy\ dz \tag{3.2}$$

where y is latitude, x is longitude, u is zonal velocity, z is depth, t is time, Z_u (Z_l) is upper (lower) boundary of the flow, Y_N (Y_S) is northern (southern) limit of the flow, and W is the half mean width of the flow.

The advantage of this method is that the transport calculation follows the current core avoiding artifacts if the current is meridionally migrating. In TRATL01 we choose the depth of the $24.5\,\mathrm{kg\,m^{-3}}$ neutral density surface as the upper boundary Z_u. This density surface represents the upper boundary of the NEUC during boreal winter, the season when the NECC is weak or not present and the NEUC can clearly be separated from the near-surface flow. The lower boundary Z_l is the depth of the $27.0\,\mathrm{kg\,m^{-3}}$ neutral density surface. A half mean width W of 2° is chosen for the NEUC. The

integration is performed between 42°W and 15°W. For the integration of the observational data slightly different boundary conditions are chosen to be consistent with the hydrographical conditions of the region. Z_u is the depth of the 24.5 kg m^{-3} and Z_l the depth of the 26.9 kg m^{-3} neutral density surface. The southern boundary is choosen as $Y_{CM} - 1.5°$ and the northern boundary is $Y_{CM} + 1.0°$. Note, if no hydrographic measurements are available for a single ship section, the neutral density field derived from the mean hydrographic section is used.

3.2.4 Conceptual model

We are using a conceptual model to investigate the oxygen response to specific circulation processes within the NEUC. It is based on the advection-diffusion model described in Brandt et al. (2010) which simulates an eastward current and its westward return flows with an oxygen source at the western boundary. The model equation (Eq. 3.3) used for all simulations throughout the study reads:

$$\frac{\partial C}{\partial t} = -aOUR - u\frac{\partial C}{\partial x} - v\frac{\partial C}{\partial y} + k_x\frac{\partial^2 C}{\partial x^2} + k_y\frac{\partial^2 C}{\partial y^2} + k_y F_{corr}\frac{\partial^2 C_{bg}}{\partial y^2} + k_z F_{corr}\frac{\partial^2 C_{bg}}{\partial z^2} \quad (3.3)$$

where C is the dissolved oxygen concentration, $aOUR$ the oxygen consumption, u and v the zonal and meridional velocity components, respectively, k_x and k_y the zonal and meridional eddy diffusivities, respectively, k_z the vertical eddy diffusivity, C_{bg} the constant large-scale background oxygen distribution, and F_{corr} a correction factor to the background oxygen curvature depending on the simulated oxygen concentration described below. The oxygen concentration at the western boundary C_0 is held constant at 147 μmol kg^{-1}, which is the mean oxygen concentration at the western boundary of the NEUC (γ_n = 26.5 kg m^{-3}, 2.5° − 6.5°N, 43°-47°W) derived from the MIMOC climatology (Schmidtko et al., 2017). In the model, the following 7 terms on the right hand side determine the oxygen tendency on the left hand side: (from left to right) (1) oxygen consumption, (2) zonal advection, (3) meridional advection, (4) zonal eddy diffusion, (5) meridional eddy diffusion associated with east- and westward jets and (6) meridional and (7) vertical eddy diffusion associated with the large-scale oxygen distribution in the upper 300 m between 0°N and 10°N.

The model parameters are tuned to fit a region covering an eastward current and its return flow between 2.5°N ($y = 0$) and 6.5°N ($y = l_y$) from 45°W ($x = 0$) to 10°W ($x = l_x$). For the idealized background flow field we use the same definition of the streamfunction as described in Brandt et al. (2010) and adjust it to fit the observations

in the NEUC regions.

$$u = u_0 \frac{l_x - x}{l_x} \cos\left(\frac{2\,\pi\,y}{l_y}\right), \qquad v = -\frac{u_0}{2\,\pi}\,\frac{l_y}{l_x} \sin\left(\frac{2\,\pi\,y}{l_y}\right) \tag{3.4}$$

where u_0 is the amplitude of the zonal jets at the western boundary. For steady state solutions, u_0 is held constant, whereas for some interannual variability simulations u_0 is multiplied with a time varying sinusoid.

Two modifications of the Brandt et al. (2010) model are realized. (i) We are using a constant, depth dependent oxygen consumption according to Karstensen et al. (2008), (ii) we modify the model parameters to correspond to the conditions of the NEUC region.

(i) The oxygen consumption used here is defined as the logarithmic function as given in Karstensen et al. (2008)

$$aOUR = c_1 + c_2 \cdot e^{-\lambda z} \tag{3.5}$$

($c_1 = -0.5$, $c_2 = 12$, $\lambda = 0.0021$). To avoid negative oxygen values, the consumption term is switched off when oxygen concentrations fall below 2 μmol kg^{-1}.

(ii) We fit our parameters to the 26.5 kg m^{-3} neutral density surface which corresponds to the core depth of the NEUC. A meridional and vertical eddy diffusion associated with the large scale oxygen distribution is derived from observations, as well as a correction factor for the background meridional diffusion as described below.

The NEUC is located in a region where oxygen concentrations are increasing equatorwards and decreasing polewards. Also in the vertical profile oxygen concentrations are changing within the NEUC. To account for this background oxygen field we estimate a meridional and vertical eddy diffusion associated with the meridional and vertical oxygen curvature in the observation at 23°W. We obtain the meridional eddy diffusion associated with the meridional oxygen distribution ($\frac{\partial^2 C_{bg}}{\partial y^2} = D_y$) similar to Brandt et al. (2010). We apply a second-order fit to the observed oxygen distribution along the 26.5 kg m^{-3} neutral density surface at 23°W between 0° and 10°N which results in $D_y = 1.55 \cdot 10^{-10}\,\mu$mol kg^{-1} m^{-2}. The vertical eddy diffusion associated with the vertical background oxygen distribution ($\frac{\partial^2 C_{bg}}{\partial z^2} = D_z$) is estimated by calculating the curvature of the mean vertical oxygen profile between 2.5°N and 6.5°N at 23°W. We obtain $D_z = 0.0112\,\mu$mol kg^{-1} m^{-2} for 130 m which corresponds to the depth of the 26.5 kg m^{-3} neutral density surface.

The correction factor for the background meridional diffusion is given as follows:

$$F_{corr} = \frac{C_0 - \overline{C_{23W}}}{C_0 - C_1} \tag{3.6}$$

where C_0 is the oxygen concentration at the western boundary ($147\,\mu\mathrm{mol\,kg^{-1}}$), C_1 is the observed mean oxygen concentration along 23°W between 2.5°N and 6.5°N ($108\,\mu\mathrm{mol\,kg^{-1}}$) and $\overline{C_{23W}}$ is the corresponding simulated value. This factor acts to damp changes of oxygen due to the background eddy diffusivity depending on the meridional and vertical oxygen curvature. That means if $\overline{C_{23W}}$ is higher (lower) than C_1 the oxygen supply because of the background eddy diffusion decreases (increases).

The coefficients of the horizontal and the vertical eddy diffusion are chosen based on previous observational studies. We use a vertical diffusivity of $k_z = 10^{-5}\,\mathrm{m^2\,s^{-1}}$ (Banyte et al., 2012; Fischer et al., 2013; Köllner et al., 2016). Hahn et al. (2014) suggested a meridional diffusivity k_y of $500 - 1400\,\mathrm{m^2\,s^{-1}}$ between 100-300 m depth. Globally, previous studies suggest an anisotropy between zonal and meridional diffusivities with zonal diffusivity larger than meridional (Banyte et al., 2013; Eden, 2007; Eden and Greatbatch, 2008; Kamenkovich et al., 2009). Brandt et al. (2010) found that $k_y = 200\,\mathrm{m^2\,s^{-1}}$ and $k_x = 2.5 \times k_y$ (k_x is the zonal diffusivity) best fits the observations in the ETNA OMZ (~ 400 m depth). Here, we calculate the equilibrium state for different k_y and k_x. We found that a meridional eddy diffusivity of $k_y = 800\,\mathrm{m^2\,s^{-1}}$ with no anisotropy (i.e. $k_x = k_y$) and $u_0 = 0.055\,\mathrm{m\,s^{-1}}$ results in oxygen concentrations along 23°W that best matches observations (Fig. 3.S1a,c). In the following we will refer to this simulation as SIM 1.

3.3 Results

The interannual variability of the NEUC and its impact on the oceanic oxygen distribution is investigated using ship observations along 23°W and the output of TRATL01. First we briefly validate and discuss the zonal velocity and oxygen sections along 23°W TRATL01. Then we present the results of the interannual variability of the NEUC in TRATL01 before we focus on the oxygen response associated with NEUC variability. Finally, we present the results of the conceptual model to understand the role of specific mechanisms.

3.3.1 Mean velocity and oxygen section along 23°W

In the mean ship section along 23°W, below the mixed layer, higher oxygen concentrations locally coincide with the eastward flowing EUC, NEUC and nNECC at 0°N,

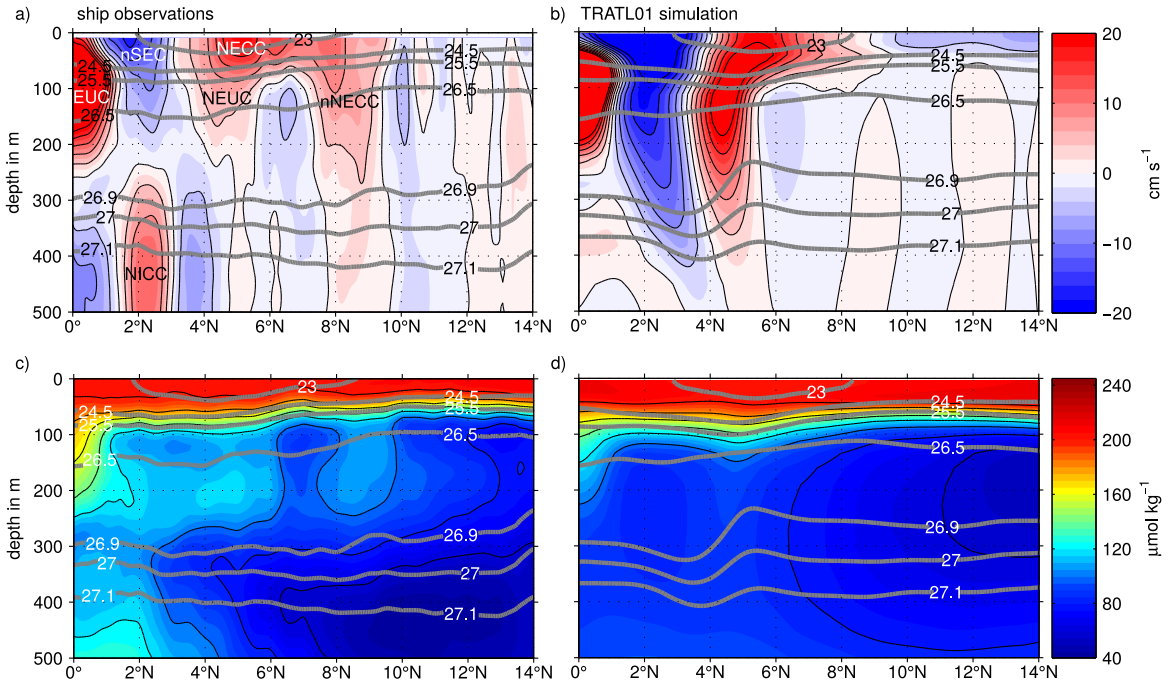

Figure 3.2: (a, b) Zonal velocity and (c, d) oxygen concentrations along 23°W from (a, c) observations and (b, d) the output of TRATL01. The observed velocity field (a) is an averaged of 21 ship sections along 23°W from 2002 to 2018 and the observed oxygen field (c) is an average of 11 ship section along 23°W from 2006 to 2018. The TRATL01 output (b, d) is an averaged of the last 14 years of the model run (1994-2007) along 23°W. (a,b) Eastward velocities are positive (red), westward are negative (blue). Grey contours mark neutral density surfaces (kg m^{-3}). Currents in a) are the Equatorial Undercurrent (EUC), the northern branch of the South Equatorial Current (nSEC), the North Equatorial Countercurrent (NECC) and its northern branch (nNECC), the North Equatorial Undercurrent (NEUC), and the North Intermediate Countercurrent (NICC).

4.5°N and 8.5°N respectively, whereas the westward flows centered at 2.5°N and 6.5°N are associated with lower oxygen concentrations (Fig. 3.2a,c). The core of the ETNA OMZ with oxygen concentrations of 40 μmol kg^{-1} is located between 400 m and 500 m and between 9°N and 13°N. In the upper 250 m south of 6°N, oxygen concentration are in general higher than north of 6°N. This is associated with the more energetic zonal flow in the near-equatorial belt including the NEUC.

From the observed zonal velocity field the NEUC intensity (INT, Eq. 3.2) and central position (Y_{CM}, Eq. 3.1) are calculated and averaged in two different ways: (i) They are calculated using the mean ship section. Here, the averaged NEUC intensity is 1.2 Sv and the current is on average located at 4.9°N. (ii) The estimates of the single ship sections are averaged. This results in an average intensity of 2.6 $\pm$ 0.4 Sv and

an averaged central position of 5.0 ± 0.1°N (Tab. 3.2). Method (ii), which results in higher values, is more consistent with the method used for the model output.

Similar to the observations, oxygen concentrations along 23°W in TRATL01 are increased in the presence of eastward flow and decreased in the presence of westward flow (Fig. 3.2b,d). The NEUC in TRALT01 is on average more than twice as strong as in the observations and its core is located a bit further south. The mean NEUC intensity at 23°N (1990-2007) is 7.4 ± 0.3 Sv and its mean central position is 4.44 ± 0.03°N. The model is overestimating the strength and depth range of the NEUC and the nSEC whereas weaker eastward current bands such as the NICC and the nNECC are not well represented by the model.

In TRATL01 oxygen concentrations below the mixed layer are generally lower, the oxygen minimum zone is located shallower, and the difference between local oxygen maxima and minima is smaller compared to observations. The core of the OMZ in TRATL01 is 200 m shallower than in observations. Also the deep oxygen maximum at the equator is not well represented in TRATL01. Although the NEUC is stronger, oxygen concentrations within the NEUC region at 23° W ($100 - 300$ m depth, $3° - 6.5°$N) are lower in TRATL01 ($93.4 \pm 0.8\,\mu$mol kg^{-1}) compared to observations ($106.0 \pm 1.5\,\mu$mol kg^{-1}).

Different mechanisms seem to dominate the NEUC mean state in observations and in TRATL01. Not only the NEUC is very strong in TRALT01, but also the nSEC south of it. One explanation for that can be a too strong recirculation between nSEC and NEUC. In the ship section from February 2018, a temporary recirculation between the nSEC and NEUC seems to exist (black dashed rectangles in Fig. 3.1b,c). Here, the velocity maximum between 3°N and 5°N in the depth range of 50 m to 300 m is associated with rather low oxygen and it is located above and south of the NEUC associated oxygen maximum. It is likely that this eastward velocity maximum is a temporary recirculation of the nSEC which overlaps with the actual NEUC flow. This results in lower oxygen values associated with higher eastward NEUC velocities. An overestimation of this process by TRATL01 could result in the shown discrepancies between model and observations. Strong recirculation between EUC, NEUC and nSEC are also shown in other model studies such as Hüttl-Kabus and Böning (2008).

In summary, distinct discrepancies exist between simulated and observed zonal velocities and oxygen concentration in the mean sections along 23°W. A potential cause for the differences in the mean state is an overestimation of the recirculation between nSEC and NEUC in TRATL01. Nevertheless, we want to emphasize here that the horizontal oxygen distribution is clearly improved in TRATL01 compared to coarser resolution

models (Duteil et al., 2014). How the erroneous representation of the mean state in TRATL01 affects the NEUC and associated oxygen changes on interannual timescales will be investigated in section 3.3.4. Before we focus on the oxygen response to the NEUC we investigate the variability of NEUC transports and central position. In the next section we briefly study the seasonal cycle of the NEUC in observations and in TRATL01.

3.3.2 Seasonal cycle of NEUC intensity (INT) and central position (Y_{CM})

In the previous section we found that on average the NEUC is too strong in TRATL01 but simultaneously shows a weaker oxygen maximum along 23°W compared to observations. We hypothesize that this might be due to an overestimation of the recirculations between nSEC and NEUC in TRALT01. Here, we focus on the seasonal cycle of the NEUC in observations and in TRATL01.

The NEUC transport estimates derived from the observational data are highly variable and show no clear seasonal signal (Tab. 3.2 and black dots in Fig. 3.3a). This is in agreement with previous observational results (Schott et al., 1995; Bourlès et al., 1999a, 2002; Schott et al., 2003; Urbano et al., 2008; Brandt et al., 2006). The current is weak and likely to be obscured by mesoscale activities (e.g. Weisberg and Weingartner, 1988; Goes et al., 2013) and interannual variability (Goes et al., 2013; Hüttl-Kabus and Böning, 2008). Even with this unique data set of 21 ship sections, observations are still too sparse to identify a seasonal variability of the NEUC.

In TRATL01, the NEUC shows a clear seasonal cycle. Along 23°W, the NEUC reaches its maximum intensity of 11.4 Sv in May and its minimum intensity of 3.9 Sv in November (red line in Fig. 3.3a). Its central position shows a semiannual cycle with southernmost positions in September and January and northernmost positions in May and November (Fig. 3.3b). The semiannual cycle of NEUC central position is not visible at all longitudes (Fig. 3.3d). The seasonal signal of NEUC INT and Y_{CM} is propagating from the eastern boundary towards the west (Fig. 3.3c,d). Highest standard deviations of NEUC transports occur during May and June in the eastern basin and during July and August in the western basin (black contours in 3.3c). Maximum standard deviation of NEUC transports seems to be associated with the seasonal weakening of the NEUC.

The seasonal cycle of the NEUC in TRATL01 is in good agreement with previous studies. Hüttl-Kabus and Böning (2008) also found a more northward position and higher transports between April and August and a more southward position and lower

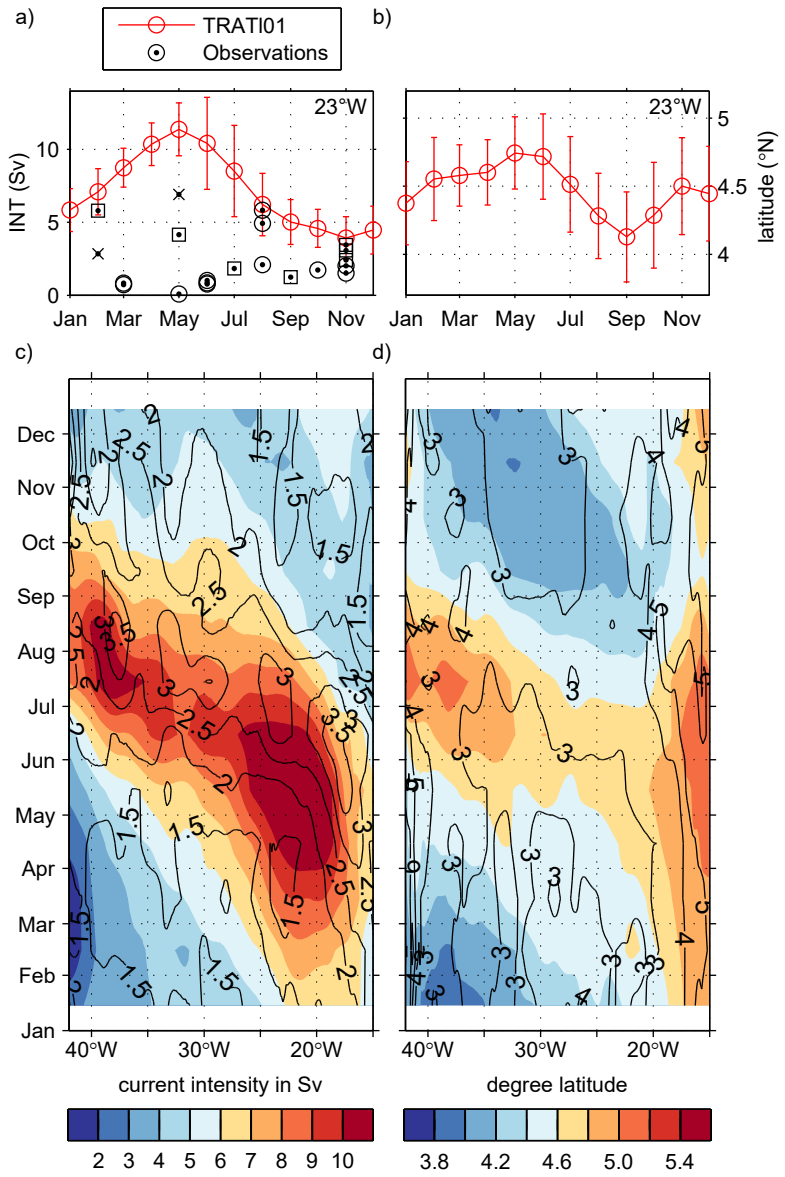

Figure 3.3: Seasonal cycle of (a) NEUC intensity (INT) and (b) NEUC central position (Y_{CM}) at 23°W derived from TRATL01 (red lines, 1958-2007) as well as NEUC INT derived from each ship section (black dots in a; circles, squares and crosses mark years of neutral, negative and positive AMM phases, respectively). The red bars denote the standard deviations of NEUC INT and Y_{CM} in TRALT01 of the respective months from 1958 to 2007. Hovmöller diagram of the 1958-2007 seasonal cycle of (c) INT and (d) Y_{CM} in TRATL01 for each longitude. The black contours show the standard deviation of (c) INT in Sv and (d) Y_{CM} in degree latitude for each month from 1958 to 2007.

Table 3.2: NEUC INT (Sv), Y_{CM} (°N) and oxygen (μmol kg^{-1}) derived from observations along 23°W from 2002 to 2018. The oxygen values are derived in two ways. (i) The values are average in a meridionally varying frame (100-300 m depth, $(Y_{CM}-1.5)$° - $(Y_{CM}+1)$°N). (ii) The values are averaged in a fixed box (100-300 m depth, 3°-6.5°N). The state of the AMM is marked for positive events (+), negative events (−), and neutral phases (∘). For the mean values derived from the single ship sections the standard error is given.

Date	Y_{CM}	INT	(i) O_2	(ii) O_2	AMM
2002 Oct	4.38	1.73			∘
2003 Aug	4.79	4.93			∘
2006 Jun	5.36	0.76	107.2	106.5	∘
2006 Jun	5.22	1.02	108.5	108.9	∘
2006 Jun	4.95	0.84	111.9	109.2	∘
2008 Mar	5.41	0.83	105.2	104.8	∘
2008 Mar	5.53	0.72			∘
2009 Jul	5.25	1.83			−
2009 Nov	4.47	2.42	106.1	103.7	−
2009 Nov	4.63	3.07			−
2010 Feb	4.60	2.84			+
2010 May	5.02	6.91			+
2011 May	4.96	0.08			∘
2011 Aug	5.24	5.83			∘
2012 Nov	5.12	2.02	98.1	96.6	∘
2012 Nov	4.83	1.51			∘
2014 May	4.71	4.15	96.5	100.8	−
2014 Nov	4.76	3.45	104.7	104.5	−
2015 Sep	5.60	1.25	114.1	115.4	−
2016 Aug	4.49	2.10	110.0	108.1	∘
2018 Feb	4.74	5.80	108.5	107.2	−
mean of single sections	4.96 ± 0.08	2.58 ± 0.42	107.1 ± 1.8	106.0 ± 1.5	
mean section	4.84	1.36	107.7	106.1	

transports between September and March in their model simulation. The seasonal cycle of NEUC transport estimates in TRATL01 is also consistent with the synthesis product of Goes et al. (2013). Similar to Goes et al. (2013), we found a semiannual cycle of the NEUC central position along 23°W, although the timing of maxima and minima is shifted by up to 2 months. We found minima in September and January and maxima in May and November, whereas in Goes et al. (2013) minima occur in September and March and maxima in August and December. In general, the seasonal strengthening

of the eastern NEUC in TRATL01 seems to coincide with the northward migration of the Intertropical Convergence Zone (ITCZ) and the shoaling of the thermocline in the eastern equatorial Atlantic (Xie and Carton, 2004).

In summary, a seasonal and longer term variability of the NEUC in observations can not be identified. In TRATL01 the NEUC shows a clear seasonal cycle which is in general agreement with previous studies. This encourages us to study the interannual variability of the NEUC in the next section.

3.3.3 Interannual variability of NEUC

The NEUC transport and central position vary on interannual to multidecadal timescale in TRATL01 (Fig.3.4). However, TRATL01 is driven by CORE v2 wind forcing that is based on NCEP winds. The CORE forcing as well as the NCEP wind is known to exhibit spurious multidecadal wind variability (Hurrell and Trenberth, 1998; Fiorino, 2000; He et al., 2016). We therefore focus on the interannual variability of the NEUC in TRATL01.

NEUC transport and central position show a positive correlation in TRATL01. To analyze the correlation, we zonally averaged NEUC INT and Y_{CM} from 42°W to 15°W and removed the seasonal cycle from 1958 to 2007 (blue lines in Fig. 3.4). To better understand the role of interannual variability of the NEUC, we applied a 1-to-5-years band-pass Butterworth filter to INT and Y_{CM} (black lines in Fig. 3.4). Higher NEUC transports are generally associated with a more northward position of the NEUC and vice versa with a significant positive correlation between the band-pass filtered time series of $R = 0.33$.

Previous studies suggest the upwelling in the Guinea Dome and along the Northwest African coast in the ETNA as a possible driver of the NEUC (Furue et al., 2007, 2009) and that changes in the wind field can impact the upwelling which in turn leads to changes in the NEUC (Goes et al., 2013). To investigate this connection we perform a linear regression of the band-pass filtered NEUC INT onto the wind stress curl using monthly time series regressed at lag 0 (Fig. 3.5). On interannual time scales, the wind stress curl explains up to 40 % of the NEUC variability. Maximum positive correlation ($R = 0.6$) is found in the eastern basin of the tropical North Atlantic between 2°N and 8°N and in the western basin of the tropical South Atlantic between 0° and 8°S. This large scale wind pattern may not only impact the strength of the NEUC, but also effect the basin wide circulation. We therefore regressed the wind stress curl on the NEUC and calculate the anomalous Sverdrup streamfunction from the derived slope b times a

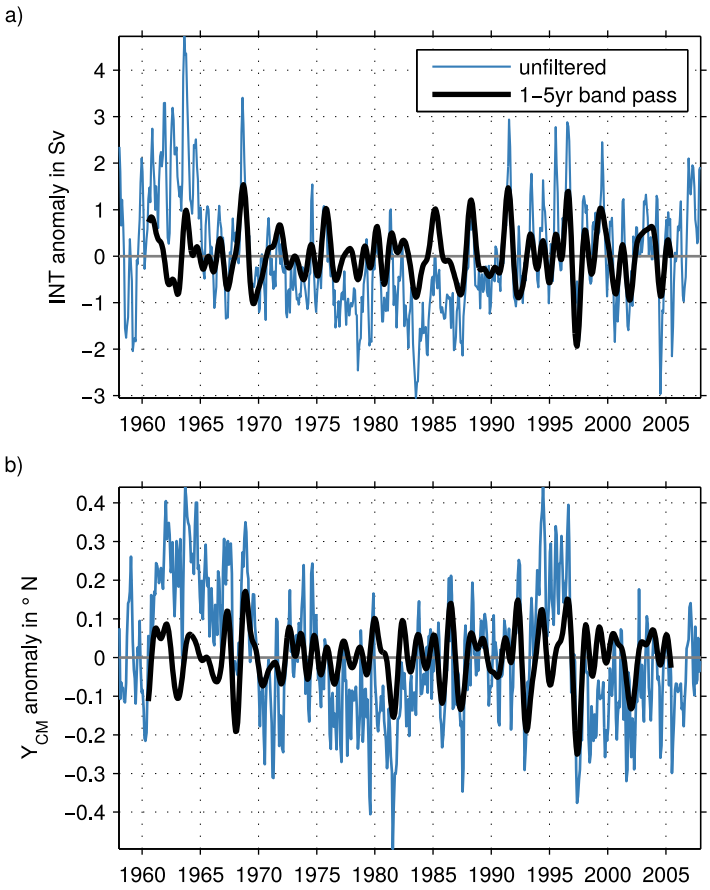

Figure 3.4: Zonally averaged (42°-15°W) monthly mean anomaly of (a) NEUC INT (Eq. 3.2) and (b) Y_{CM} (Eq. 3.1) with respect to the 1958-2007 seasonal cycle estimated from TRATL01. A 1-5-year band-pass (black line) Butterworth filter is applied to the zonally averaged time series (blue lines).

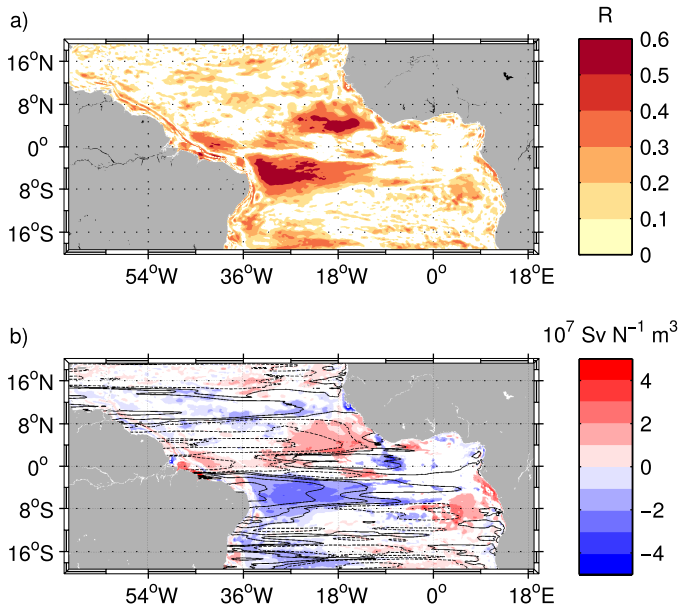

Figure 3.5: Linear regression of 1-5-years band-pass filtered NEUC *INT* onto wind stress curl from TRATL01. (a) Coefficient of correlation and (b) slope of the linear regression. Contours in b) presents the anomalous Sverdrup circulation forced by a wind stress curl anomaly that causes a NEUC transport anomaly of 1 Sv. The black solid lines mark the 0 Sv, 0.1 Sv, 0.4 Sv and 1 Sv isoline and the black dashed lines mark the -0.1 Sv, -0.4 Sv and -1 Sv isoline.

unit transport of 1 Sv.

During a strong (weak) NEUC the derived anomalous Sverdrup streamfunction is associated with a westward (eastward) velocity anomaly between 8°N and 10°N and an eastward (westward) velocity anomaly just south off the equator (Fig. 3.5). At the western boundary the closure of the anomalous Sverdrup streamfunction would result in a southward (northward) and northward (southward) velocity anomaly north and south of the equator, respectively. Between 40°W and 10°W just north of the equator the wind stress curl anomaly leads to an anomalous northward (southward) Sverdrup transport. To further investigate the relationship between the NEUC and the large scale wind field we perform a composite analysis regarding the wind and SST field during strong and weak NEUC transports.

The band-pass filtered time series of NEUC *INT* is used to define years of strong and weak NEUC flow. As threshold 0.6 times its standard deviation is chosen (green line in Fig. 3.6a). Then composites of SST and the wind field are calculated for years of strong and weak NEUC transports (Fig. 3.6b,c). The composites show an inter-hemispheric SST gradient with opposite sign for strong and weak NEUC transports.

Associated are wind anomalies pointing from the colder hemisphere towards the warmer hemisphere. These are the characteristics of the AMM as described in the introduction. The interannual NEUC variability is negatively correlated with the AMM. A positive AMM is associated with a weaker and more southern NEUC, and the negative AMM is associated with a stronger and more northern NEUC.

The anomalous inter-hemispheric winds during an AMM event link the interannual variability of the NEUC to the AMM. Associated with a positive (negative) AMM event is a negative (positive) wind stress curl anomaly along the equator and just north of it east of 20°W (Joyce et al., 2004; Foltz and McPhaden, 2010b). We find a similar wind pattern for weak and strong NEUC, respectively (Fig. 3.5). The large-scale wind pattern does not only effect the NEUC flow but also effects the basin-wide Sverdrup circulation in the tropical Atlantic (Fig. 3.5). The anomalous northward Sverdrup transport between 40°W and 10°W just north of the equator might impact the recirculation between the NEUC and the nSEC. Furthermore, along the Northwest African coast south of 15°N, we find alongshore wind stress that act to weaken (strengthen) coastal upwelling during weak (strong) NEUC transports (Fig. 3.6).

In summary, in TRATL01 the interannual variability of the NEUC is linked to the AMM, likely due to its associated large-scale wind anomalies. Consistent with the results of Goes et al. (2013), we find a strengthening and a more northward position of the NEUC during negative AMM events and vice versa. The anomalous wind stress curl additionally impacts the Sverdrup circulation between 10°S and 10°N. The response of oxygen to the interannual changes of the NEUC in TRATL01 is investigated in the next section.

3.3.4 NEUC impact on oxygen

On interannual time scales the NEUC variability is linked to the AMM in TRATL01. During positive AMM events, the NEUC transports are weaker and the current core is displaced towards the south. During negative AMM events, the NEUC is stronger and displaced towards the north. In this section we investigate the impact of the interannual NEUC variability on oxygen. Brandt et al. (2010) suggest that weaker NEUC transports lead to lower oxygen concentrations at 23°W due to a weaker advection of oxygen-rich water masses from the western boundary. Consequently, we expect lower oxygen concentrations after positive AMM events and vice versa. The observational data show no clear connection between oxygen concentration, NEUC transports and the AMM (Fig. 3.S2). We will therefore focus on the interannual variability of oxygen

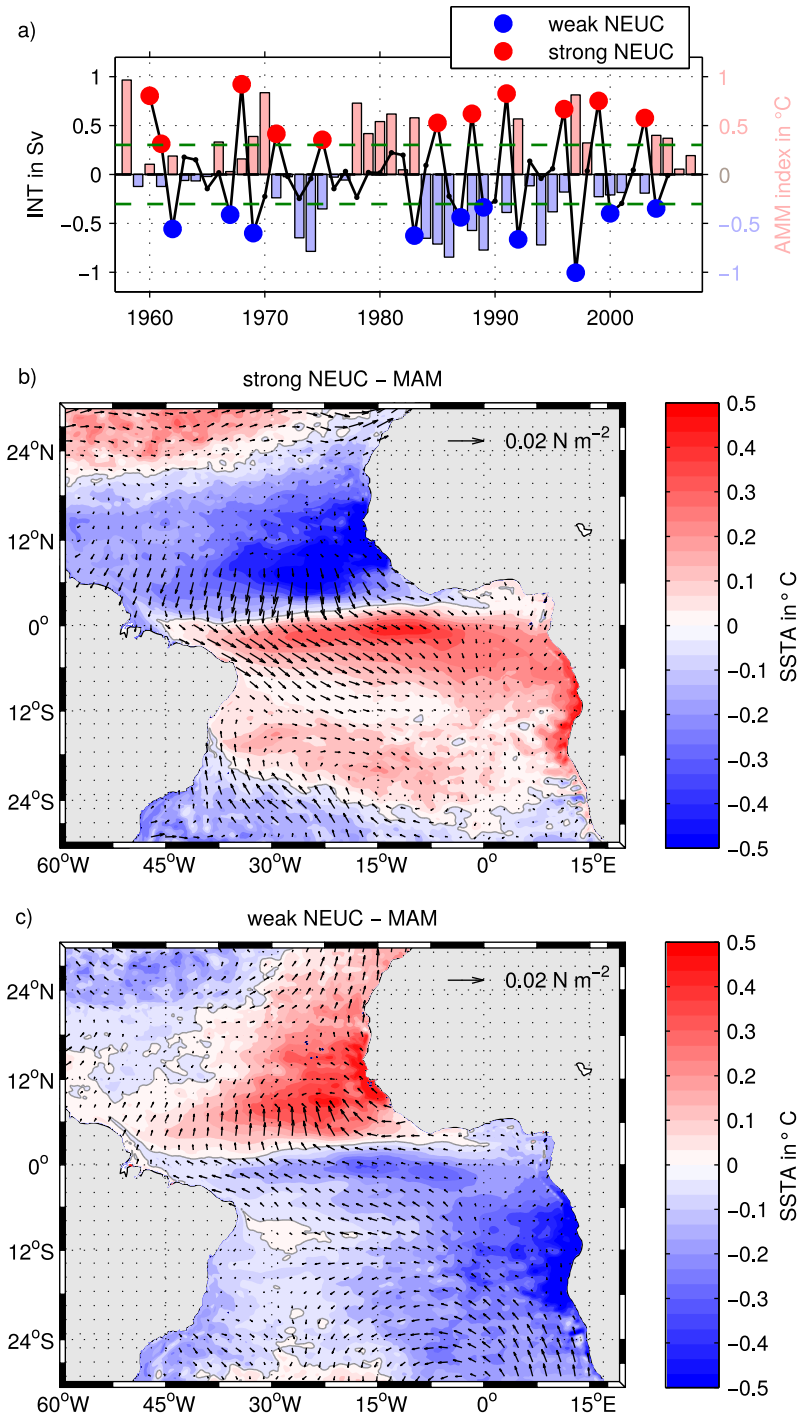

Figure 3.6: (a) Annual mean of NEUC *INT* anomaly averaged between 42°W and 14°W. An 1-5-years band-pass filter is applied to the time series (left y-axis). The green dashed line marked ±0.6 times the standard deviation of the time series. Red dots mark years of strong NEUC *INT*, blue dots mark years of weak NEUC *INT*. The bars show the March to May averages of the AMM index after Servain (1991) (right y-axis). Composites of anomalous SST (color shading) and surface wind stress (arrows) for years of (b) strong and (c) weak NEUC *INT*.

in TRATL01.

In TRATL01 the oxygen variability is analyzed along three characteristic neutral density (γ_n) surfaces of the NEUC. We choose the 25.5 $\mathrm{kg\,m^{-3}}$ surface for the upper part of the NEUC, the 26.5 $\mathrm{kg\,m^{-3}}$ surface for the central part of the NEUC, and the 26.9 $\mathrm{kg\,m^{-3}}$ surface for the lower part of the NEUC (Fig. 3.2). The mean oxygen concentrations and horizontal velocities along all three γ_n surfaces of the period 1990 to 2007 are shown in Figure 3.7. Along the upper γ_n surface in the area of the nSEC and NEUC low oxygen concentrations exist (Fig. 3.7a). Interestingly, minimum oxygen concentrations are found in the western basin in the area of the nSEC supplying the eastward flow within the NEUC. This suggests that the water masses in the upper NEUC in TRATL01 are only weakly connected to the oxygen-rich waters in the western boundary and are instead provided largely out of the recirculation between NEUC and nSEC. A possible mechanism causing the low oxygen values along the 25.5 $\mathrm{kg\,m^{-3}}$ surface close to the western boundary might be a too weak or inexistent intermediate current system in TRATL01. This would lead to a too low ventilation at depth which again can result in an upward flux of low-oxygen waters towards the surface due to either diapycnal mixing or vertical advection within the subthermocline cells (Wang, 2005; Perez et al., 2014).

Along the 26.5 $\mathrm{kg\,m^{-3}}$ surface oxygen concentration are high in the western basin and low in the eastern basin (Fig. 3.7b). At the northern flank of the NEUC and north of it a tongue of high oxygen concentrations spreads towards the east. At the southern flank of the NEUC and within the nSEC a tongue of low oxygen spreads towards the West. The mean horizontal current field in combination with the oxygen concentrations indicates that the NEUC in TRATL01 is partly supplied by water masses from the western boundary and partly by water masses from the nSEC. This supports our previous hypothesis that in TRATL01 a constant recirculation between nSEC and NEUC superimposed on a mean eastward current results in a strong NEUC flow that is associated with low oxygen levels, as it is supplied by the oxygen-poor water masses out of the nSEC.

At the lower part of the NEUC (26.9 $\mathrm{kg\,m^{-3}}$ surface) a tongue of high oxygen concentration centered at the NEUC spreads from the western to the eastern basin (Fig. 3.7c). Here, the ventilation of the NEUC by the western boundary seems to dominate the water supply of the NEUC with only weak recirculation occurring along the eastward path of the NEUC. Note that eastward flow of waters with higher oxygen concentrations associated with the NEUC reaches the eastern boundary north of 6°N.

To investigate interannual variability of oxygen in TRATL01 the seasonal cycle is

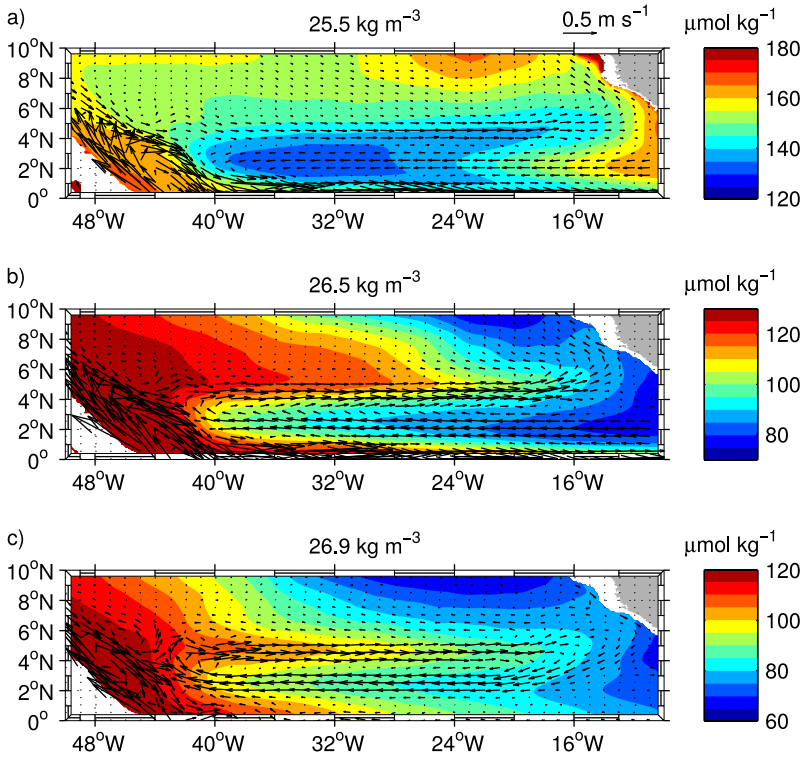

Figure 3.7: Mean oxygen concentration (shading) and horizontal velocities (arrows) for the period 1990 to 2007 along three characteristic isopycnals (25.5 kg m^{-3}, 26.5 kg m^{-3}, and 26.9 kg m^{-3}) of the NEUC in TRALT01.

removed from the oxygen field and a 5-years high-pass Butterworth filter is applied to the annual averaged oxygen anomalies. Similar to the SST and wind stress analysis, composites of oxygen and horizontal velocity for strong and weak NEUC transports are calculated (Fig. 3.8). We now focus on the oxygen variability along the 26.5 kg m^{-3} surface representing the core depth of the NEUC in TRATL01.

At a first glance, the oxygen anomalies associated with the NEUC variability in TRATL01 appear to be counterintuitive. Along the 26.5-isopycnal during years of weak NEUC, positive oxygen anomalies exist along the NEUC path with a connection to the southwestern boundary (Fig. 3.8a). For years of strong NEUC flow, negative oxygen anomalies occur along the NEUC path instead (Fig. 3.8b). This is the opposite of what we would have expected taken into account the mean velocity and oxygen fields along 23°W.

Again, a too strong recirculation between the nSEC and NEUC might explain the oxygen pattern in TRALT01. The composites analysis shows that during weak (strong) NEUC flow, also the nSEC is weak (strong) and is transporting less (more) oxygen-poor water to the western basin (Fig. 3.8). Associated is a weaker (stronger) than nor-

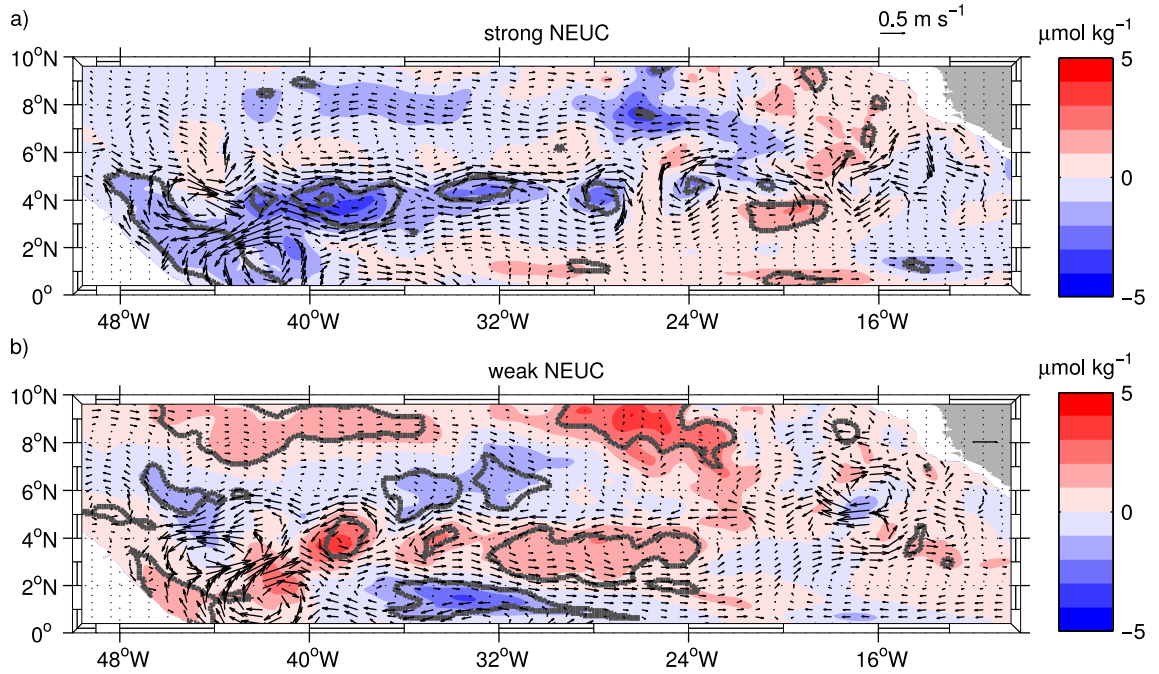

Figure 3.8: Anomalous oxygen concentrations (shading) and horizontal velocities (arrows) for years of strong (a) and weak (b) NEUC flow along the 26.5 kg m^{-3}-isopycnal in TRATL01. The annual mean data was 5-years high-pass filtered. Areas within the gray contour lines mark oxygen anomalies that are significant at a 95% confidence level.

mal recirculation between NEUC and nSEC and the NEUC is supplied by less (more) oxygen-poor water from the nSEC. Additionally a weak (strong) nSEC is transporting less (more) oxygen-poor water to the western basin. Positive (negative) oxygen anomalies develop in the western basin, which may be then advected by the NEUC towards the east.

In the oxygen composites, anomalies occur in the entire tropical North Atlantic which might be associated with the detected large-scale wind anomalies during anomalous NEUC transports. For example, weak negative (positive) oxygen anomalies exist along the western boundary during strong (weak) NEUC phases and cover a depth range of 50 m to 450 m depth. These oxygen anomalies are associated with weak meridional velocity anomalies that act to weaken (strengthen) the NBC and its return flow. This pattern could be related to the closure of the Sverdrup circulation at the western boundary (Fig. 3.5b). The wind-field during strong (weak) NEUC and negative (positive) AMM events acts to weaken (strengthen) the NBC just north of the equator so that less (more) oxygen-rich water might be supplied there. Furthermore negative (positive) oxygen anomalies during strong (weak) NEUC flow exist also north of 7°N. Here, we find westward (eastward) velocity anomalies in the anomalous Sverdrup streamfunction

at about 8°N that are also visible in Figure 3.8. This westward (eastward) velocity anomaly act to weaken (strengthen) the nNECC which again could explain the oxygen anomalies there.

In contrast to our expectations, the NEUC strength and the oxygen concentrations along its flow path are negatively correlated on interannual timescales in TRATL01. To get a rough estimate of how much of the oxygen variability can be explained by the NEUC variability we perform a lagged linear regression of oxygen on NEUC INT for the 1-5 years band-pass filtered time series (Fig. 3.9). The linear regression supports the results from the composite analysis, i.e. a negative correlation between oxygen and NEUC in TRATL01 (Fig. 3.9). Highest values of R occur along and slightly south of the NEUC pathway mainly between 42°W and 24°W (Fig. 3.9a-d). Here, on average the NEUC variability can explain between 20% and 40% of the oxygen variability. Maximum R values occur just south of the NEUC west of 36°W when the NEUC leads the oxygen by 3 month. This hints again toward the relationship between nSEC and NEUC. If the nSEC is weak, less oxygen-poor water is transported towards the west leading to a positive oxygen anomaly there that is maximum 3 months after nSEC is weakest. Striking is also the high correlation near the equator in Figure 3.9e suggesting that the oxygen variability there leads the NEUC variability further north. A possible explanation might be that the variability of the near-equatorial flow is leading the variability of the NEUC. A lead-lag correlation between NEUC INT and the zonal velocity show eastward velocity anomalies along the equator leading an anomalous strong NEUC by 3 months, but the correlation is low.

We here want to briefly discuss the role of respiration for oxygen variability. Generally, respiration can be another mechanism changing the oxygen concentration. However, on interannual time scales the variability of respiration in TRATL01 is too small to have a significant effect on oxygen. This is consistent with other studies showing that circulation changes are the dominant mechanism setting the variability of oxygen levels on seasonal and multidecadal timescales (Montes et al., 2014; Vergara et al., 2016; Pozo Buil and Di Lorenzo, 2017; Yang et al., 2017).

In summary, NEUC transports and oxygen concentrations along its pathways are anti-correlated on interannual time scales in TRATL01. This is in contrast to the conclusion drawn from observations (Brandt et al., 2010), where a stronger NEUC is associated with higher oxygen concentrations. The results of this section motivates us to four experiments with a conceptual model that are described in the next section.

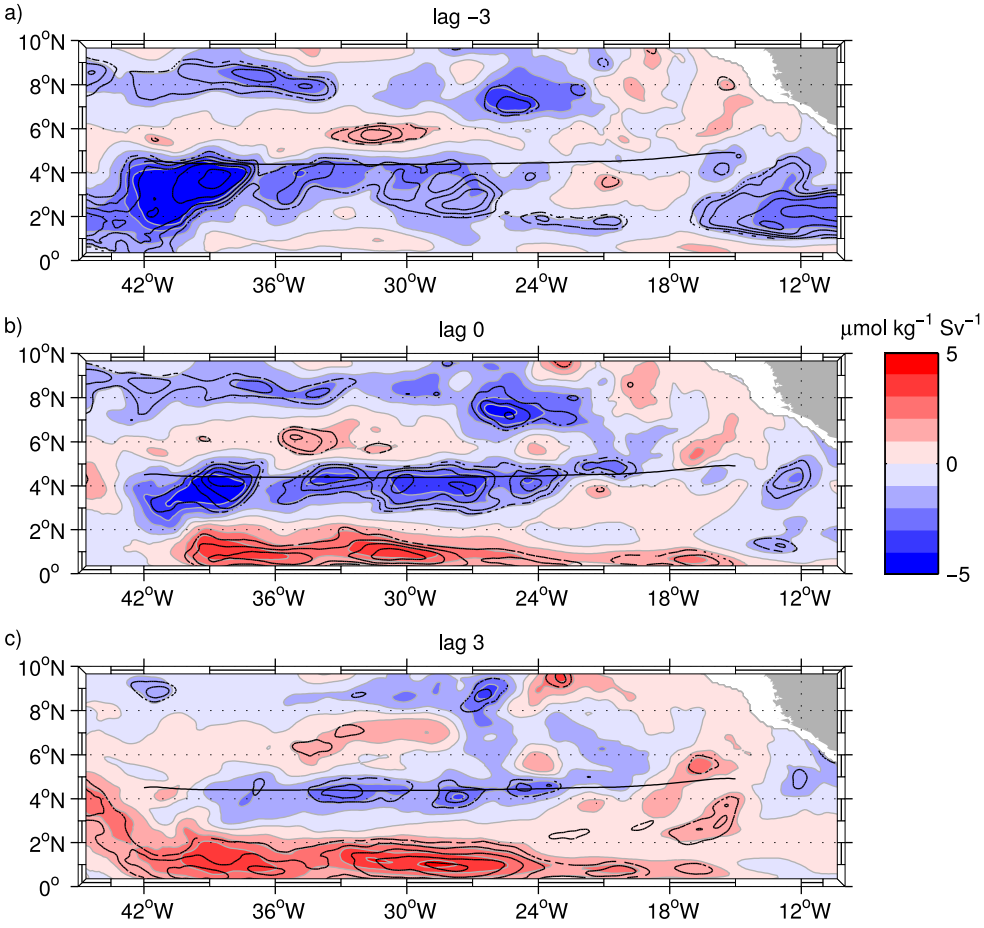

Figure 3.9: Linear regression of TRATL01 oxygen concentrations along the 26.5 kg m^{-3}-isopycnal on NEUC INT. Shading marks the slope of linear regression for a lag of -3 months (a; NEUC leads oxygen), zero lag (b), and a lag of +3 months (c; oxygen leads NEUC). Negative values of the slope indicate an anti-correlation between NEUC and oxygen, i.e. oxygen is low when the NEUC transport is strong. Black contours mark the significant values of the coefficient of determination (0.1 interval starting at 0.4). Black line marks mean position of the NEUC.

3.3.5 Conceptual model

The conceptual model is used to investigate single processes that appear to be active in the observations and/or in TRATL01. These processes potentially impact the NEUC, its variability and the associated oxygen distribution. In addition to our reference experiment SIM 1, we perform 4 experiments (SIM 2 and VAR 1-3) with the conceptual model. First, we want to test how a mean recirculation between NEUC and nSEC affects the oxygen concentrations (SIM 2). Furthermore, we calculate the oxygen response for three possible scenarios: (i) A stronger mean NEUC that is associated with enhanced

ventilation from the western boundary and hence, positive oxygen anomalies along the NEUC (VAR 1). (ii) A stronger NEUC due to a stronger recirculation with the nSEC which is associated with negative oxygen anomalies in the NEUC (VAR 2). (iii) An oxygen variability of the source waters at the western boundary, which is then advected by the unchanged NEUC towards the east (VAR 3). The experiments are based on the conceptual model (Eq. 3.3) with the horizontal eddy diffusivities $k_x = k_y = 800\,\mathrm{m^2\,s^{-1}}$ and the background flow field given by Eq. 3.4 with $u_0 = 0.055\,\mathrm{m\,s^{-1}}$. The design and the results of the 4 experiments are discussed in the following. Table 3.3 gives an overview over all the simulations.

The discrepancies of the mean state in TRATL01 and observations motivates our first experiment SIM 2. To study the impact of a recirculation between NEUC and nSEC on the oxygen distribution the following elliptical velocity field is superimposed on the background flow field (Eq. 3.4) centered between the NEUC and nSEC:

$$\begin{aligned} u &= \begin{cases} 0.5 \cdot u_1 \cdot \cos\left(\frac{2\pi \cdot y}{ly}\right) \cdot \left(\cos\left(\frac{2\pi \cdot x}{l_x}\right) - 1\right) & \text{if } 0 \le y \le \frac{1}{2}\, l_y \\ 0 & \text{else} \end{cases} \\ v &= \begin{cases} 0.5 \cdot u_1 \cdot \frac{ly}{lx} \cdot \sin\left(\frac{2\pi \cdot y}{ly}\right) \cdot \sin\left(\frac{2\pi \cdot x}{l_x}\right) & \text{if } 0 \le y \le \frac{1}{2}\, l_y \\ 0 & \text{else} \end{cases} \end{aligned} \tag{3.7}$$

where u_1 is the velocity amplitude of the recirculation ($u_1 = u_0$ for steady state simulations). In this experiment the recirculation acts to homogenize the horizontal oxygen distribution in the central and eastern basin resulting in lower oxygen concentration west and in higher oxygen concentration east of about 20°W compared to SIM 1 (Fig. 3.10 and Fig. 3.S1). In SIM 2 maximum zonal velocities occur in the center of the basin and not at the western boundary as in SIM 1. This enables the nSEC to advect more oxygen-poor water from the eastern boundary towards the west which again hampers the eastward advection of oxygen-rich water by the NEUC and results in a strong zonal oxygen gradient west of 35°W. Simultaneously, east of 35°W the recirculation acts to homogenize the oxygen distribution resulting in a weak horizontal oxygen gradient. Consequently, we found lower oxygen concentrations west of 23°W and higher oxygen concentration east of it compared to SIM 1 and observations (Fig. 3.S1).

The results of SIM 2 suggest that a recirculation between the NEUC and nSEC acts to weaken the oxygen maximum associated with the NEUC. However, the recirculation in SIM 2 leads to a better ventilation of the basin east of 23°W compared to SIM 1. This

Table 3.3: Overview over the different simulations performed with the conceptual model (Eq. 3.3).

simulation	flow field	velocity amplitude	oxygen at western boundary
SIM 1	Eq. 3.4	$u_0 = 0.055\,\mathrm{m\,s^{-1}}$	$C_0 = 147\mu\mathrm{mol\,kg^{-1}}$
SIM 2	Eq. 3.4 + Eq. 3.7	$u_0 = u_1 = 0.035\,\mathrm{m\,s^{-1}}$	$C_0 = 147\mu\mathrm{mol\,kg^{-1}}$
VAR 1	Eq. 3.4	$u_0 = 0.055\,\mathrm{m\,s^{-1}} + 0.04\,\mathrm{m\,s^{-1}} \cdot sin(t)$	$C_0 = 147\mu\mathrm{mol\,kg^{-1}}$
VAR 2	Eq. 3.4 + Eq. 3.7	$u_0 = 0.035\,\mathrm{m\,s^{-1}}$, $u_1 = 0.035\,\mathrm{m\,s^{-1}} + 0.025\,\mathrm{m\,s^{-1}} \cdot sin(t)$	$C_0 = 147\mu\mathrm{mol\,kg^{-1}}$
VAR 3	Eq. 3.4	$u_0 = 0.055\,\mathrm{m\,s^{-1}}$	$C_0 = 147\mu\mathrm{mol\,kg^{-1}} + 4\,\mu\mathrm{mol\,kg^{-1}} \cdot sin(t)$

may be due to the boundary condition of the conceptual model, which do not allow any flow through the eastern, northern and southern boundary. In reality and in TRATL01 the zonal currents are not limited by a box. For example the nSEC extends further east and can advect oxygen-poor water from east of 10°W towards the west which additionally acts to decrease oxygen concentrations in TRATL01. This mechanism is not captured by the conceptual model.

In the following we are going to discuss three time varying experiments VAR 1-3 performed with the conceptual model. The time variability is simulated by a simple sinusoid $A \cdot sin(t)$, where A is the amplitude and t is the time. The sinusoid in all experiments has a period of three years as this study focuses on the interannual variability of the NEUC.

VAR 1: Experiment VAR 1 is based on SIM 1 (Eq. 3.3 combined with flow field defined by Eq. 3.4, no recirculation) and simulates oxygen changes associated with a time varying mean flow. Here, we superimpose a sinusoid with $A = 0.04\,\mathrm{m\,s^{-1}}$ on the velocity amplitude of the background flow field ($u_0 = 0.055\,\mathrm{m\,s^{-1}} + 0.04\,\mathrm{m\,s^{-1}} \cdot sin(t)$ in Eq. 3.4, Fig. 3.11a).

VAR 2: To study oxygen changes associated with a time varying recirculation experiment VAR 2 is based on SIM 2 (Eq. 3.3 combined with flow field defind by Eq. 3.4+Eq. 3.7, recirculation included). Here, a sinusoid with $A = 0.025\,\mathrm{m\,s^{-1}}$ is superimposed on the veloxity amplitude of the recirculation ($u_1 = 0.035\,\mathrm{m\,s^{-1}} + 0.025\,\mathrm{m\,s^{-1}} \cdot sin(t)$ in Eq. 3.7, Fig. 3.11b).

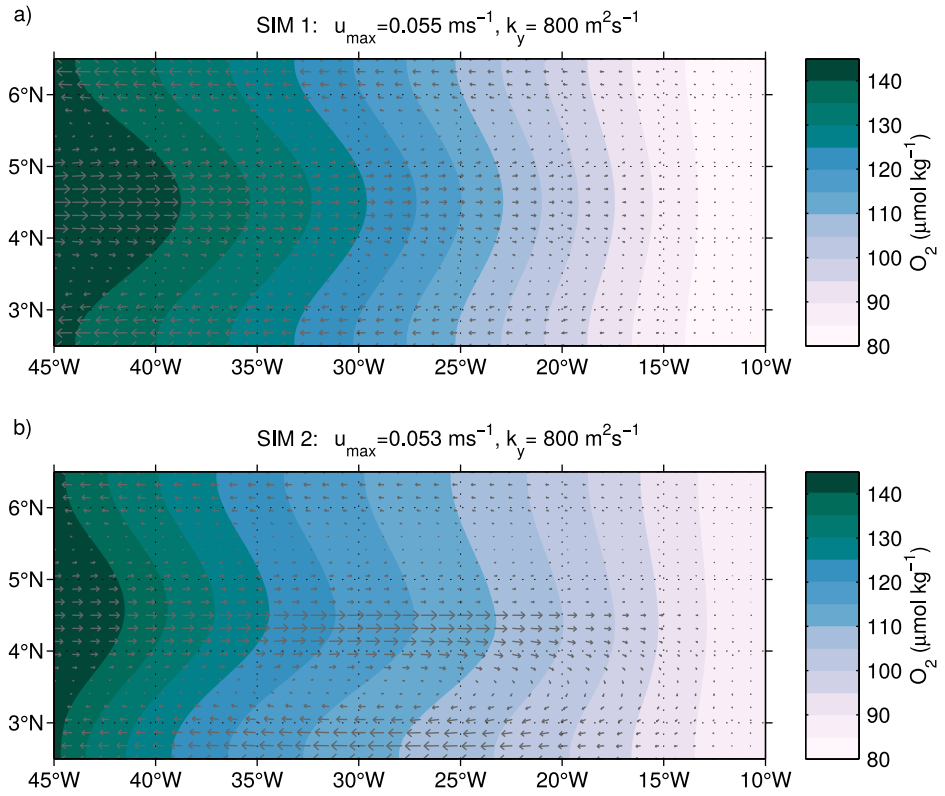

Figure 3.10: Oxygen distributions (shading and contours) as simulated from Eq. 3.3 with $k_x = k_y = 800\,\mathrm{m^2\,s^{-1}}$ using (a) the background flow field (Eq. 3.4) with $u_0 = 0.055\,\mathrm{m\,s^{-1}}$ and (b) an elliptical flow field (Eq. 3.7) superimposed on the background flow field with $u_0 = u_1 = 0.035\,\mathrm{m\,s^{-1}}$. The gray arrows show the velocity fields which have a comparable maximum velocity (u_{max}) in a) and b).

VAR 3: The last experiment VAR 3 is designed to study oxygen changes associated with time varying oxygen concentrations at the western boundary. VAR 3 is based on SIM 1 (Eq. 3.3 combined with flow field defined by Eq. 3.4, no recirculation). Here, a sinusoid with $A = 4\,\mu\mathrm{mol\,kg^{-1}}$ is superimposed on the oxygen source at the western boundary ($C_0 = 147\mu\mathrm{mol\,kg^{-1}} + 4\,\mu\mathrm{mol\,kg^{-1}} \cdot sin(t)$) while the velocity field is in steady state ($u_0 = 0.055\,\mathrm{m\,s^{-1}}$ in Eq. 3.4; Fig. 3.11c).

To analyze the results of the experiments VAR 1-3 we investigate the horizontal distribution and magnitude of the simulated oxygen amplitude (oxygen maximum minus oxygen minimum, Fig. 3.11d-f) during one period of variability (3 years). The oxygen amplitude shows where maximum variability occurs in the basin. Additionally we investigate the phase of the simulated oxygen maximum (Fig. 3.11g-i). This means we are calculating the time lag between the time of maximum amplitude of the forcing term (Fig. 3.11a-c) and the time of maximum simulated oxygen concentrations.

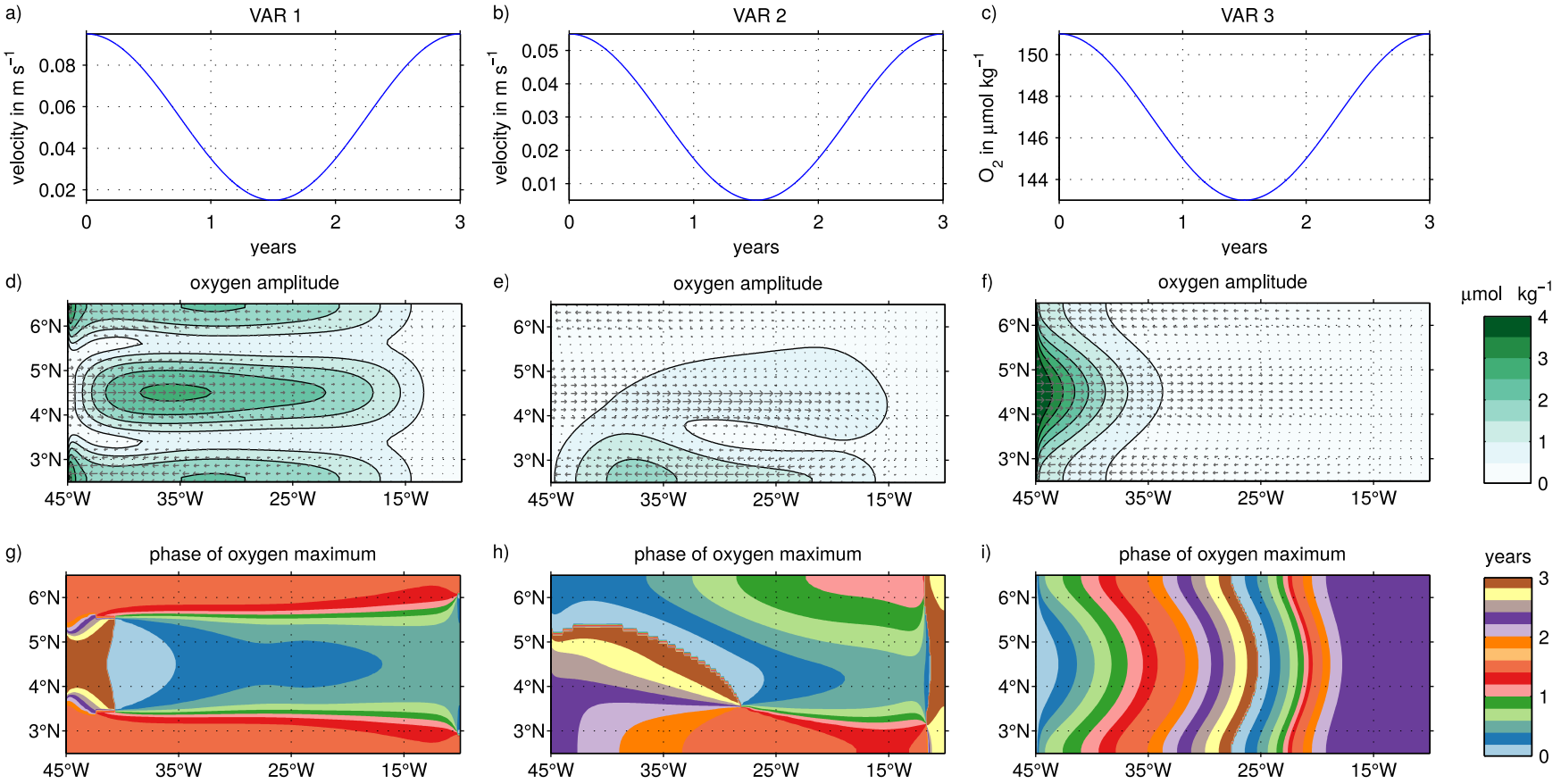

Figure 3.11: Amplitude of the time varying forcing (a,b,c), distribution of oxygen amplitude (shading in d,e,f) and distribution of phase of oxygen maximum (g,h,i) simulated with the idealized experiments: time varying background flow field (a,d,g), time varying recirculation (b,e,h) and time varying oxygen at 45°W (c,f,i). Gray arrows in d)-f) show the mean horizontal flow field.

In VAR 1 high oxygen amplitudes can be found across the whole basin (Fig. 3.11d). Along the eastward flow east of 40°W maximum oxygen concentration occur within the first 6 months after the velocity is maximum. This supports the suggestion of Brandt et al. (2010) derived for an intermediate jet that a strengthening of the NEUC supplied out of the well-ventilated western boundary region is associated with positive oxygen anomalies. Note that in VAR 1 the oxygen concentrations along the westward return flows become maximum about 1 to 1.5 years after maximum velocities occurs. This means that the oxygen amplitude in the cores of the eastward and the westward currents have a phase shift of 120°-180° depending on the longitude (180° near the western boundary, 120° near the eastern boundary). Consequently, while the oxygen concentrations are high within the NEUC, oxygen is low in the westward return flows and vice versa. In the eastern basin, the oxygen amplitude is weak (below $0.5\,\mu\mathrm{mol\,kg^{-1}}$). This is mainly due to the design of the flow field that has zero flow across the northern, southern and eastern boundary. In reality and in TRATL01, NEUC waters could exit the model domain toward all model boundaries as shown, e.g. in the model simulation of Hüttl-Kabus and Böning (2008).

Experiment VAR 2 can partly explain the results of TRATL01 (Fig. 3.8-3.9). The variable flow here mainly affects the oxygen concentrations of the southern westward return flow west of 25°W (Fig. 3.11e). There, maximum oxygen concentrations lag the maximum velocities by 1.5 to 2 years. In other words, within the first 6 months after the velocity amplitude is maximum oxygen concentrations become minimum in the southwestern quarter of the basin. Here, a stronger recirculation is associated with negative oxygen anomalies. However, east of 30°W along the eastward flow, weak positive oxygen anomalies ($< 1\,\mu\mathrm{mol\,kg^{-1}}$) occur. When increasing the velocity amplitude of the recirculation and its variability (e.g. $u_1 = 0.07\,\mathrm{m\,s^{-1}} + 0.04\,\mathrm{m\,s^{-1}} \cdot sin(t)$ in Eq. 3.7) in VAR 2, oxygen anomalies in the southwest of the basin become more negative and spread northward into the eastward flow during the first 1.5 year after maximum velocities occur (Fig. 3.S3). The higher the velocity amplitude of the recirculation and its variability, the higher the negative oxygen anomaly associated with maximum velocities in the southwest of the basin. Note that in VAR 1 oxygen values are minimum along the nSEC during maximum velocities. This suggests that in TRATL01 a combination of both processes, a stronger recirculation between NEUC and nSEC superimposed on a stronger mean flow, might occur. We test the effect of a variable mean flow field that is superimposed by a recirculation by modifying the experiment VAR 2 slightly. Instead of applying the sinusoid to the velocity amplitude of the recirculation in SIM 2 we apply it to the velocity amplitude of the mean flow field (Fig. 3.S4). Here, similar oxygen

pattern as in VAR 1 occur, but the highest variability is confined to the western basin as in VAR 2. In other words, a negative relationship between oxygen concentrations and NEUC strength is only caused by a variability of the recirculation between NEUC and nSEC as simulated in VAR 2 with a strong recirculation (Fig. 3.S3). This supports the hypothesis that in TRATL01 stronger (weaker) NEUC and nSEC transports are associated with a higher (lower) recirculation between the currents. A stronger (lower) recirculation is again associated with a stronger (weaker) supply of oxygen-poor water masses from the nSEC to the NEUC.

In VAR 3 the variability of oxygen concentrations at the western boundary shows a minor effect on the basin wide oxygen distribution (Fig. 3.11c,f,i). East of 37°W the oxygen amplitude drops below $1\,\mu\mathrm{mol\,kg^{-1}}$, and the weak oxygen maximum east of 30°W lags that at the western boundary by over 3 years (Fig. 3.11f,i). Note that the shading of the phase at about 30°W shows values close to zero, but as it is not plausible that the center of the basin is directly impacted by the western boundary, we interpret this as the color bar value plus one period of variability (3 years). Consequently, changes of oxygen concentrations about $4\,\mu\mathrm{mol\,kg^{-1}}$ in the source waters of the NEUC are too small to result in noticable signals in the oxygen concentration in the eastern basin on interannual time scales.

In summary the experiments with the conceptual model support our hypothesis that a strong mean recirculation between NEUC and nSEC in TRATL01 can lower the oxygen concentration within the simulated NEUC that, however, is stronger than in observations (SIM 2). Additionally we find maximum oxygen concentrations along the NEUC during maximum flow (VAR 1), which supports the results of Brandt et al. (2010) derived for an intermediate jet. However, in VAR 1 minimum oxygen concentration occur also along the nSEC during maximum velocities as in TRATL01. Furthermore, a strengthening of the recirculation (VAR 2) leads to negative oxygen anomalies especially in the western basin where the zonal oxygen gradient is high (Fig. 3.11d). This is consistent with the results of TRATL01. The last experiment VAR 3 shows that the effect of oxygen variability at the western boundary on the basin wide oxygen distribution is negligible on interannual time scales.

3.4 Discussion and Conclusion

In this study we analyze the interannual variability of the NEUC and, in a next step, its impact on oxygen in the ETNA in a state of the art OGCM. As the relationship between changes in current strength and oxygen differs from the one expected from

observations, this study further addresses the question which mechanisms might lead to these discrepancies. Our analysis is based on the output of the high-resolution OGCM TRATL01 (Duteil et al., 2014) in combination with an unique data set of 21 ship sections along 23°W and a conceptual model simulating an eastward current and its westward return flow with an oxygen source at the western boundary (Brandt et al., 2010).

In observations and in TRATL01, the NEUC is associated with a local oxygen maximum. Although the NEUC in TRATL01 is much stronger than in observations its associated oxygen maximum is much weaker (Fig. 3.2). The correct representation of oxygen concentrations and their variability in the eastern tropical oceans still proves a challenge for current generation ocean and climate models (e.g. Oschlies et al., 2018; Cabré et al., 2015; Oschlies et al., 2017). This study suggests that a stronger than observed recirculation between the NEUC and the nSEC in TRATL01 contributes to the model bias in the NEUC region. The experiment SIM 2 performed with the conceptual model supports this hypothesis. In SIM 2 a recirculation between the NEUC and nSEC is superimposed on the background flow field. The results generally show a stronger eastward flow and lower oxygen concentrations west of 20°W.

Despite our large data set of 21 ship sections, the observations are still too sparse to detect a seasonal signal or long-term variability of the NEUC. The NEUC is a weak current and in ship sections it is likely obscured by mesoscale activity (e.g. Weisberg and Weingartner, 1988) and interannual variability (Hüttl-Kabus and Böning, 2008; Goes et al., 2013) present in the tropical Atlantic .

TRATL01 simulates a seasonal to interannual variability of the NEUC which agrees in general with previous studies (Hüttl-Kabus and Böning, 2008; Goes et al., 2013) although the mean NEUC transport in TRATL01 is stronger compared to most observations (e.g. Bourlès et al., 1999a, 2002; Schott et al., 2003; Brandt et al., 2006; Urbano et al., 2008). The interannual variability of the NEUC in TRATL01 is linked to the AMM (Fig. 3.6). We find an anticorrlation between the NEUC and the AMM index which is in good agreement with Goes et al. (2013). Our results suggest that the anomalous wind pattern associated with the AMM can hamper or amplify the seasonal cycle of the NEUC. Different mechanisms can potentially impact the NEUC transport. Previous studies suggest that the NEUC might be pulled by the upwelling in the Guinea Dome and along the northwest African coast (McCreary et al., 2002; Furue et al., 2007, 2009). In this study we find that the NEUC strength is related to the anomalous wind stress curl above the ETNA (Fig. 3.5). This wind stress curl anomaly impacts the seasonal shoaling of isopycnals in the eastern equatorial basin (Foltz and McPhaden,

2010a; Burmeister et al., 2016) which again might impact the seasonal cycle of the NEUC. Additionally there might be direct wind curl driven recirculations as suggested by the Sverdrup stream function (contours in 3.5b). Furthermore a composite analysis of wind stress suggests enhanced (reduced) coastal upwelling by along-shore winds off Northwest Africa during a strong (weak) NEUC, which would support that the NEUC is additionally pulled by coastal upwelling (Fig. 3.6). Another process that might impact the NEUC strength is the Eliassen-Palm flux of TIWs (Jochum and Malanotte-Rizzoli, 2004). Perez et al. (2012) found that years of high (low) TIW activity are associated with a strong (weak) wind stress curl along 5°N. We find a strong (weak) wind stress curl during years of strong (weak) NEUC flow. This indicates that anomalous TIW activity might also contribute to interannual NEUC variability.

In contrast to our expectations that a stronger NEUC flow is associated with positive oxygen anomalies along its pathway, we find an inverse relationship of both quantities on interannual time scales in TRATL01 (Fig. 3.8 and 3.9). Again, a too strong recirculation between the NEUC and the nSEC in TRATL01 can explain the reverse relationship between oxygen and NEUC transports. A stronger recirculation supplies more oxygen-poor water masses from the nSEC into the NEUC. The NEUC in turn transports less oxygen even though it is stronger. In TRATL01 the interannual variability of respiration is too small to have an effect on oxygen, which is consistent with previous studies (Montes et al., 2014; Vergara et al., 2016; Pozo Buil and Di Lorenzo, 2017; Yang et al., 2017). The large-scale wind pattern associated with the AMM effects not only the NEUC but also the general wind-driven circulation in the tropical Atlantic (Fig. 3.5). Consequently, we find basin wide oxygen anomalies apart from those associated with the NEUC variability (Fig. 3.8).

We performed three further experiments (VAR 1-3) with the conceptual model to investigate oxygen changes associated with a time varying mean flow (VAR 1), a time varying recirculation (VAR 2) or a time varying oxygen source at the western boundary (VAR 3). In VAR 1 maximum eastward velocities are associated with maximum oxygen concentrations and maximum westward velocities with minimum oxygen concentrations. The highest oxygen variability occurs along the cores of the eastward and westward currents. In VAR 2 highest oxygen variability occurs in the western basin where the oxygen gradient is strongest. This supports our hypothesis that enhanced recirculation between the NEUC and nSEC results in an anticorrelation between NEUC strength and oxygen within the NEUC in TRATL01. The results of VAR 3 suggest that the effect of interannual oxygen variability at the western boundary is of minor importance for the basin wide oxygen distribution (Fig. 3.11).

The combined results of our analysis allow us to draw the following conclusions: The impact of NEUC interannual variability on the oxygen distribution in the tropical North Atlantic depends on the processes dominating the variability. If a strengthening of the NEUC is associated with a higher ventilation from the western boundary it will advect more oxygen-rich waters towards the eastern basin. If a strengthening of the NEUC is associated with a stronger recirculation between the NEUC and the nSEC, for example due to higher TIW activity or directly wind-driven, it is advecting less oxygen towards the east. If both processes occur simultaneously, the recirculation will act to damp the effect on oxygen of a stronger NEUC mean flow supplied out of the western boundary current.

A general issue emphasized in this study is the connection of the zonal current system in the tropical North Atlantic to the western boundary. This becomes important especially when investigating tracer distributions. While observational studies suggest that the eastward currents in the tropical Atlantic are important supply routes for oxygen towards the east (e.g. Stramma et al., 2008a; Brandt et al., 2010, 2015; Fischer et al., 2008), model studies point to the importance of recirculations between the off-equatorial zonal currents and the EUC (Jochum and Malanotte-Rizzoli, 2004; Hüttl-Kabus and Böning, 2008). For example in observations, the lower part of the SEUC seems to be supplied out of the western boundary (Fischer et al., 2008) but models seem not to be able to simulate this connection (Jochum and Malanotte-Rizzoli, 2004; Hüttl-Kabus and Böning, 2008). It is hence important to improve the understanding of the connection of the zonal current system with the well-ventilated western boundary region in the tropical Atlantic in both, observations and models.

Realistically simulating the narrow-banded zonal current system of the tropical Atlantic still proves a challenge to ocean models. A promising approach to improve its representation in OGCMs is to increase the horizontal and temporal resolution of the wind forcing as done in the new JRA55-do surface dataset (Tsujino et al., 2018). Our results show a relationship between the interannual NEUC and wind stress curl variability in TRATL01 (Fig. 3.5) which suggests that the wind forcing plays an important role. A too coarse resolution of the wind forcing might not resolve important wind stress curl patterns which could lead to an erroneous representation of the zonal current system. Improving the representation of the zonal current system in the tropical oceans in coupled physical and biogeochemical model simulations is crucial to simulate more realistically the mean state and the variability of the oxygen distribution and the oxygen minimum zones.

Acknowledgments

This study was funded by the Deutsche Forschungsgemeinschaft as part of the Sonderforschungsbereich 754 "Climate–Biogeochemistry Interactions in the Tropical Ocean", through several research cruises with RV L'Atalante, RV Maria S. Merian, RV Meteor and RV Polarstern, by the project FOR1740 and by the Deutsche Bundesministerium für Bildung und Forschung (BMBF) as part of projects NORDATLANTIK (03F0605B, 03F0443B) and RACE (03F0651B). We thank the captains, crews, scientists and technical groups involved in the different national and international research cruises to the eastern tropical North Atlantic that contributed to collecting CTD, velocity (and mooring data) and making them freely available. We thank Johannes Hahn and Rebecca Hummels for post-processing of the recent ship section data. The shipboard data is accessible at https://doi.pangaea.de/10.1594/PANGAEA.899052. We thank Sunke Schmidtko, Gregory C. Johnson, John M. Lyman for creating the MIMOC climatology and making it freely available at http://www.pmel.noaa.gov/mimoc/. The model ouput of TRATL01 was published in Duteil et al. (GRL, 2014, doi: 10.1002/2013GL058888) and is available on https://data.geomar.de.

3.5 Supporting Information for "Variability of the Atlantic North Equatorial Undercurrent and its impact on oxygen"

Contents of this file

1. Figures 3.S1 to 3.S4

Introduction

The supplementary information contains four figures (Fig. 3.S1-3.S4). These figures are realized using simulation SIM1 and SIM2 of the conceptual model, ship observations along 23°W, the MIMOC climatology (Schmidtko et al., 2017), and HadISST data (retrieved from https://climatedataguide.ucar.edu/climate-data/sst-data-hadisst-v11).

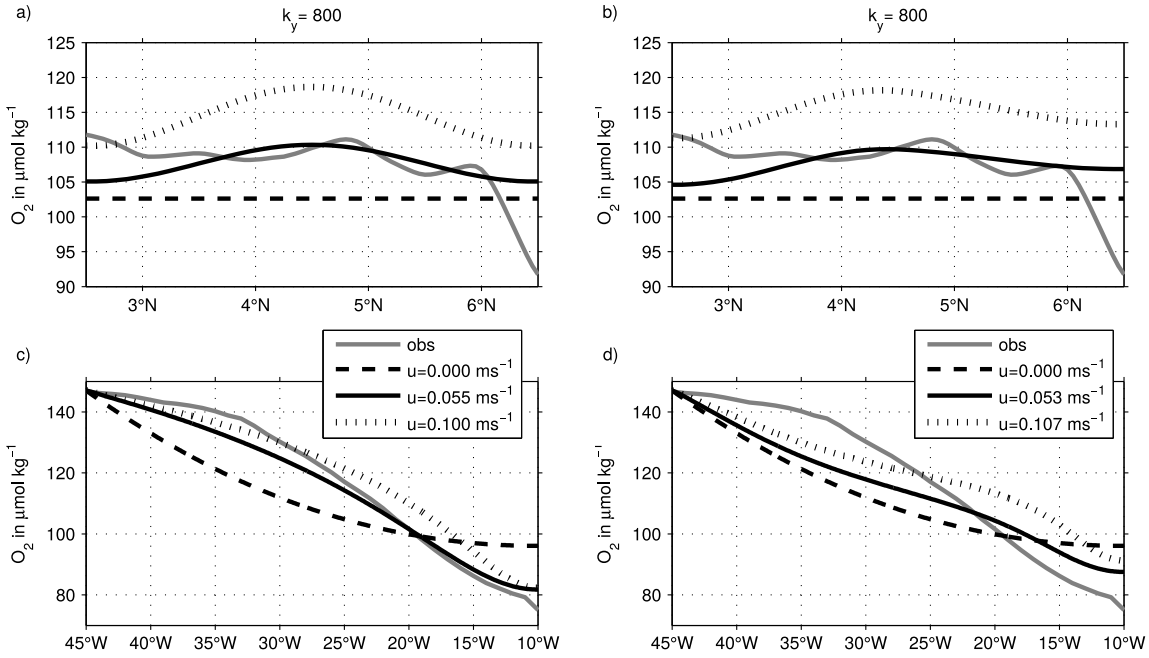

Figure 3.S1: Black lines show (a,b) the meridional and (c,d) the zonal oxygen distribution along 23°W and 4.5°N, respectively, as simulated from Equ. 3 with $k_x = k_y = 800\,\mathrm{m^2\,s^{-1}}$ and three different u (velocity maximum) using (a,c) only the background flow field (Eq. 4, where $u_0 = 0\,\mathrm{m\,s^{-1}}$, $0.055\,\mathrm{m\,s^{-1}}$, and $0.1\,\mathrm{m\,s^{-1}}$ for the dashed, solid, and dotted line, respectively) and (b,d) superimpose a recirculation on the background flow field (Eq. 4+7, where $u_0 = u_1 = 0\,\mathrm{m\,s^{-1}}$, $0.035\,\mathrm{m\,s^{-1}}$, and $0.14\,\mathrm{m\,s^{-1}}$ for the dashed, solid, and dotted line, respectively). The observations (gray lines) are oxygen concentrations along the $26.5\,\mathrm{kg\,m^{-3}}$ isopycnal from (a,b) the mean ship section along 23°W and (c,d) the MIMOC climatology (Schmidtko et al., 2017).

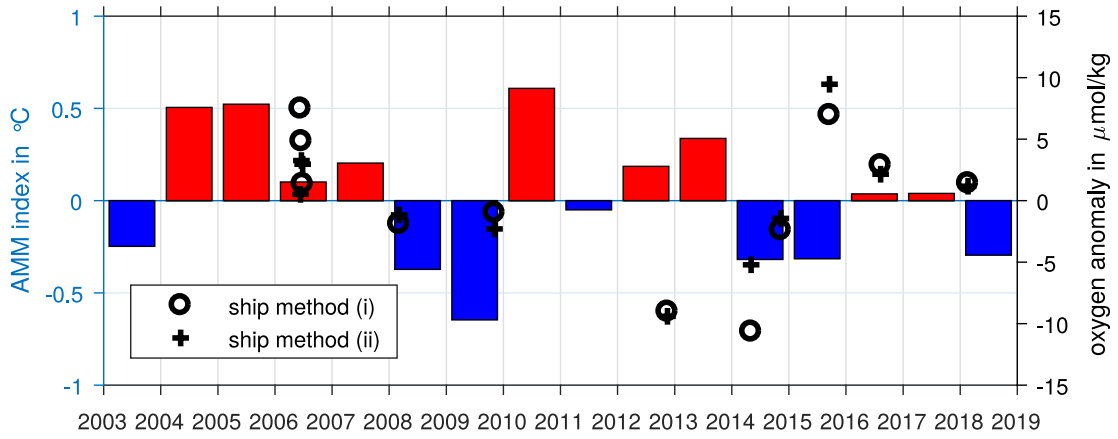

Figure 3.S2: Left y-axis shows the monthly mean AMM index after Servain (1991) derived from HadISST data (red and blue bars, retrieved from https://climatedataguide.ucar.edu/climate-data/sst-data-hadisst-v11). Right y-axis shows oxygen anomalies derived from ship sections (total mean is substracted) averaged in NEUC region using 2 methods. (i) The values are average in a meridionally varying frame (100-300 m depth, $(Y_{CM}-1.5)°$ - $(Y_{CM}+1)$°N) (crosses). (ii) The values are averaged in a fixed box (100-300 m depth, 3°-6.5°N) (circles).

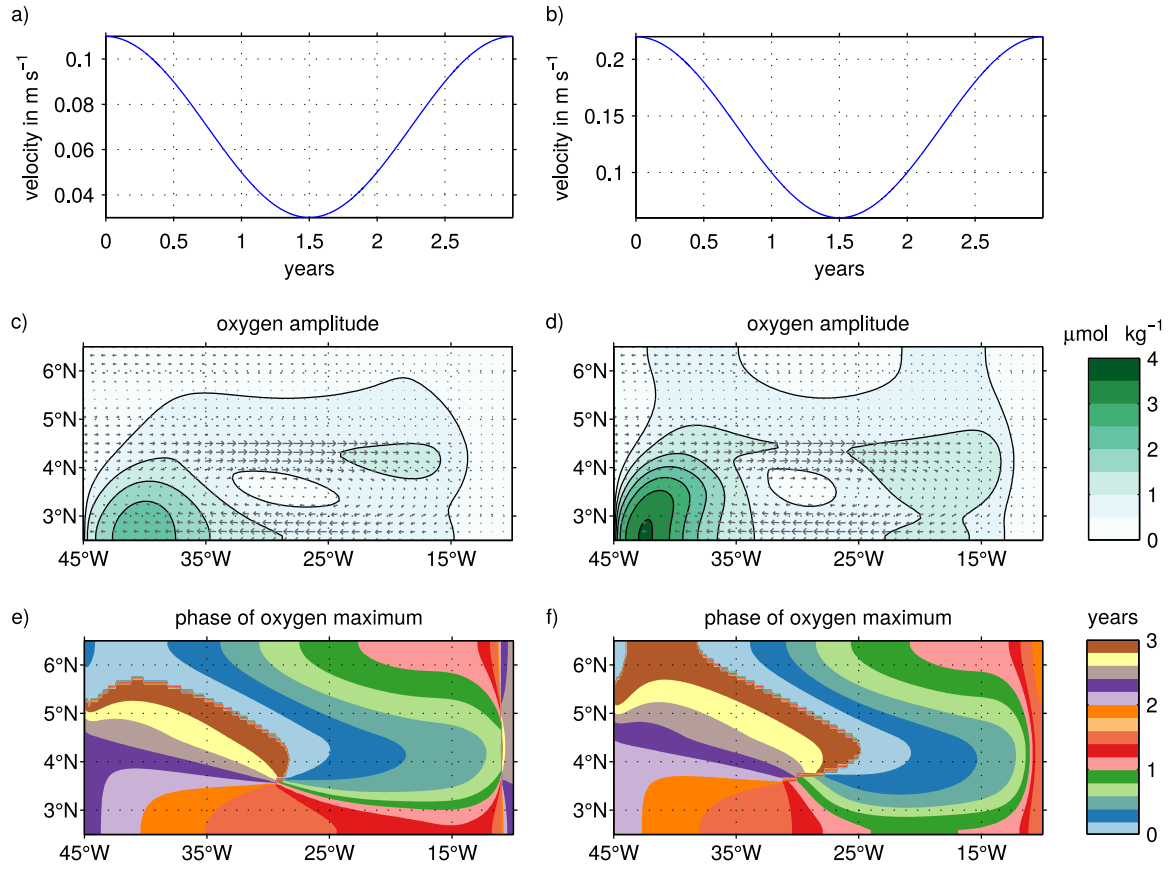

Figure 3.S3: Amplitude of the time varying forcing (a,b), distribution of oxygen amplitude (shading in c,d) and distribution of phase of oxygen maximum (e,f) simulated by two experiments with the conceptual model (Eq. 3). Gray arrows in c-d) show the mean horizontal flow field. Both experiments study oxygen changes associated with a steady mean flow that is superimposed by a temporally varying recirculation. They are based on SIM 2. The following velocity amplitudes are used for a,c,e: the velocity amplitude of the steady mean field (Eq. 4) is $u_0 = 0.035\,\mathrm{m\,s^{-1}}$, the velocity amplitude of the time varying recirculation (Eq. 7) is $u_1 = 0.07\,\mathrm{m\,s^{-1}} + 0.04\,\mathrm{m\,s^{-1}} \cdot sin(t)$. The following velocity amplitudes are used for b,d,f: the velocity amplitude of the steady mean field (Eq. 4) is $u_0 = 0.035\,\mathrm{m\,s^{-1}}$, the velocity amplitude of the time varying recirculation (Eq. 7) is $u_1 = 0.14\,\mathrm{m\,s^{-1}} + 0.08\,\mathrm{m\,s^{-1}} \cdot sin(t)$.

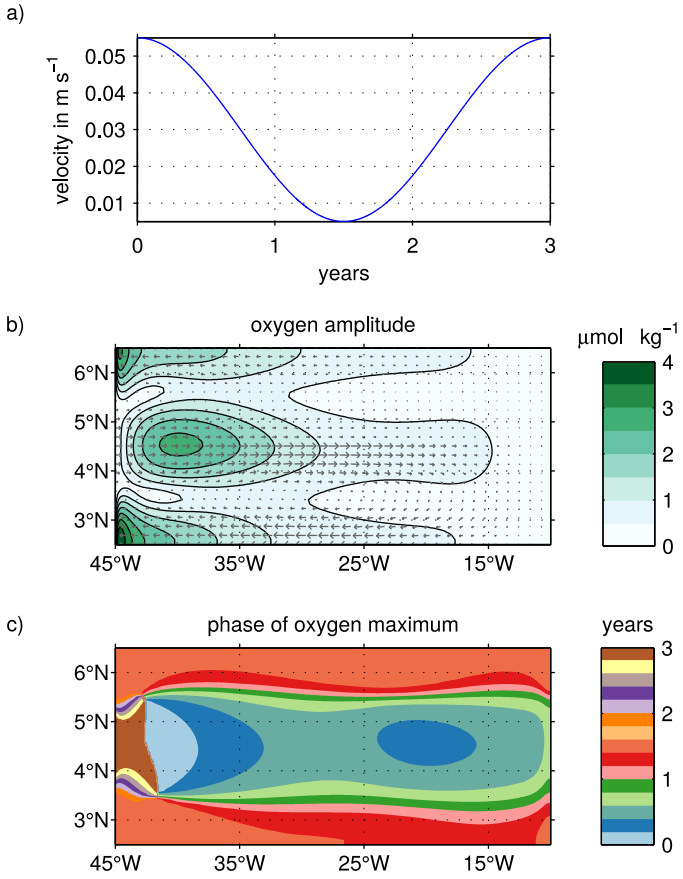

Figure 3.S4: Amplitude of the time varying forcing (a), distribution of oxygen amplitude (shading in b) and distribution of phase of oxygen maximum (c) simulated with the conceptual model: This experiment studies oxygen changes associated with a time varying mean flow that is superimposed by a temporally constant recirculation. It is based on SIM 2. Here, a sinusoid with $A = 0.025\,\mathrm{m\,s^{-1}}$ is superimposed on u_1 of the background flow field (Eq. 7, Fig. 11b). Gray arrows in b) show the mean horizontal flow field.

4 Reconstructed NEUC transports from moored observations at 5°N, 23°W and its relation to oxygen

Here, the NEUC variability and its relation to oxygen is explored based on direct velocity and oxygen observations at 5°N, 23°W. The NEUC transport is reconstructed from moored and shipboard velocity observations for the periods Jun 2008 to February 2008 and November 2009 to January 2018. In contrast to the model study in the previous chapter, neither the moored zonal velocities at 5°N nor the reconstructed NEUC transport time series exhibit a strong seasonal cycle. The NEUC transport variability is instead dominated by sporadic intraseasonal eastward events. In agreement with the results of the previous study, the relation between NEUC strength and oxygen levels within the NEUC is not straight forward. The intraseasonal events are only occasionally associated with positive oxygen anomalies. Nevertheless, they are found to be responsible for the local oxygen maximum in the mean shipboard section along 23°W at the NEUC core position.

The manuscript will be submitted to *Geophysical Research Letters* for publication.

Citation: **Burmeister K.**, Lübbecke, J. F., Brandt, P., Claus, M., & Hahn, J. (2019). Ventilation of the eastern tropical North Atlantic by intraseasonal flow events of the North Equatorial Undercurrent. *To be submitted to* Geophysical Research Letters.

Section 4.1 to 4.8: The candidate carried out the analysis of observational data sets. She produced all figures and authored the manuscript from the first draft to the final version.

Section 4.9: The shallow water model simulations were carried out by Martin Claus. The candidate estimated the scaling coefficients for the shallow water model, applied them to the model output and carried out the analysis of the scaled model output. She produced all figures and authored the manuscript from the first to the final version.

Abstract

Although the core velocity of the Atlantic North Equatorial Undercurrent (NEUC) is low ($0.1\,\mathrm{m\,s^{-1}}$ to $0.3\,\mathrm{m\,s^{-1}}$) it has been suggested to act as an important oxygen supply route towards the oxygen minimum zone in the eastern tropical North Atlantic. For the first time the intraseasonal to interannual NEUC variability and its impact on oxygen is investigated based on shipboard and moored velocity observation around 5°N, 23°W. In contrast to previous studies that were mainly based on models or hydrographic data, we find hardly any seasonal cycle of NEUC transports in the central Atlantic. The NEUC transport variability is instead dominated by sporadic intraseasonal events. Only some of these events are associated with high oxygen levels suggesting an occasional eastward oxygen supply by NEUC transport events. Nevertheless, they are found to be responsible for the local oxygen maximum in the mean shipboard section along 23°W at the NEUC core position.

Plain Language Summary

In the eastern tropical North Atlantic a zone of low-oxygen waters exists between 100 m and 700 m depth due to high oxygen consumption and a weak exchange of water masses. Long-term oxygen changes in this zone have been reported with possible impacts on, for example, the ecosystem or the available habitat for fish. Typically, the water masses in that region are exchanged via weak eastward and westward currents. As the oxygen concentration in the western Atlantic basin is high, an eastward current such as the North Equatorial Undercurrent (NEUC) may transport oxygen-rich waters into the eastern low-oxygen zone. Given the east-west difference in oxygen concentration, we assume that a stronger NEUC is transporting more oxygen-rich water from the western towards the eastern basin. This is the first study that investigates the variations in NEUC transport based on direct velocity measurements. In contrast to previous studies based on model simulations or hydrographic data, we do not find a seasonal cycle of the NEUC transport. We find that changes of the NEUC transport are dominated by bursts of eastward flow which persist for about two months. These eastward flow bursts are only occasionally associated with higher oxygen concentrations.

4.1 Introduction

The circulation of the upper tropical Atlantic is characterized by a complex current system which takes part in the wind-driven equatorial gyre circulation, the shallow subtropical and tropical overturning cells and the basin-wide Atlantic meridional overturning circulation (e.g. Schott et al., 2004; Hazeleger and Drijfhout, 2006). The zonal currents play a key role in the basin wide distribution of water mass properties and affect the transport of heat, salt and biogeochemical components such as oxygen (e.g. Schott et al., 2004; Hazeleger and Drijfhout, 2006; Oschlies et al., 2018). The NEUC is an eastward flowing subsurface (here defined in the depth range 65-270 m) current centered at 5°N. Although the NEUC core velocity ($0.1\,\mathrm{m\,s^{-1}}$ to $0.3\,\mathrm{m\,s^{-1}}$) is one of the lowest among the wind-driven off-equatorial currents in the tropical Atlantic the NEUC has been suggested to act as an important oxygen supply route towards the oxygen minimum zone in the ETNA (Stramma et al., 2008a; Brandt et al., 2010; Hahn et al., 2017).

Model studies generally agree that the NEUC is mainly in geostrophic balance but its driving mechanism is under discussion. Potential mechanisms that were described for the NEUC or similar subsurface currents in other tropical basins are the conservation of angular momentum of the tropical overturning cells (Marin et al., 2000), the Eliassen-Palm flux associated with the propagation of Tropical Instability Waves (TIWs) (Jochum and Malanotte-Rizzoli, 2004) or the pull of the upwelling within domes in the eastern basin or at the eastern boundary (McCreary et al., 2002; Furue et al., 2007, 2009).

Until now, the seasonal to long-term variability of the NEUC has been investigated based on model output (Hüttl-Kabus and Böning, 2008; Burmeister et al., 2019) or geostrophic velocities derived from a combination of hydrography and satellite data (Goes et al., 2013). In these studies, a seasonal cylce of the NEUC with amplitudes of 1 Sv to 3.5 Sv was identified. In general, NEUC transport estimates derived from meridional ship sections are obscured by mesoscale activity (Weisberg and Weingartner, 1988) and interannual variability (Hüttl-Kabus and Böning, 2008). Consequently, studies based on shipboard velocity observations have not yet been able to detect a seasonal cycle of the NEUC (Schott et al., 1995; Bourlès et al., 1999a, 2002; Schott et al., 2003; Urbano et al., 2008; Burmeister et al., 2019).

For the first time, we will investigate the NEUC variability using direct velocity observations. In this study we reconstruct the eastward transport associated with the NEUC at 5°N, 23°W using moored velocity observation from July 2006 to February

2018 in combination with 24 meridional ship sections taken between 21°W and 26°W. This study aims to investigate the intraseasonal to interannual variability of the NEUC and its impact on oxygen levels.

4.2 Data

Moored ADCP velocity, hydrography and oxygen data are available at 5°N, 23°W (Jun 2006-Feb 2008, Nov 2009-Jan 2018) as well as at 4.6°N, 22.4°W and 4.5°N, 23.4°W (Nov. 2012-Apr. 2014). The upper limit of the ADCP observations varies between 65 m and 85 m, the lower limit is at least 755 m. Oxygen and Conductivity-Temperature-Depth (CTD) sensors were installed at the mooring at 5°N, 23°W in 100 m, 200 m, and 300 m depth. All instruments were set to a sampling rate of 2 h or higher. The moored velocity data was linearly interpolated onto a regular time-depth grid (12 h $\times$10 m) and a 40-day low-pass Butterworth filter was applied to remove tides from the time series. Hydrography and oxygen data from point measurements were interpolated onto a 12-h time grid. This data set is an extension of the one used in Hahn et al. (2014, see Text S1 details).

In addition to the mooring time series we use data from 24 meridional ship sections taken between 21°W and 26°W which were obtained in the time period 2002 to 2018 (Table 3.S1). Only shipboard ADCP, hydrography and oxygen sections that cover at least the upper 350 m between 0° and 10°N are used. The ship sections are an extension of the data set used in Burmeister et al. (2019, see Text S1 for more details).

4.3 Observed velocity variability at 5°N, 23°W

In the upper 300 m the horizontal velocity field from the moored ADCPs at 5°N, 23°W is characterized by a weak mean eastward velocity with maximum velocity of 9 cm s^{-1} at the upper limit of the ADCP range (65m) and a meridional velocity varying around zero (Fig. 4.1 a and b). The periodograms of the horizontal velocity components indicate variability over a range of frequencies, in particular in the intraseasonal band (Fig. 4.1 c and d). While the zonal velocity exhibits intraseasonal variability mainly for periods greater than 70 days, the meridional velocity is dominated by variability with periods between 30 and 70 days which is associated with TIWs (Jochum and Malanotte-Rizzoli, 2003). The zonal velocity, while eastward in the mean, occasionally changes to westward. Its variability is characterized by strong eastward events with a duration of about two months occurring throughout the year. Unexpectedly, the seasonal cycle

of the zonal velocity is much weaker than found in previous studies (Hüttl-Kabus and Böning, 2008; Goes et al., 2013; Burmeister et al., 2019). The annual harmonic fit with a maximum amplitude of 3 $cm\,s^{-1}$ only explains between 2% (85 m) and 9% (300 m) of the zonal velocity variability. For the semi-annual harmonic we derived a maximum amplitude of 5 $cm\,s^{-1}$ and an explained variance between 1% (300 m) and 11% (75 m).

4.4 NEUC transport estimates at 23°W

The NEUC transport is estimated by four different methods. (i) We calculated the NEUC transport (only eastward velocities) between the 24.5 $kg\,m^{-3}$ and 26.9 $kg\,m^{-3}$ neutral density surfaces from the 24 ship sections using a path following algorithm developed by Hsin and Qiu (2012) (Fig. 4.2, green diamonds). This method allows to follow the current core, thereby avoiding artifacts if the current is meridionally migrating (see Text S2 for more details). Using this method we estimate a mean NEUC transport of 2.7±0.4 Sv. Uncertainties are given in terms of the standard error. In the following, we consider this estimate as a reference NEUC transport keeping in mind that the NEUC transport estimate from ship sections can be obscured by mesoscale activity (Weisberg and Weingartner, 1988) and interannual variability (Hüttl-Kabus and Böning, 2008).

(ii) We integrate the zonal velocity sections (only eastward velocities) between 4.25°N and 5.25°N, 65 m and 270 m (Fig. 4.2, black circles). This box is chosen to be consistent with the transports calculated from the moored observations described below. The mean box integrated transport derived from the ship sections is 1.4±0.2 Sv. As the chosen box does not cover the complete NEUC region, we are underestimating the NEUC transport using the box integrated method. However, method (ii) represents the variability of the reference NEUC well (R=0.91, Fig. 4.S2a)

(iii) We reconstruct the NEUC transport combining the moored velocity observations at 5°N, 23°W as well as 4.6°N, 22.4°W and 4.5°N, 23.4°W and the ship sections following the optimal width (OW) method described in Brandt et al. (2014). This method aims to find an optimal latitude range W_i for each mooring position i to reconstruct the latitudinally integrated zonal velocity $U(z,t)$ by:

$$U(z,t) = \sum_{i=1}^{3} W_i u_i(z,t) \tag{4.1}$$

Therefor, we latitudinally integrate the eastward velocities of each ship section from 4.25°N to 5.25°N. The latitudinally integrated velocity is then regressed onto the zonal velocities of the ship section at the three mooring position between 65 m and 270 m depth

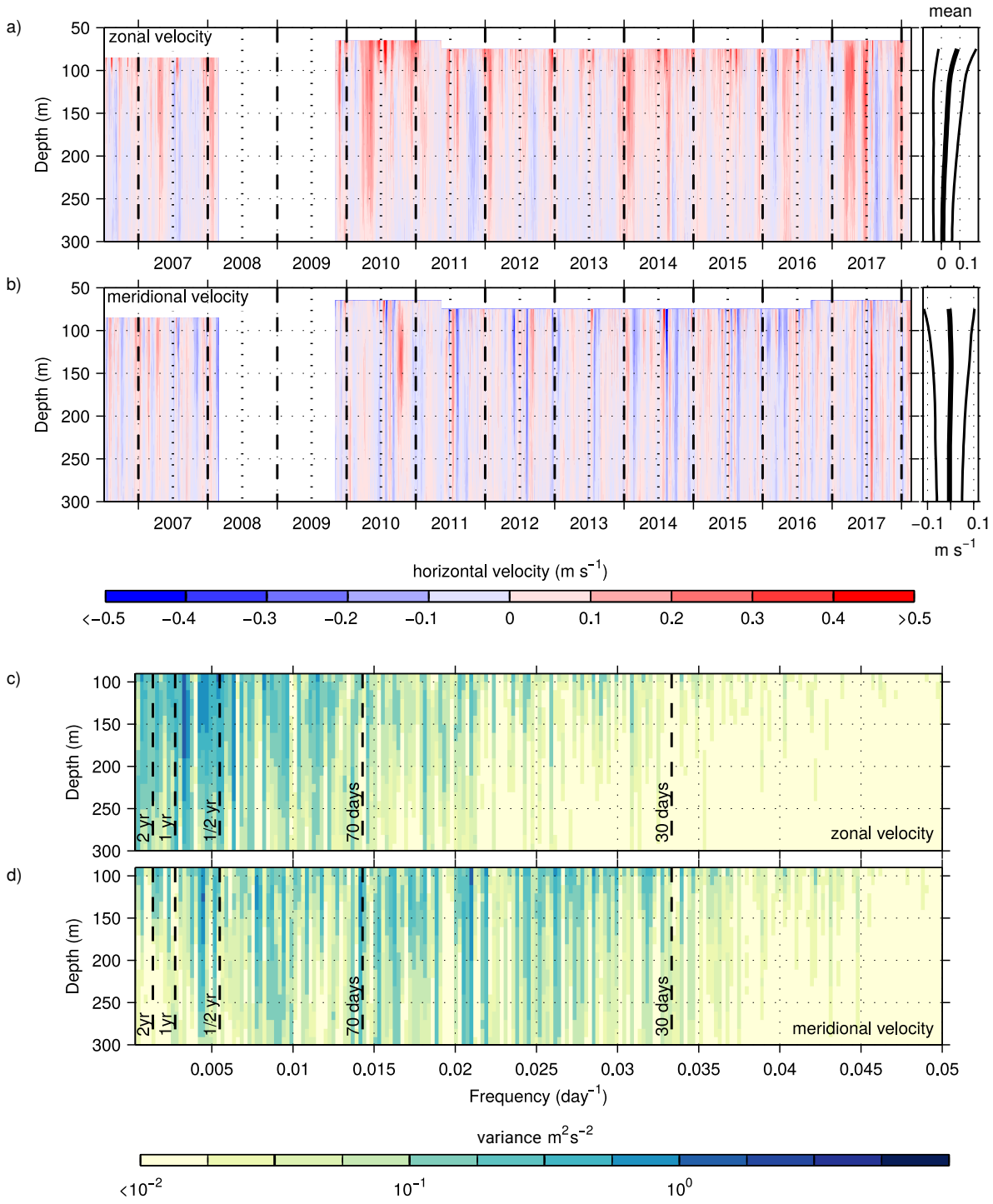

Figure 4.1: (a) Zonal and (b) meridional velocity measurements from moored ADCPs at 5°N, 23°W. The temporal mean profiles (thick black line) are shown at the right side of the zonal (a) and meridional (b) velocity time series. The thin black line marks the mean profile ± its standard deviation. Lomb-Scargle periodogram of (c) zonal and (d) meridional velocity.

to obtain W_i. We estimated that the moorings at 5°N, 4.6°N and 4.5°N correspond to latitude ranges of 0.46°, 0.18° and 0.37°, respectively. As the two southern moorings are very close together, the width of the two moorings is overweighted and the sum of the three widths is slightly bigger than the whole domain. The NEUC transport is then reconstructed by integrating Equation 4.1 over the same depth range as for method (ii) (Fig. 4.2 blue line). Note that data from all three mooring positions are only available for the time period November 2012 to April 2014. The root mean square error of the reconstructed transports using method (iii) and the box intergrated transport (method ii) using the shipboard data is 0.16 Sv. The mean reconstructed transport is 0.9±0.3 Sv. For a validation of the method see Text S2 in the supplementary information.

(iv) This method is similar to method (iii) but only using moored velocity observations at 5°N, 23°W to obtain a longer transport time series (Fig. 4.2 grey line). Here, the 5°N mooring corresponds to a latitude range of 0.88°. Although the root mean square error between the reconstructed transport and the box integrated transport increases (0.51 Sv) when using only one mooring, the reconstructed transports based on one mooring agrees well with the one reconstructed using three moorings (R=0.89). The mean NEUC transport is the same as estimated for method (iii), i.e. 0.9±0.2 Sv.

In the following we will analyze the NEUC variability based on the reconstructed time series using only the mooring at 5°N, 23°W. Please note that at 23°W the NEUC is approximately located between the 24.5 $\mathrm{kg\,m^{-3}}$ and 26.9 $\mathrm{kg\,m^{-3}}$ neutral density surfaces which corresponds to a depth range of about 65 m and 270 m. The upper limit of the ADCP measurements varies between 65 m and 85 m, hence the upper part of the NEUC is not always fully covered by the moored observations. Additionally, the chosen width of the integration box may not always cover the complete meridional extent of the NEUC (Fig. 4.S1a). Consequently, the reconstructed transport time series from the moored velocity observations tends to underestimate the mean current strength of the NEUC. Nevertheless, we still consider the variability to be captured to a large extend. This is supported by transport estimates reconstructed using all three moorings combined with zonal velocity sections between 3.5°N and 6.0°N which agree reasonably well with the transport time series reconstructed by method (iii) accounting for velocities between 4.25°N and 5.25°N (Fig. 4.S4).

4.5 NEUC variability

Similar to the zonal velocity time series, the NEUC is dominated by strong eastwards transport events that persist for about two months. The transport time series do not

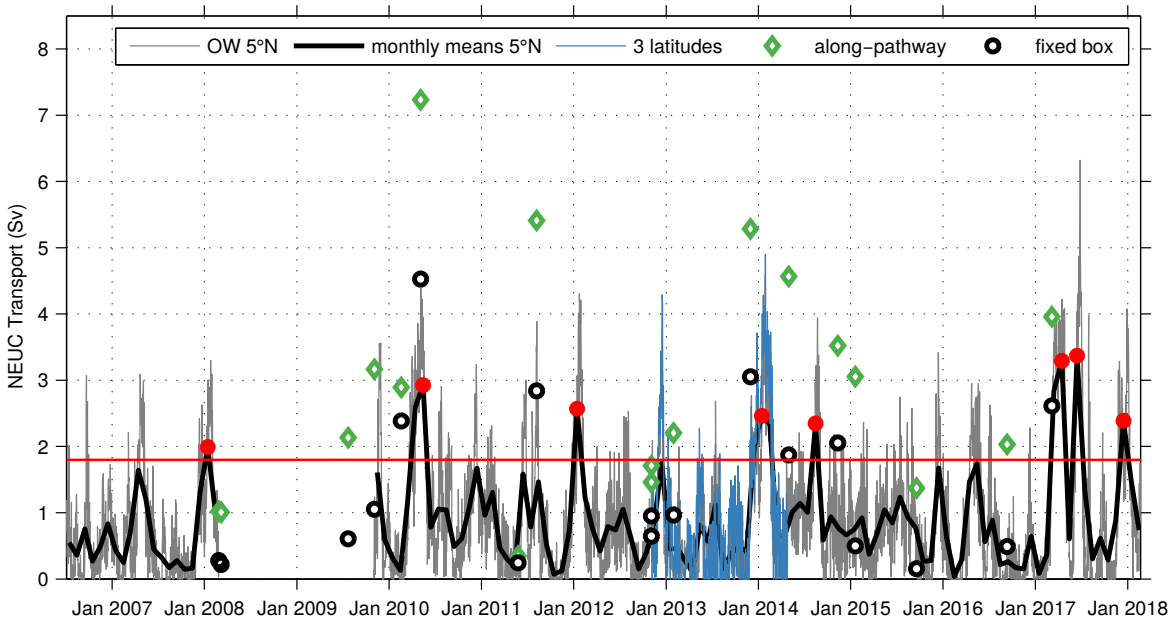

Figure 4.2: NEUC transport at 23°W calculated by four different methods: (i) from ship observations using a path following algorithm (green diamonds); (ii) from ship sections by integrating the eastward velocities in a fixed box (black circles); (iii) by the OW method combining ship sections and moored zonal velocities at three mooring positions (blue line); (iv) by the OW method combining ship sections with moored zonal velocities at 5°, 23°W (gray line). The black thick line shows the monthly mean values of the NEUC transport reconstructed at 5°N. The red line marks 2.5 times the standard deviation of the monthly mean transports used to define strong transport events (red dots).

exhibit a seasonal cycle. The explained variance of the annual and semi-annual harmonic is only 2% and 3%, respectively. We therefore focus the analysis on the strong intraseasonal events. We find 14 events that exceed 2 times the standard deviations of the complete monthly mean time series. Eight of these events exceed 2.5 times the standard deviation, which we refer to as strong eastwards transport events. In the monthly mean time series the strong eastward events have a maximum transport between 2.3 Sv and 3.8 Sv and peak without a clear seasonal preference (3 in January, 1 each in April, May, June, August and December). The events last between two to five months (from local minimum to minimum). During the strong eastward events the 12-hourly transports reach maximum values from 3.8 Sv to 7.2 Sv. How these intraseasonal transport events contribute to the ventilation of water masses at 5°N, 23°W is investigated in the following section.

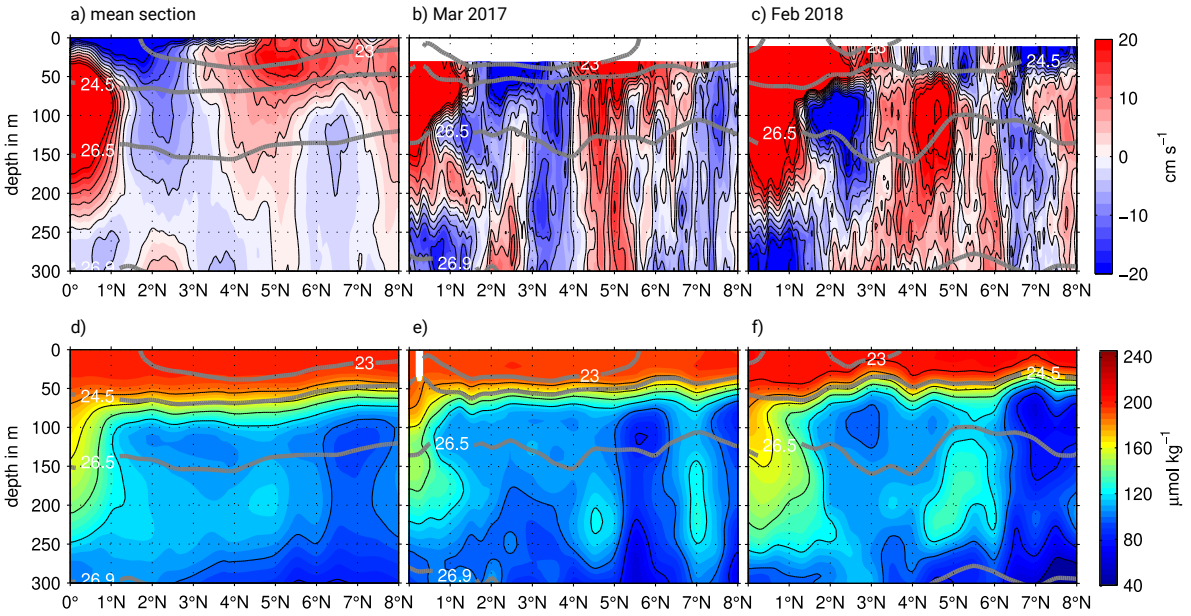

Figure 4.3: Zonal velocity (a-c) and oxygen (d-f) observations along 23°W with mean sections of all 24 cruises (d,e) as well as sections taken during Ronald H. Brown cruise PNE 2017 (f,g) and during Meteor cruise M145 (h,i).

4.6 NEUC and oxygen

The NEUC is thought to transport oxygen rich water from the western boundary towards the generally poorly ventilated eastern tropical North Atlantic (Stramma et al., 2008a; Brandt et al., 2010; Hahn et al., 2017). The mean ship section indicates a local oxygen maximum which is associated with the NEUC and the single ship sections often show maxima in the area of the NEUC (Fig. 4.3). Here we will investigate this link using the moored observations.

To investigate whether the strong eastward transport events are associated with high oxygen levels, we calculate oxygen anomalies on isopycnals. First, a temporal mean oxygen profile as a function of density was calculated from the mooring time series. Next, for each time step, the oxygen anomaly was calculated with respect to the mean oxygen value of the respective density. Finally we applied a 75-day low-pass Butterworth filter order 2 to both, the transport and the oxygen time series (Fig. 4.4).

In 100 m and 200 m depth, which is within the NEUC depth range, the oxygen and transport time series agree well for 2017 but no significant correlation is found for the other years. For 300 m just below the NEUC no correspondence between the NEUC transports and oxygen is visible.

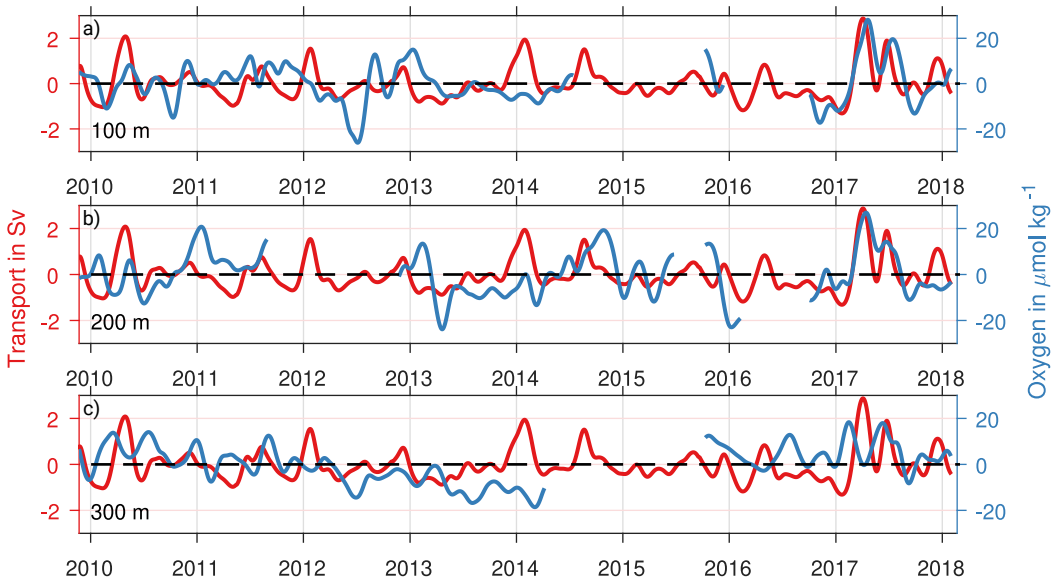

Figure 4.4: 75-day low-pass filtered reconstructed NEUC transport (red lines, same in all panels) and oxygen anomalies (blue lines). The oxygen time series are measured at a depth of (a) 100 m, (b) 200 m, and (c) 300 m.

4.7 Summary and Discussion

The NEUC is an eastward flowing current centered around 5°N in the tropical Atlantic. Although its core velocity is weak (below 0.3 m s^{-1}) it is thought to act as an important oxygen supply route towards the eastern tropical North Atlantic oxygen minimum zone (Stramma et al., 2008a; Brandt et al., 2010; Hahn et al., 2017). For the first time we reconstructed a time series of the NEUC transport based purely on direct velocity observations. By combining moored zonal velocities at 5°N, 23°W and meridional ship sections along 23°W we obtained a NEUC transport time series from June 2006 to February 2008 and November 2009 to January 2018. In contrast to previous studies (Hüttl-Kabus and Böning, 2008; Goes et al., 2013; Burmeister et al., 2019), neither the moored zonal velocities at 5°N (Fig. 4.1) nor the reconstructed eastward transport time series (Fig. 4.2) exhibit a pronounced seasonal cycle. We find that both time series are dominated by strong intraseasonal eastward flow events which can peak throughout the year (Fig. 4.1 and 4.2). Although in the ship sections the NEUC commonly coincides with a local oxygen maximum (Fig. 4.3), we find that the strong eastward flow events are only occasionally associated with high oxygen levels (Fig. 4.4).

We reconstructed the NEUC transport at 23°W based on velocity observations from three moorings and 24 meridional ship sections (Fig. 4.2). In a next step, we reconstructed the NEUC variability based on data from only one mooring position. The

comparison with the three-mooring solution indicates that the variability is dominated by an homogeneous structure covering the complete integration box (Fig. 4.S3). However, the method has some limitations. The used integration box does not cover the complete NEUC region (Fig. 4.S1). Consequently, our method is underestimating the true NEUC transport. We compared the box integrated transport calculated from the ship section with a reference transport calculated from the ship sections using a path following algorithm. The box integrated transport represents the variability of the NEUC reasonably well (R=0.9, Fig. 4.S2 and 4.S5). An additional uncertainty of the reconstructed transport is given by the upper range of the moored velocity observations that varies between 65 m and 85 m, i.e. the moored velocities do not always cover the complete NEUC depth range. In summary, the used method is underestimating the true NEUC strength but it is still capable of representing its variability, as this is dominated by a homogeneous structure in latitude and depth.

The reconstructed NEUC transport time series is characterized by intraseasonal eastward flow events. The dominance of intraseasonal variability suggests that the upwelling within the Guinea dome in the eastern basin as suggest by McCreary et al. (2002) and Furue et al. (2007, 2009) may not be of first order in forcing the observed NEUC transport variability. We here want to briefly discuss potential driving mechanisms of the intraseasonal eastward flow events. As the NEUC at 5°N, 23°W appears to be rather weak, strong eastward transport events can generally be caused by different mechanisms triggering Rossby waves that alter the weak mean flow. Rossby waves at 5°N, 23°W may be directly wind-driven or may be remotely generated by reflection of equatorial Kelvin waves at the eastern boundary as well as by the radiation of Rossby waves from coastally trapped waves generated in the Gulf of Guinea. A linear regression of wind stress curl anomalies onto the reconstructed NEUC transport shows negative wind stress curl anomalies between 3°N to 6°N just off the coast of Liberia leading the NEUC transport time series by one to two months (Fig. 3.S6, Text S3). Such a localized forcing could initiate Rossby waves that may cause the observed events. Furthermore, we calculate composite Hovmöller diagrams of anomalous zonal wind stress between 2°S and 2°N (Fig. 3.S7a) and sea level anomalies (SLAs) between 1°S and 1°N as well as between 2°N and 5°N (Fig. 4.S7b,c). One to three months before a strong eastward transport event occurs, we find easterly wind stress anomalies along the equator (Fig. 4.S7a) that trigger an upwelling equatorial Kelvin wave (Fig. 4.S7b), traveling along the equator towards the eastern boundary where it is reflected into an upwelling Rossby wave (Fig. 4.S7c) that propagates westward between 2°N and 5°N. Simultaneously, positive sea level anomalies occur between between 2°N and 5°N which indicate a downwelling

Rossby wave traveling westward. The equatorial waves and eastward flow events of the NEUC may either be driven by the same mechanism or the equatorial waves themselves may trigger the eastward flow events. For example, the observed upwelling Kelvin wave reaches the eastern boundary about one to two months before the peak of an eastward flow event and is reflected into an westward propagating Rossby wave and a coastally trapped wave. A baroclinic mode one Rossby wave ($c_{R1} \sim 0.9\mathrm{m\,s^{-1}}$) travels the distance between 10°E and 23°W in approximately 1.5 months. However, in the SLA data such a fast propagation of the reflected upwelling Rossby wave is not clearly visible. Additionally, the duration of the intraseasonal events are close to the cut-off period of equatorial Rossby waves and hence zonal energy propagation of such Rossby waves is low and dissipation is high.

Finally, we investigated the relationship between the NEUC transport and oxygen. We find periods where the eastward transport and oxygen anomalies agree very well (in particular in 2017) suggesting a ventilation of the eastern basin by such pulses. However, for other events we did not find such a relationship (Fig. 4.4). One possible explanation is that the local oxygen maximum associated with the NEUC is not located directly at 5°N as visible in the meridional ship sections of March 2017 (Fig. 4.3b,e). In that case the higher oxygen concentrations are simply not captured by the mooring at 5°N.

In contrast to the mean ship section, in the individual ship sections eastward velocities within the NEUC region do not always coincide with local oxygen maxima. Our results suggest that the NEUC does not continually advect oxygen-rich water from the western boundary towards the eastern basin but rather in some kind of bursts or filaments. Until those oxygen-rich bursts reach as far east as 23°W the zonal velocity field may be already altered by local processes for example by tropical instability waves or other mesoscale recirculations (Weisberg and Weingartner, 1988; Hahn et al., 2014; Burmeister et al., 2019). For example, in the meridional section of February 2018, we find strong eastward velocities between 4°N and 5°N, 50 m and 100 m depth associated with low oxygen concentrations, which might be due to a recirculation of lower oxygenated water typically present south of the NEUC (Fig. 4.4h-i; Burmeister et al., 2019). Simultaneously, centered at around 5°N down to a depth of 250 m, we find much higher oxygen concentrations (>120 μmol $\mathrm{kg^{-1}}$) in February 2018 than in the ship section of March 2017 (Fig. 4.4b and c). This increase in oxygen concentrations may be the result of the two consecutively strong eastward transport events in 2017 associated with positive oxygen anomalies. Although 2017 represents an exceptional year in the transport time series, such high ventilation events may be important for the

mean ventilation and oxygen distribution of the oxygen minimum zone of the eastern tropical North Atlantic and are the reason for the oxygen maximum in the mean ship section along 23°W.

Acknowledgments

This study was funded by the Deutsche Forschungsgemeinschaft as part of the Sonderforschungsbereich 754 "Climate-Biogeochemistry Interactions in the Tropical Ocean," through several research cruises with RV L'Atalante, RV Maria S. Merian, RV Meteor, and RV Polarstern, by the project FOR1740 and by the Deutsche Bundesministerium für Bildung und Forschung (BMBF) as part of projects RACE (03F0651B) and RACE-Synthesis (03F0824C). We thank the captains, crews, scientists, and technical groups involved in the different national and international research cruises to the eastern tropical North Atlantic that contributed to collecting CTD, velocity as well as mooring data, and making them freely available. We thank Rebecca Hummels for postprocessing of the recent mooring and ship section data. The shipboard data are accessible at https://doi.pangaea.de/10.1594/PANGAEA.899052. The mooring data will be made available at pangea (in progress). We are grateful to NOAA/PMEL and NOAA/AOML to make the data of the PIRATA Northeast Extension cruises freely available at https://www.aoml.noaa.gov/phod/pne/cruises.php. ASCAT data were obtained from the Centre de Recherche et d'Exploitation Satellitaire (CERSAT), at IFREMER, Plouzané (France) and are available at ftp://ftp.ifremer.fr/ifremer/cersat/products/gridded/MWF/L3/ASCAT/Daily/. Global Ocean Gridded L4 sea surface heights and derived variables were made available by E.U. Copernicus Marine Environment Monitoring Service (CMEMS). The data is available at http://marine.copernicus.eu/services-portfolio/access-to-products/?option=com_csw&view=details&product_id=SEALEVEL_GLO_PHY_L4_REP_OBSERVATIONS_008_047. The JRA-55 reanalysis surface winds used for this study is provided from the Japanese 55-year Reanalysis (JRA-55) project carried out by the Japan Meteorological Agency (JMA) and is available at https://jra.kishou.go.jp/JRA-55/index_en.html#jra-55 after registration.

4.8 Supporting Information for "Ventilation of the eastern tropical North Atlantic by intraseasonal flow events of the North Equatorial Undercurrent"

Contents of this file

Text S1 to S3, Figures 4.S1 to 4.S7 and Table 4.S1.

Introduction

In section S1 of the Supporting Information we give an detailed overview about the processing of the moored and shipboard observations. Section S2 presents details of the estimations of eastward transports from zonal velocity observations, their accuracies and uncertainties as well as their associated spatial patterns. In section S3 we provide some evidence linking NEUC transport events to wind stress curl and zonal wind stress anomalies.

S1: Moored and shipboard observations

Moored data

For our analysis we used velocity, hydrography and oxygen data from moorings at 5°N/23°W (Jul 2006-Feb 2008, Nov 2009-Jan 2018), 4.6°N/23.4°W (Nov 2012-Apr 2014) and 4.5°N/22.4°W (Nov 2012-Apr 2014). At all three mooring positions horizontal velocity was measured with downward (Jul 2006-Feb 2008) or upward (Nov 2009-Jan 2018) looking 75-kHz Longranger Acoustic Doppler Current Profilers (ADCPs). The ADCP configuration was set to a sampling period of 2 h, a bin length of 16 m and an ensemble number of 20 pings. A single velocity data point has a standard error of 1.7 cm s^{-1}. Given the manufacturer's compass accuracy of 2°, we inferred a velocity error of < 4 % of the absolute measured velocity (Hahn et al., 2014). The minimum measurement range of all mooring periods is 85 m to 755 m. The moored velocity data was linear interpolated onto a regular time-depth grid (12 h $\times$10 m) and a 40-day low-pass Butterworth filter was applied to remove the tidal signal from the time series (Fig. 4.S1).

Eight pairs of oxygen (AADI Aanderaa optodes of model types 3830 and 4330) and CTD sensors (Sea-Bird SBE37 microcats) were installed at the moorings evenly distributed in the depth range from 100 m to 800 m. This configuration allows an appropriate estimate of the dissolved oxygen on density surfaces. All instruments were set

to a sampling rate of $0.5\,h^{-1}$ or higher. The oxygen and CTD sensors are calibrated against CTD casts performed directly prior to or after the deployment period of the mooring. The oxygen sensors are additionally calibrated against laboratory measurements to expand the range of reference calibration points. For more details of the oxygen calibration see Hahn et al. (2014). The root mean square error of moored temperature, salinity and dissolved oxygen measurements was about 0.003°C, 0.006 and $3\,\mu mol\,kg^{-1}$, respectively (see Hahn et al., 2017). The point measured hydrogaphy and oxygen data was interpolated onto a 12-h time grid.

Shipboard data

The 24 meridional velocity and 15 hydrographic and oxygen sections between 21°W and 26°W were obtained during cruises between 2002 to 2018 (Table 4.1). All ship sections cover at least the upper 350 m between 0° and 10°N. The velocity, hydrographic and oxygen ship sections used in this study are an extension of the data set used in Burmeister et al. (2019).

Velocity data are acquired by vessel-mounted ADCPs (vm-ADCPs). Vm-ADCPs continuously record velocities throughout a ship section and the accuracy of 1-h averaged data is better than 2-4 $cm\,s^{-1}$ (Fischer et al., 2003). Hydrographic and oxygen data obtained during CTD casts are typically performed on a uniform latitude grid with half-degree resolution. The data accuracy for a single research cruise is generally assumed to be better than 0.002°C, 0.002 and $2\,\mu mol\,kg^{-1}$ for temperature, salinity, and dissolved oxygen, respectively (Hahn et al., 2017). The velocity, hydrographic and oxygen data are mapped on a regular grid (0.05° latitude × 10 m) and are smoothed by a Gaussian filter (horizontal and vertical influence (cutoff) radii: 0.05° (0.1°) latitude and 10 m (20 m), respectively). The final sections are averaged at each grid point to derive mean sections. For the mean velocity, temperature, salinity and oxygen sections the standard error in the NEUC region ($65 - 270$ m depth, $3° - 6.5°$N) are $1.7\,cm\,s^{-1}$, 0.22°C, 0.02 and $3.8\,\mu mol\,kg^{-1}$, respectively.

S2: NEUC transport calculations

Path following algorithm

We derived estimates of the NEUC transport from the 24 meridional ship sections based on the algorithm of Hsin and Qiu (2012) as follows. First, the central position Y_{CM} of the current is estimated using the conception of centered of mass:

$$Y_{CM}(t) = \frac{\int_{Z_l}^{Z_u} \int_{Y_S}^{Y_N} y\ u(y,z,t)\ dy\ dz}{\int_{Z_l}^{Z_u} \int_{Y_S}^{Y_N} u(y,z,t)\ dy\ dz}, \tag{4.2}$$

where y is latitude, u is zonal velocity, z is depth, t is time, Z_u (Z_l) is upper (lower) boundary of the flow, and $Y_N = 6°\text{N}$ ($Y_S = 3.5°\text{N}$) is northern (southern) limit of the current core.

Now the eastward velocity is integrated within a box whose meridional range is given by $Y_{CM}(t)$ and the southern (B_S) and northern (B_S) extent of the flow:

$$INT(t) = \int_{Z_l}^{Z_u} \int_{Y_{CM}-B_S}^{Y_{CM}+B_N} u(y,z,t)\ dy\ dz \tag{4.3}$$

For the integration we used the same boundary conditions as Burmeister et al. (2019). Z_u is the depth of the $24.5\,\text{kg}\,\text{m}^{-3}$ and Z_l the depth of the $26.9\,\text{kg}\,\text{m}^{-3}$ neutral density surface. The southern boundary is choosen as $Y_{CM} - 1.5°$ and the northern boundary is $Y_{CM} + 1.0°$. Note that, if no hydrographic measurements are available for a single ship section, the neutral density field derived from the mean hydrographic section is used.

Transport reconstruction

The eastward transport associated with the NEUC at 5°N, 23°W is computed using moored velocity data at 5°N/23°W (2006-2018), 4.6°N/22.4°W (Nov. 2012-Apr. 2014), and 4.5°N/23.4°W (Nov. 2012-Apr. 2014) combined with 24 meridional ship sections between 21°W and 26°W (Fig 4.S1). In the main manuscript we reconstruct the NEUC transport using the optimal width (OW) method as described in Brandt et al. (2014). We here want to validate the OW method using another approach from Brandt et al. (2014). Figure 4.S2 presents the relationship between the NEUC transport estimated by the path following algorithm and the reconstructed transports.

In the second approach the latitude-depth velocity fields are reconstructed from the moored zonal velocities by interpolating between the mooring position. For the interpolation we use variability pattern derived from the 24 ship section. Therefor we calculate Hilbert empirical orthogonal functions (HEOF) pattern from the velocity sections between 4.25°N and 5.25°N, 65 m and 270 m (black dashed frame in Fig. 4.S1). Here, a Hilbert transformation is applied to the zonal fields, before an EOF analysis is performed. The adventage of a HEOF is, that the statistical patterns efficiently reveal spatial propagation features as for example a meridional migration of the current, in contrast to a traditional EOF. The first HEOF pattern explains 56% of variability contained in the ship section. The real pattern of the first HEOF shows a homogeneous

change of velocities over the complete integration area (Fig. 4.S3). Using only the first HEOF patterns to interpolate between the mooring positions by regressing the patterns onto the moored zonal velocity observations results in similar reconstructed transports as the OW method (black and red line in Fig. 4.S4). As the homogeneous structure of the first HEOF explains most of the variability, there is no added value by including more HEOF patterns to reconstruct the NEUC transport. Nevertheless we want to mention here, that the second pattern with a explained variance of 20% describes a meridional shift of the NEUC. A vertical shift of the NEUC might be described by the patterns of the third and forth HEOF.

To investigate whether the dominant pattern of first HEOF of the zonal velocities between 4.25°N and 5.25°N represents a meridional migration of the NEUC out of the calculation area the HEOF method is repeated using the zonal velocities between 3.5°N and 6.0°N. This region covers the southern and northern boundary of the NEUC even if the current is meridionally migrating. The fixed box averaged transport for this region calculated from the ship sections (gray squares in Fig. 4.S4) agrees well with the reference transports. Again, the real pattern of the first HEOF shows a homogeneous change of velocity although it explains less variability compared to the first HEOF of the smaller box. Furthermore, the first and second pattern which explain together 66% of the velocity variability seem to describe a meridional shift of the current. Nevertheless, the eastward transport time series reconstructed using the first (yellow line in Fig. 4.S4) or the first two HEOF pattern (blue line in Fig. 4.S4) of zonal velocities between 3.5°N and 6.0°N agrees well with that reconstructed from velocities between 4.25°N and 5.25°N. The mean transport estimates using the bigger box is 1.9 Sv.

In summary, the reconstructed eastward transports between 4.25°N and 5.25°N tend to underestimate the mean current strength of the NEUC, however the time series is able to reconstruct the NEUC variability reasonable well. We choose the smaller box to reconstruct the NEUC transport variability due to the smaller uncertainty of the reconstructed transports when using only the mooring at 5°N, 23°W.

S3: NEUC and sea surface winds

Auxiliary data

Monthly mean JRA-55 surface wind velocities (**?**) on a 1.25°×1.25° horizontal grid for the time period from 2006 to 2018 are used in this study.

We are using monthly mean wind stress from the ASCAT on METOP Level 4 Daily Gridded Mean Wind Fields (Bentamy and Fillon, 2012) with a horizontal resolution of 0.25° covering the time period from April 2007 to May 2018. For the calculation

of the wind stress curl the ASCAT wind stress with a horizontal resolution of 0.25° is regridded onto a horizontal grid of the JRA-55 reanalysis data (1.25°) by bin averaging.

Daily SSALTO/DUACS sea level anomalies (SLAs) from the delayed-time allsat product are produced and distributed by the Copernicus Marine and Environment Monitoring Service (CMEMS) (http://www.marine.copernicus.eu). The data set used here covers the time period 2005 to 2018 and has a spatial resolution of 0.25°.

Linear regression wind stress curl

We perform a lead-lad regression of wind stress curl anomalies with respect to the 2008 to 2017 climatology onto the reconstructed NEUC time series for two different wind products (Fig. 4.S6). In the ASCAT data, a very localized negative wind stress curl anomaly off the coast of Liberia, which is significant on the 95% confidence level, is leading the NEUC transport time series by 2 month (Fig. 4.S6b). In the JRA-55 data, a significant negative wind stress curl anomaly off the coast of Liberia is the leading the NEUC transport by 1 month (Fig. 4.S6g). In both datasets, the observed localized wind stress curl anomaly could initiate Rossby waves that may cause the observed intraseasonal eastward flow events. However, the linear regression pattern of the different wind products differ markedly. Differences in the wind stress products may arise from the different kind of data that is used. Another source of uncertainty may be different Bulk formulas used for the wind stress calculations, which can result in a uncertainty up to 20% (Large and Yeager, 2004).

Composite Hovmöller diagrams

We calculate composite Hovmöller diagrams of anomalous zonal wind stress between 2°S and 2°N (Fig. 4.S7a) and SLAs between 1°S and 1°N as well as between 2°N and 5°N (Fig. 4.S7 b,c). To test the significance of the composites we selected 10000 times eight random dates for the available time period of the satellite data and calculated composites of anomalous zonal wind stress (Apr 2007-May 2018) and SLAs (2005-2018) from 3 months before to 3 months after the randomly selected dates to obtain a probability distribution. If a value of the composite of the true events lies outside of the 95% confidence interval of the probability distribution, it is considered as significant.

One to three months before a strong eastward transport event occurs, we find easterly wind stress anomalies along the equator (Fig. 4.S7a) that trigger an upwelling equatorial Kelvin wave (Fig. 4.S7b), traveling along the equator towards the eastern boundary where it is reflected into an upwelling Rossby wave (Fig. 4.S7c) that propagates westward between 2°N and 5°N. Simultaneously, positive sea level anomalies occur between

Table 4.1: Meridional ship sections between 21°W and 26°W from 2002 to 2018. All sections cover at least the upper 350 m from 0°N to 10°N. For all sections ADCP data is available. Sections including oxygen (O_2) and hydrography (CTD) measurements are marked accordingly.

cruise	date	averaged longitude	latitude	O_2/CTD
Meteor 55	Oct-Nov 2002	24°W	0–10°N	no
Ronald H. Brown A16N	Jun-Aug 2003	26°W	-6-10°N	no
Ronald H. Brown PNE6	Jun 2006	23°W	-5-13.5°N	yes
Ronald H. Brown PNE6	Jun-Jul 2006	23°W	-5-14°N	yes
Meteor 68/2	Jun-Jul 2006	23°W	-4-14°N	yes
L'Atalante IFM-GEOMAR 4	Feb 2008	23°W	-2-14°N	yes
L'Atalante IFM-GEOMAR 4	Mar 2008	23°W	-2-14°N	no
Ronald H. Brown PNE09	Jul-Aug 2009	23°W	0-14°N	no
Meteor 80/1	Oct-Nov 2009	23°W	-6-14°N	yes
Meteor 81/1	Feb-Mar 2010	21°W	-6-13°N	no
Ronald H. Brown PNE10	May 2010	23°W	0-14°N	yes
Maria S. Merian 18/2	May-Jun 2011	23°W	0-14°N	no
Ronald H. Brown PNE11	Jul-Aug 2011	23°W	0-14°N	no
Maria S. Merian 22	Oct-Nov 2012	23°W	-6-8°N	yes
Maria S. Merian 22	Oct-Nov 2012	23°W	0-14°N	no
Ronald H. Brown PNE13a	Jan-Feb 2013	23°W	0-14°N	no
Ronald H. Brown PNE13b	Nov-Dec 2011	23°W	-6-14°N	yes
Meteor 106	Apr-May 2014	23°W	-6-14°N	yes
Polarstern PS88.2	Nov 2014	23°W	-2-14°N	yes
Endeavor EN-550	Jan 2015	23°W	-2-14°N	yes
Meteor 119	Sep-Oct 2015	23°W	-5.5-14°N	yes
Meteor 130	Aug-Oct 2016	23°W	-6-14°N	yes
Ronald H. Brown PNE17	March 2017	23°W	-4-14°N	yes
Meteor 145	Feb-Mar 2018	23°W	-6-14°N	yes

between 2°N and 5°N which indicate a downwelling Rossby wave traveling westward, however these anomalies are not significant. The simultaneous appearance of equatorial waves and eastward flow events of the NEUC suggests that either they are driven by the same mechanism or that the equatorial waves themselves trigger the eastward flow events.

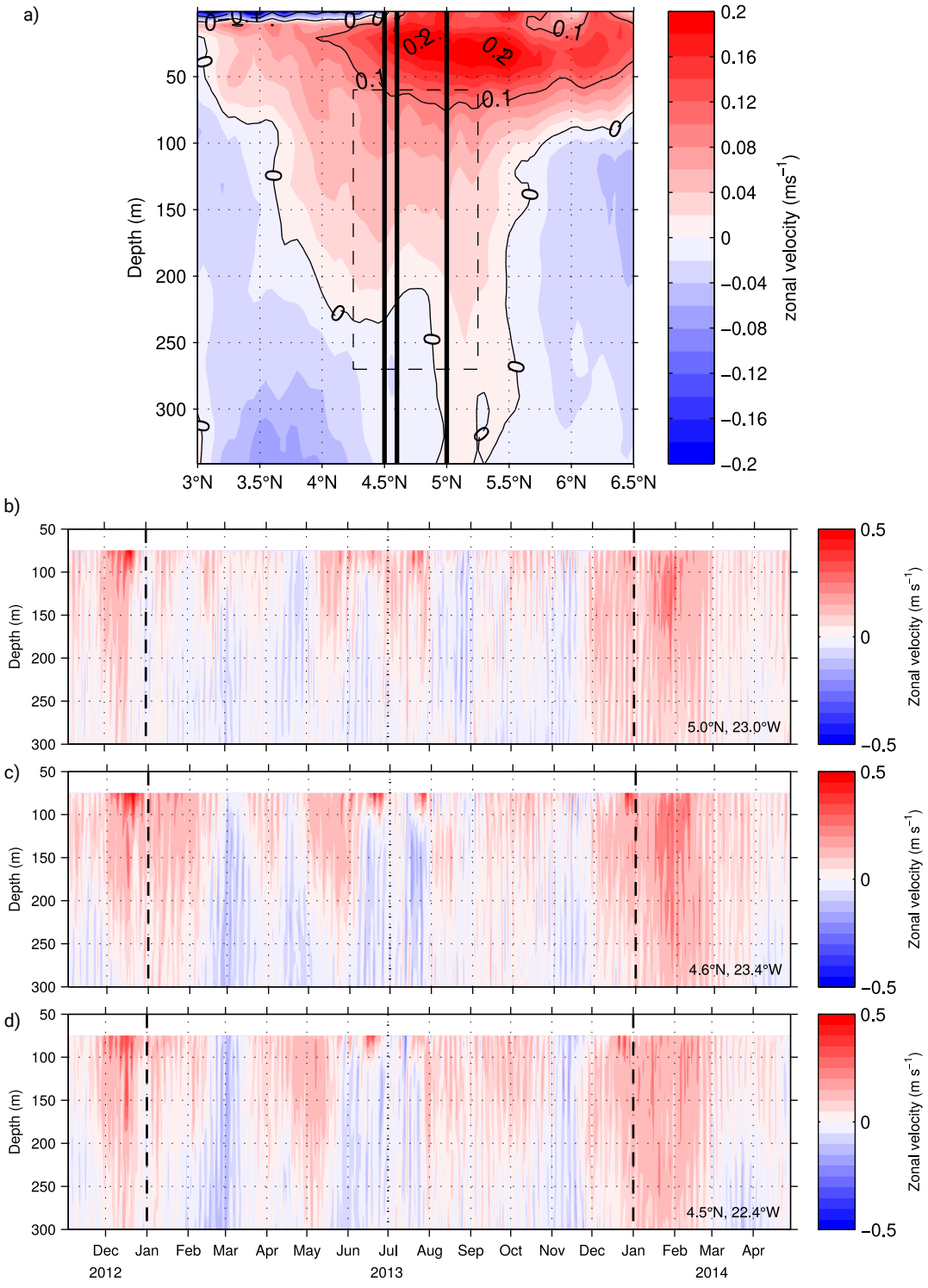

Figure 4.S1: (a) Mean zonal velocity sections along 23°W estimated based on 24 ship sections acquired by cruises from 2002 to 2018. Black vertical lines mark the position of the three moorings. The black dashed frame mark the box for the transport reconstruction. (b,c,d) Zonal velocity observations ar the mooring position (b) 5.0°W, 23°W, (c)4.6°N,23.4°W and (d) 4.5°N, 22.4°W.

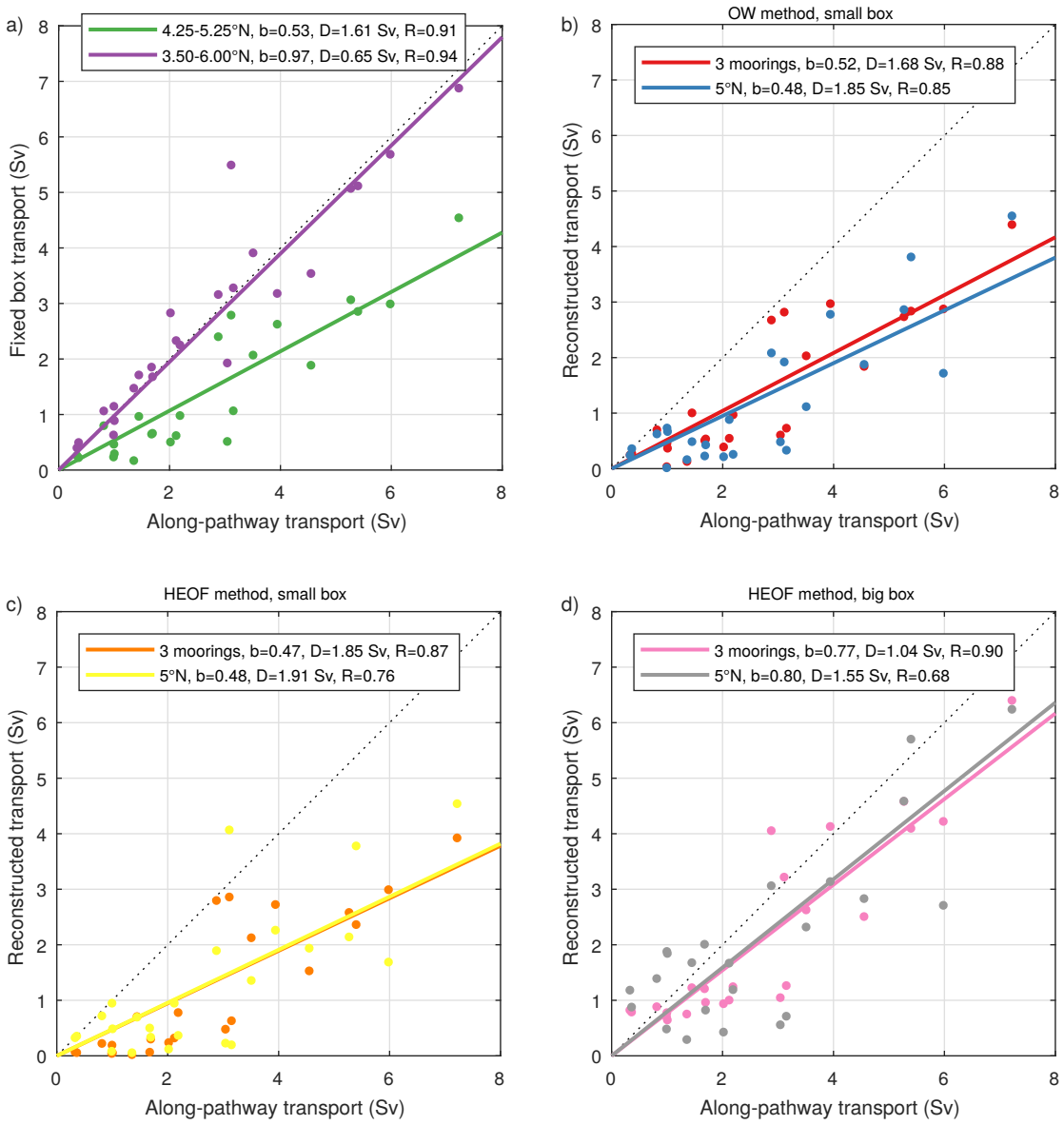

Figure 4.S2: Regression slope b, mean difference D and correlation coefficient R between the reference NEUC transport (Along-pathway transport) and the reconstructed transports based on different methods: (a) fixed box integrated transports between 4.25°N and 5.25°N (green) as well as between 3.50°N and 6.00°N (purple), (b) OW method using 3 moorings (red) and only the 5°N mooring, (c) HEOF method using the first HEOF pattern calculated from 3 moorings (orange) and only the 5°N mooring (yellow) for the area between 4.25°N and 5.25°N, (d) HEOF method using the first HEOF pattern calculated from 3 moorings (pink) and only the 5°N mooring (grey) for the area between 3.50°N and 6.00°N.

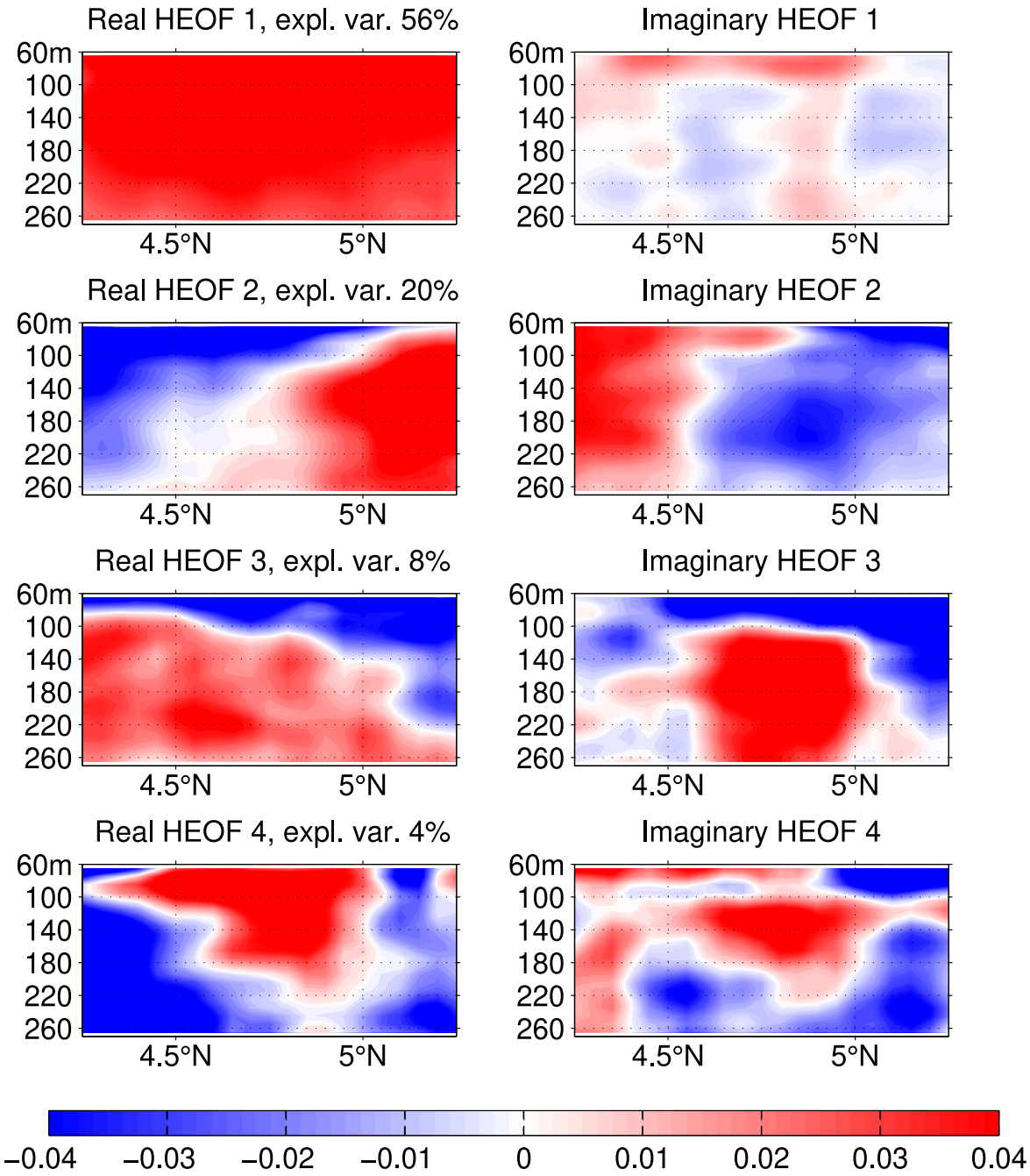

Figure 4.S3: Real (left side) and imaginary (rigth side) pattern of the first four Hilbert empirical orthogonal functions calculated from the 24 zonal velocity section along 23°W between 4.25°N and 5.25°N, 65 m and 270 m depth.

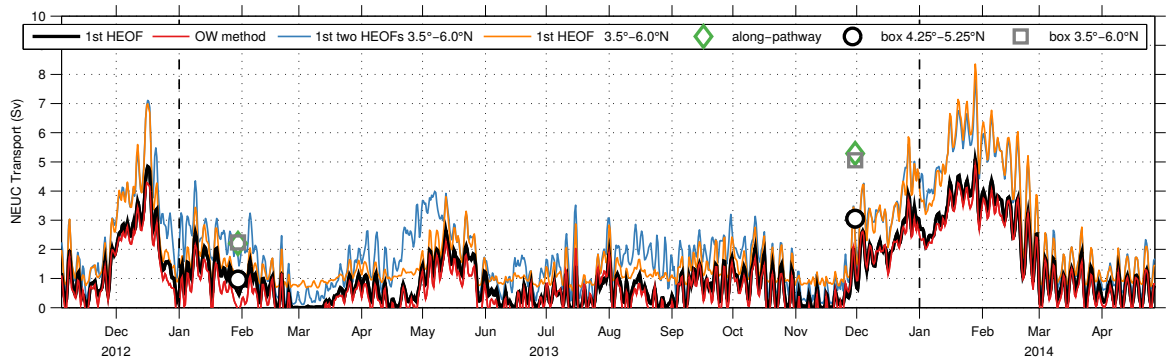

Figure 4.S4: NEUC transport at 23°W calculated by different methods: (i) from ship observations using a path following algorithm (green diamonds); (ii) from ship section by integrating the eastward velocities in a fixed box between 4.25°N and 5.25°N (black circles) and 3.5°N and 6.0°N (grey squares); (iii) by the HEOF method combining ship sections and moored zonal velocities at three mooring positions using the first HEOF of velocities between 4.25°N and 5.25°N (black line) as well as using the first (yellow line) or the first two (blue line) HEOF of velocities between 3.5°N and 6.0°N; (iv) by the OW method combining ship sections and moored zonal velocities at three mooring positions (black line).

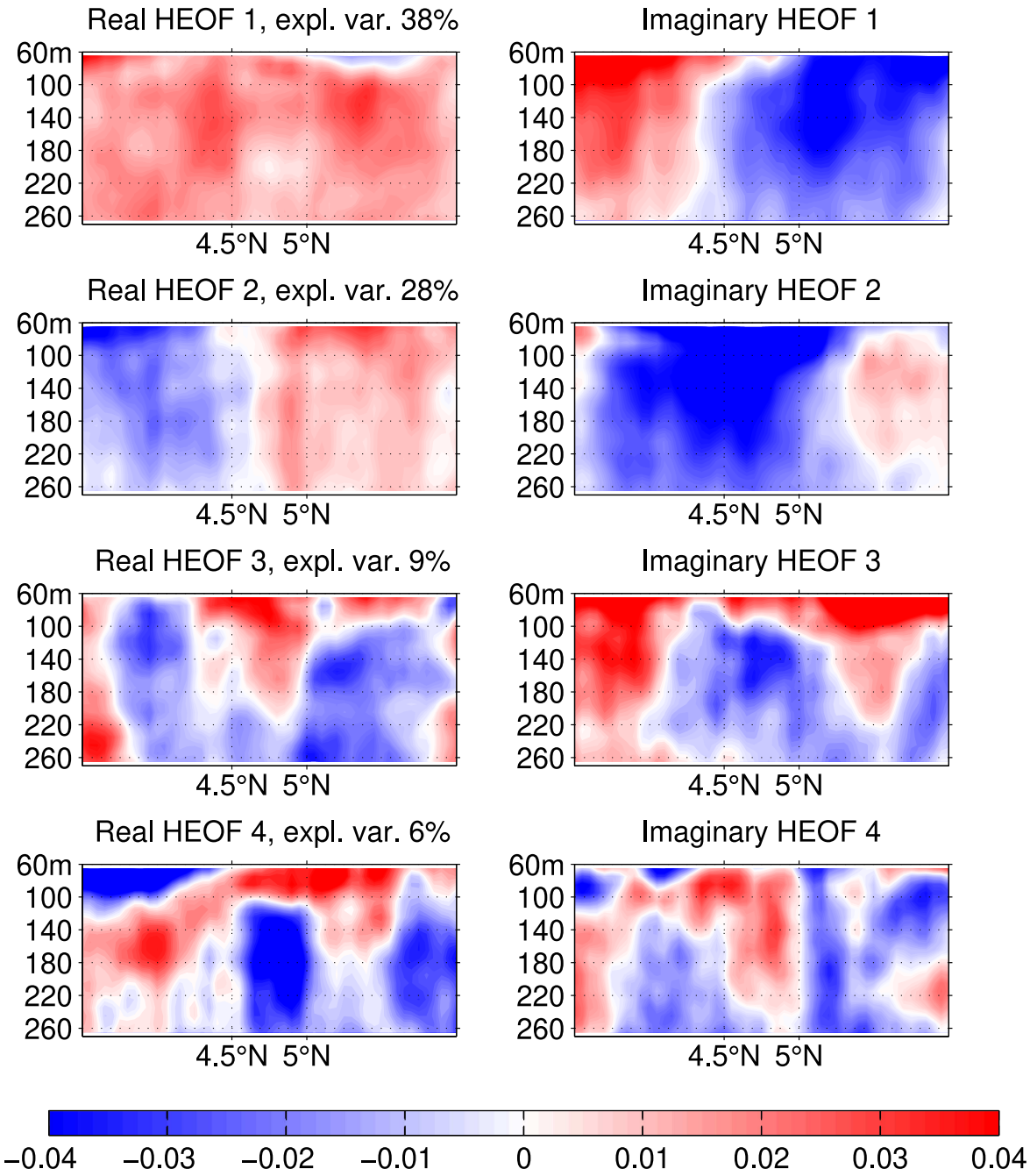

Figure 4.S5: Real (left side) and imaginary (rigth side) pattern of the first four Hilbert empirical orthogonal functions calculated from the 24 zonal velocity section along 23°W between 3.5°N and 6.0°N, 65 m and 270 m depth.

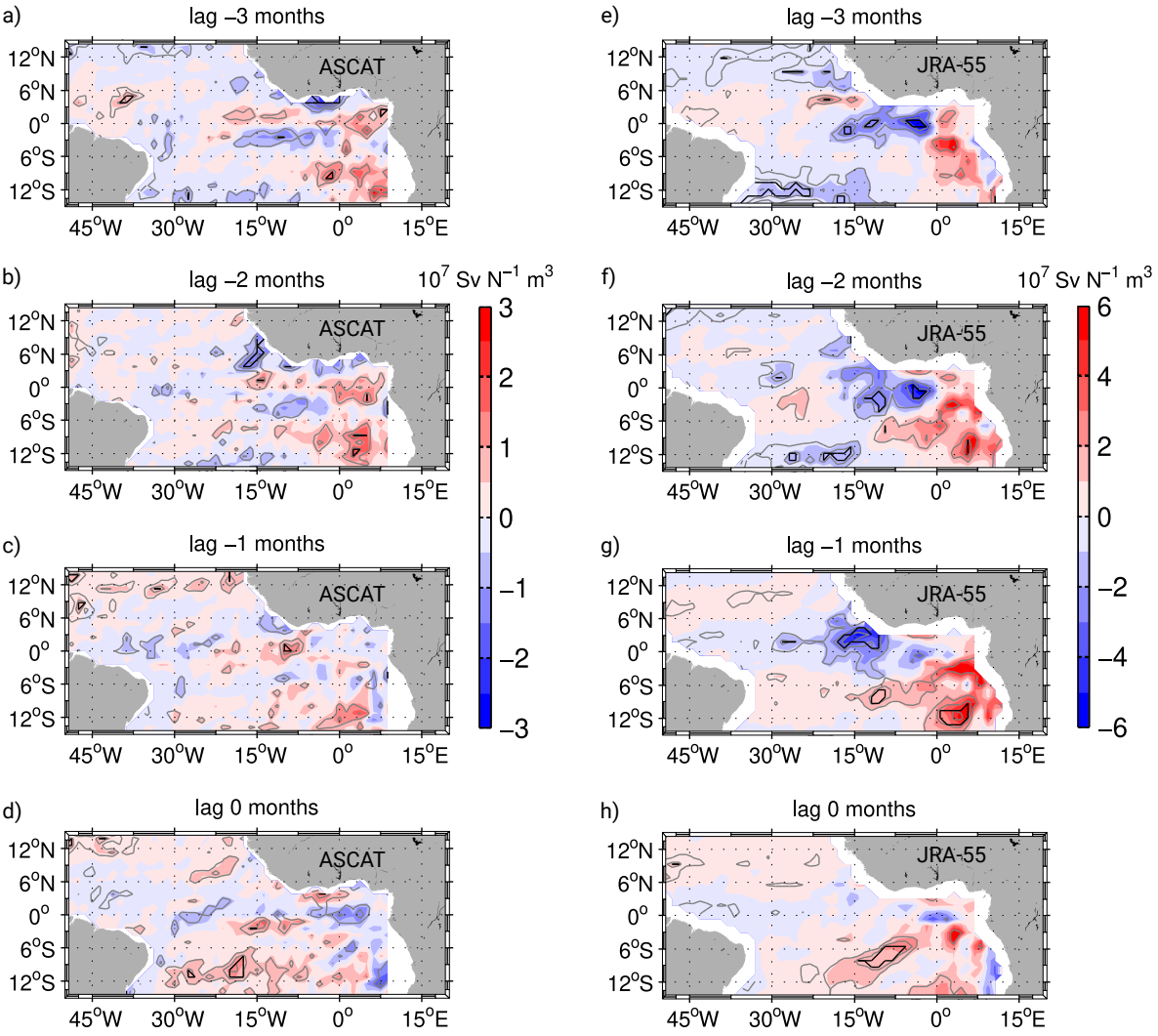

Figure 4.S6: Slope of lead-lag regression of monthly mean wind stress curl anomalies with respect to the 2008-2017 climatology onto the reconstructed monthly mean NEUC transport time series. Results are shown for ASCAT (a-d) and JRA-55 reanalysis (e-h) data. Gray contours show the coefficient of correlation (R) with an interval of 0.1. Black contours mark significant values of R.

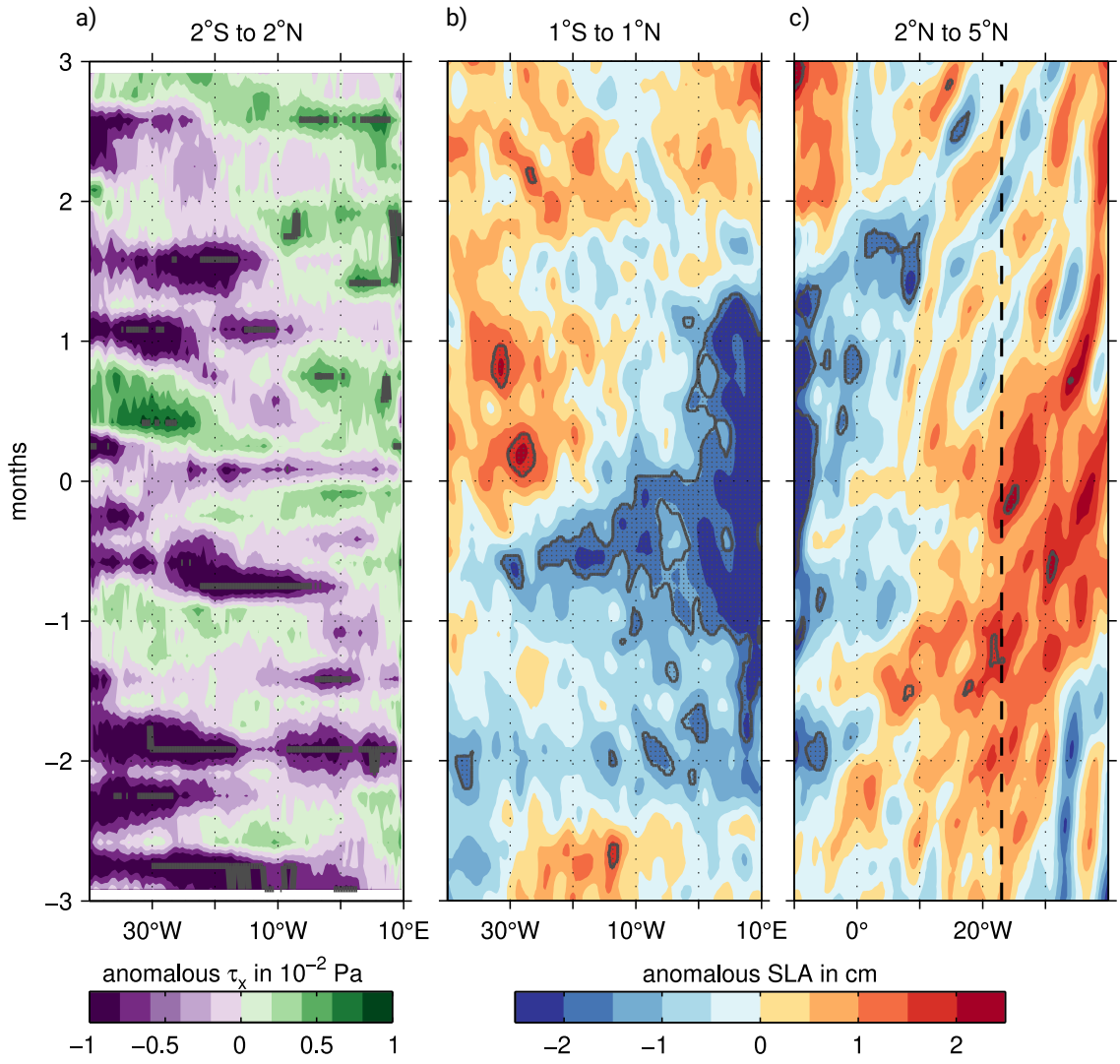

Figure 4.S7: Composites of (a) 5-daily ASCAT zonal wind stress anomalies and (c,d) daily anomalous SLA averaged between (a) 2°S and 2°N, (b) 1°S and 1°N, as well as (c) 2°N and 5°N from 3 months before to three months after the peak of an eastward transports event. Note that the x-axis of c is reversed. Dotted areas within grey contour lines mark anomalies that are significant at the 95% confidence level.

4.9 Excursus: The role of resonant equatorial basin modes for the seasonal variability of the zonal velocities at 5°N, 23°W

In the previous sections, a weak annual and semi-annual cycle was found for the moored zonal velocity observations at 5°N, 23°W (Fig. 4.1), which will be further investigated in this excursus. A special focus is laid on the role of resonant equatorial basin modes for the wind-driven seasonal variability of the zonal velocity field. Resonant equatorial basin modes are low-frequency standing equatorial modes consisting of long equatorial Kelvin and Rossby waves (Cane and Moore, 1981). Depending on the gravity wave speed and the basin geometry, each baroclinic mode has a characteristic resonance period. In the equatorial Atlantic, the semiannual, annual and interannual variability of the zonal flow is attributed to the resonance period of the gravest basin mode for the second, the forth and higher baroclinic modes, respectively (Thierry et al., 2004; Ascani et al., 2006; D'Orgeville et al., 2007; Ding et al., 2009; Greatbatch et al., 2012; Claus et al., 2016; Brandt et al., 2016). Idealized simulations using a linear wave model have suggested that these modes might also impact zonal velocities along 5°N (Brandt et al., 2016; Kopte et al., 2018). In this section, the influence of resonant equatorial basin modes on velocities along 5°N is revisited using a linear shallow water model.

4.9.1 Shallow Water Model

Following the approach of previous studies, a suite of linear shallow water model simulations was set up, where each realization represents the solution for a single baroclinic mode forced with a climatological wind forcing (Greatbatch et al., 2012; Brandt et al., 2016; Zhu et al., 2017; Kopte et al., 2018).

Governing Equations

The governing equations associated with a particular baroclinic mode n in spherical coordinates are given by (see also Greatbatch et al., 2012; Zhu er al., 2017; Kopte et al., 2018):

$$\frac{\partial u_n}{\partial t} - fv_n = -\frac{g}{a\cos\theta}\frac{\partial \eta_n}{\partial \lambda} + \frac{\tau_s^x}{\rho H_E}G_n + F^u, \tag{4.4}$$

$$\frac{\partial v_n}{\partial t} + fu_n = -\frac{g}{a}\frac{\partial \eta_n}{\partial \theta} + \frac{\tau_s^y}{\rho H_E}G_n + F^v, \tag{4.5}$$

$$\frac{\partial \eta_n}{\partial t} + \frac{H_n}{a\cos\theta}\left[\frac{\partial u_n}{\partial \lambda} + \frac{\partial\left(\cos\theta v_n\right)}{\partial \theta}\right] = 0, \tag{4.6}$$

where θ is latitude, λ is longitude, a the radius of the earth, $f = 2\Omega sin(\theta)$ the Coriolis parameter with Ω the angular speed of the earth, g the acceleration caused by gravity, ρ representative density for seawater, u and v are the zonal (eastward) and meridional (northward) velocity components, respectively, h is the isopycnal displacement, H_E is the depth scale for the surface Ekman layer, H_n is the equivalent depth set by the wave speed $c_n = \sqrt{gH_n}$ associated with the respective baroclinic mode n, τ_s^x and τ_s^y are the zonal and meridional components of the surface wind vector, respectively, acting as body force with G_n the wind stress projection coefficient associated with the respective baroclinic mode n. G_n is first set equal 1 in the simulations and is afterwards derived according to the approaches of Zhu et al. (2017) and Kopte et al. (2018) described below (section 4.9.2). The lateral mixing of momentum F^u and F^v is given by:

$$F^u = \frac{A_h}{a^2}\left[\frac{1}{\cos^2\theta}\frac{\partial^2 u}{\partial \lambda^2} + \frac{1}{\cos\theta}\frac{\partial}{\partial\theta}\left(\cos\theta\frac{\partial u}{\partial\theta}\right) + u(1-\tan^2\theta) - \frac{2\sin\theta}{\cos^2\theta}\frac{\partial v}{\partial\lambda}\right], \tag{4.7}$$

$$F^v = \frac{A_h}{a^2}\left[\frac{1}{\cos^2\theta}\frac{\partial^2 v}{\partial \lambda^2} + \frac{1}{\cos\theta}\frac{\partial}{\partial\theta}\left(\cos\theta\frac{\partial v}{\partial\theta}\right) + v(1-\tan^2\theta) - \frac{2\sin\theta}{\cos^2\theta}\frac{\partial u}{\partial\lambda}\right], \tag{4.8}$$

where A_h is the horizontal eddy viscosity coefficient.

Model Setup

The model domain covers the Atlantic from 20°S to 20°N and 62.5°W to 15°E and has a spatial resolution of 0.1°. The coastline is defined by the 1000-m isobath. Sponge layers with e-folding scale of 2.5° are applied to the southern and northern boundary of the model domain to inhibit Kelvin wave propagation. An Ekman layer depth of 500 m and a lateral eddy viscosity of 100 m^2s^{-1} is chosen. Model simulations for different gravity wave speeds ($c_1 = 2.47ms^{-1}$, $c_2 = 1.32ms^{-1}$, $c_3 = 0.95ms^{-1}$,$c_4 = 0.74ms^{-1}$, $c_5 = 0.57ms^{-1}$; Brandt et al., 2016) are performed, where each simulation represents one of the first 5 baroclinic modes. Each model simulation is driven by the climatological forcing of the JRA55-do surface dataset (Tsujino et al., 2018) and is run for 20 years,

which is sufficient to reach equilibrium at the Equator. The last 5 years of each run are used for the analysis.

4.9.2 Deriviation of the wind stress projection coefficients

The wind stress projection coefficients enable a scaling of the shallow water model output based on the modal decomposition of observations, which is necessary for a direct comparison between simulated and observed zonal velocities.

Additional Observational Data

For the scaling of the shallow water model, top-to-bottom moored zonal velocity observations at 0°, 23°W from December 2001 to February 2018 are used, representing an extensions of the data set used in Brandt et al. (2016), Kopte et al. (2018) and Tuchen et al. (2018). The data set combines moored ADCPs measurements (upper 600-900 m), single-point current meters (600-1000 m depth), a McLane Moored Profiler (MMP, 1000-3500 m depth), and lowered-ADCP profiles taken during the mooring services near the mooring position (see Tuchen et al., 2018, for further details of the mooring setup). The ADCP and single-point current meter data were detided using a 40-h low-pass filter and subsampled to a 12 h resolution. Every 4 to 6 days, the MMP performed an upcast followed by a downcast 6 h afterwards. Due to the relatively large sample interval of the MMP, no filter was applied to the MMP data.

Modal decomposition of moored zonal velocities at 0°, 23°W

The modal decomposition is performed based on vertical structure functions $\hat{p}_n(z)$ of the first five baroclinic modes used in Kopte et al. (2018). They are a subset of those derived by Claus et al. (2016) from a mean buoyancy frequency profile obtained from 47 shipboard CTD profiles. The CTD profiles were acquired during mooring services near 0°, 23°W. $\hat{p}_n(z)$ are calculated for an ocean depth of $H = 4500$m and have been normalized so that $\int_{-H}^{0}[\hat{p}_n(z)]^2 dz = H$.

Due to the different vertical extent of the moored velocity observations and the vertical structure functions, the deepest value of the moored velocity time series at each time step is extended to a depth of 4500 m, but only if it exists below 3000 m depth. This approach is necessary in order to constrain the fit between $\hat{p}_n(z)$ and the moored observations in the vertical direction. Now, $\hat{p}_n(z)$ of the first 20 baroclinic modes

($n = 1, 2, ..., 20$) multiplied with either the annual or semi-annual cycle are consecutively projected onto the zonal velocity observations. This is realized by optimizing the following linear equations system for each baroclinic mode:

$$\begin{aligned} \hat{p}_n(z)\sin(w_j t)\, a_{n,j} &= u(z,t), \quad \text{and} \\ \hat{p}_n(z)\cos(w_j t)\, a_{n,j} &= u(z,t), \end{aligned} \tag{4.9}$$

where w_j is the angular frequency of the annual or semi-annual cycle, t is time, $a_{n,j}$ and $b_{n,j}$ are the amplitudes for sine and cosine fitting, respectively, and u is the observed zonal velocity at 0°, 23°W. The modal amplitude $A_{n,j}$ of the observed zonal velocity associated with a baroclinic mode n is then given by $A_{n,j} = \sqrt{a_{n,j}^2 + b_{n,j}^2}$. After the linear system is solved for an arbitrary baroclinic mode, the fitted zonal velocity associated with the baroclinic mode $\hat{p}_n(z)\cos(w_j t)\, a_{n,j} + \hat{p}_n(z)\sin(w_j t)\, a_{n,j}$ is subtracted from the observed velocity field before the next baroclinic mode is fitted to the velocity time series. As the velocity observations are incomplete and do not cover the complete 4500 m, orthogonality of the modal decomposition is not given. Consequently, this procedure is repeated 10.000 times with random order of the fitted baroclinic modes in order to estimate the most likely mode energies and phases as well as the associated uncertainties (Fig. 4.E1). The results agree well with those obtained by Kopte et al. (2018) for the period 2004 to 2016.

Scaling of model-computed modal amplitudes

For each baroclinic mode a wind stress projection coefficient G_n is calculated separately for the annual and semi-annual cycle following the approach of Zhu et al. (2017) and Kopte et al. (2018). G_n is given by the ratio of modal amplitudes of the zonal velocity derived from observations and the corresponding model-computed modal amplitudes at 0°,23°W (Tab. 4.2). Using this approach, the model-computed modal amplitudes are scaled to fit the observations, while the model-computed modal phases are not changed. Please note that the simulated resonant basin modes depend mainly on the chosen gravity wave speed and the basin geometry. Hence, the derived wind stress coefficients not only represent the wind energy input alone. They rather indicate how much energy is needed to simulate similar modal amplitudes as the observed ones at a given oscillation period.

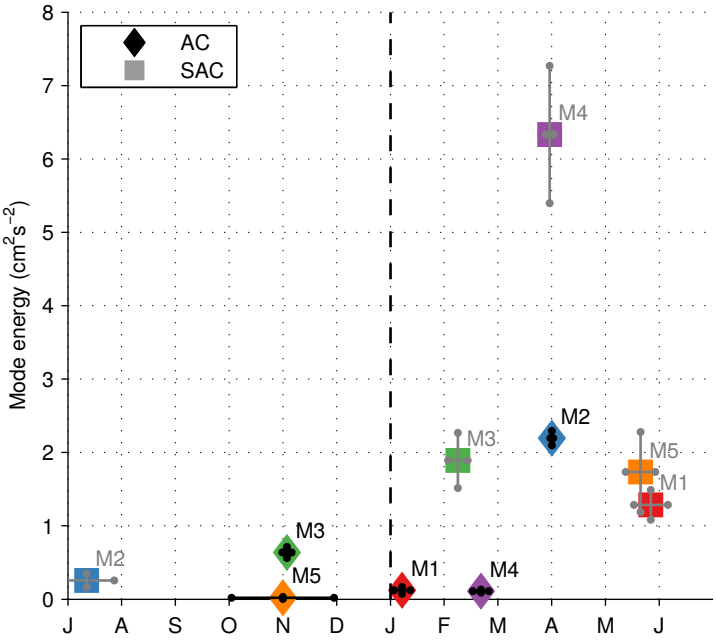

Figure 4.E1: Modal energy and phase of the first five baroclinic modes derived from moored zonal velocities at 0°, 23°W at the time of maximum surface velocity for the annual (AC, squares) and semi-annual cycle (SAC, diamonds). For clarity, only one maximum of the semi-annual cycle is shown. The error bars show the standard deviation of the modal energies and phases resulting from uncertainties of the modal decomposition due to data gaps.

Table 4.2: Dimensionless wind stress projection coefficients G_n derived for different shallow water model simulations representing the first 5 baroclinic modes. G_n is derived for the annual cycle (AC) and the semi-annual cycle (SAC) separately.

mode n	G_n (AC)	G_n (SAC)
1	0.71	0.19
2	0.11	0.32
3	0.06	0.20
4	0.06	0.05
5	0.06	0.03

4.9.3 Results

The annual and semiannual harmonic fitted to the moored velocity observations at 5°N, 23°N are shown in Figure 4.E2a and b. The observed annual harmonic has a maximum amplitude of 3 $\mathrm{cm\,s^{-1}}$ located between 100 m to 200 m depth. The observed semi-annual harmonic has a maximum amplitude of 5 $\mathrm{cm\,s^{-1}}$ that is confined to the uppermost observations between 65 m and 100 m depth. Above 100 m, the semiannual cycle is much stronger than the annual cycle.

For the shallow water model simulations, the annual and semi-annual cycle of the zonal velocity field at the mooring position are reconstructed by summing up the first five baroclinic modes, which are scaled by the respective wind stress projection coefficients (Tab. 4.2). Then the annual and semi-annual harmonic are fitted to the reconstructed velocity field (Fig. 4.E2c, d). The observed semi-annual cycle fits well to the one reconstructed by the superposition of the first five baroclinic modes simulated by the shallow water model (Fig. 4.E2b, d). Interestingly, the superposition of simulated baroclinic modes fails to represent the observed annual cylce of zonal velocity at 5°N, 23°W (Fig. 4.E2a, c). Using solely the simulation representing baroclinic mode 4, the annual cycle of zonal velocity at 5°N, 23°W can be reconstructed reasonably well (Fig. 4.E2e).

4.9.4 Summary and Discussion

In this section, the role of resonant equatorial basin modes for the wind-driven seasonal cycle of moored zonal velocity observations at 5°N, 23°N is investigated. A suite of shallow water models, where each simulation represents one of the first five baroclinic modes, is used to reconstruct the zonal velocity field at the mooring position. While the phase and amplitude of the semiannual cycle simulated by the first five baroclinic modes fit well to the observed ones, the annual cycle could not be reconstructed by the superposition of the first five baroclinic modes. Only baroclinic mode four is able to reproduce the phase and amplitude of the observed seasonal cycle reasonably well.

The discrepancies between observed and modeled seasonal cycle may be caused by the simplified nature of the shallow water model. The results suggest that only the fourth baroclinic mode can simulate the phase and amplitude of the observed seasonal cycle. Consequently, processes which dissipate the other baroclinic modes at the annual frequency might be missing in the shallow water model. As noted in Kopte et al. (2018), the shallow water model does not account for large-scale changes in stratification or topographic features, which might cause changing wave speeds or a scattering of

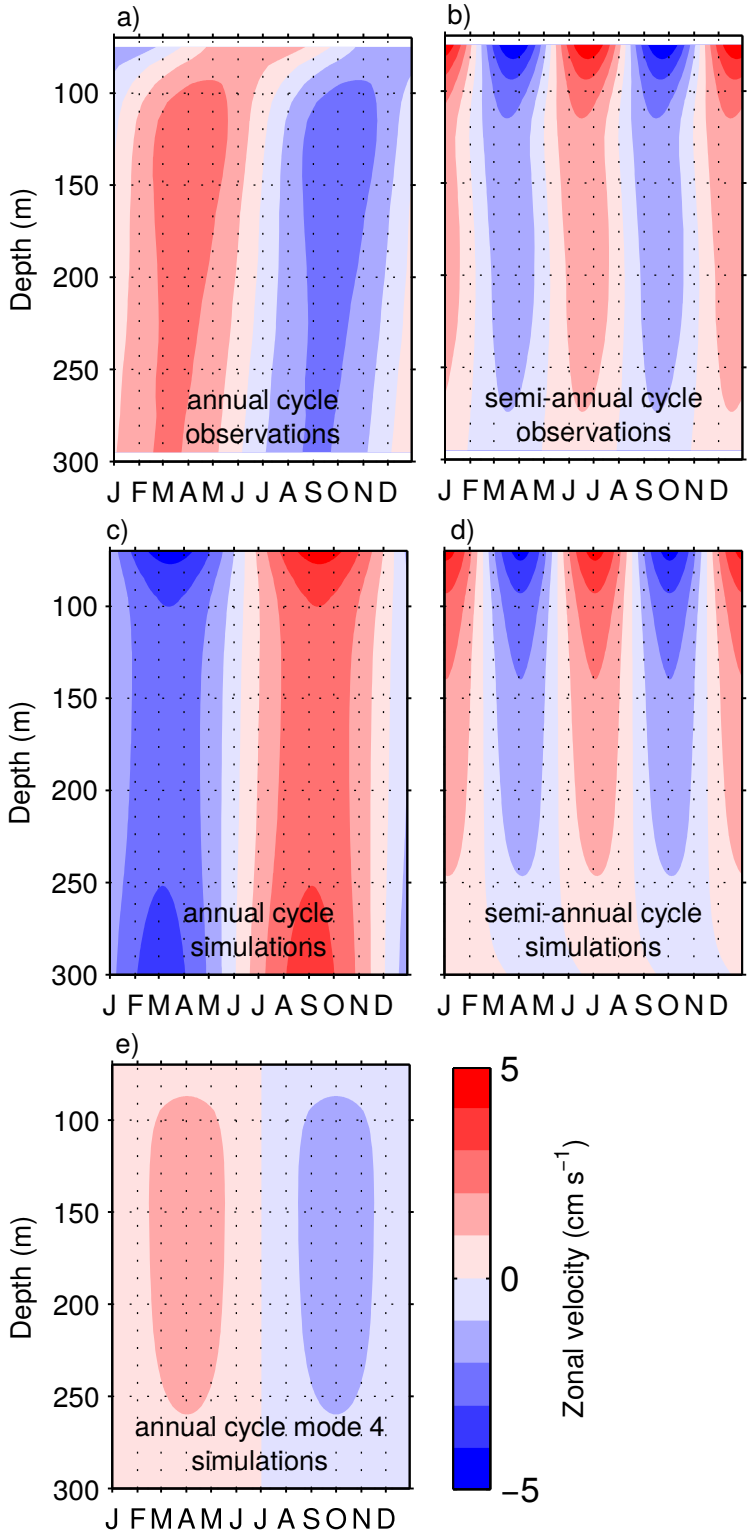

Figure 4.E2: (a,c,e) Annual and (b,d) semiannual harmonic fit to (a,b) the zonal velocity observations and the reconstructed velocities simulated by (c,d) the first five baroclinic modes or (e) baroclinic mode four of the shallow water model at 5°N, 23°W.

baroclinic waves. Consequently, the potential energy transfer between baroclinic modes is not included in the model. For example, the pull of the upwelling within the Guinea dome is a potential process that may influence the seasonal variability of the NEUC (McCreary et al., 2002; Furue et al., 2007, 2009), which is not simulated by the shallow water model. Other non-linear mechanisms that may contribute to the seasonal cycle of the NEUC and are not captured by the linear shallow water model are the interaction of equatorial waves with the mean flow (Claus et al., 2014) and the Eliassen-Palm flux of TIWs (Jochum and Malanotte-Rizzoli, 2004).

5 Decadal to mulditdecadal variability of the NEUC

After the previous sections discussed the intraseasonal to interannual variability of the NEUC in both a state-of-the-art OGCM and observations, this chapter focuses on the decadal to multidecadal variability of the NEUC. Unfortunately, observations within the NEUC region are still too sparse to investigate decadal or longer time variability. Hence, this chapter is based on model output. For the analysis the same OGCM and conceptual model as in chapter 3 are used. In the OGCM, a stronger and more northward positioned NEUC is associated with a positive wind stress curl anomaly north of about 4°N and a negative one south of it. The resulting anomalous Sverdrup transport induces anomalous eastward flow along the core of the NEUC. Experiments with the conceptual model suggest that a strengthening of the NEUC on decadal to multidecadal time scale can result in a better ventilation of the eastern basin between 2.5° and 6.5°N.

5.1 Introduction

Changes of the zonal advection of oxygen have been suggested to play an important role in the decadal to multidecadal variability of the ETNA OMZ (Brandt et al., 2010; Hahn et al., 2017). Decadal to multidecadal variability in the tropical Atlantic has been related to different influencing factors including the wind-driven circulation (Hüttl and Böning, 2006; Rühs et al., 2015; Brandt et al., 2015; Duteil et al., 2014), the AMOC (e.g. Latif et al., 2006; Biastoch et al., 2008; Rühs et al., 2015) and SST (e.g. Folland et al., 1986; Schlesinger and Ramankutty, 1994; Kushnir, 1994; Knight et al., 2005). Ridder and England (2014) explored in a model study that the variability of the oceanic oxygen distribution is associated with changes of surface wind stress in the tropics, which they linked to SST anomalies as well as changes in the ocean circulation and marine biology. Using meridional ship sections taken in the tropical North Atlantic between 28.5°W and 23°W, Brandt et al. (2010) contrasted oceanographic data taken during the period 1972

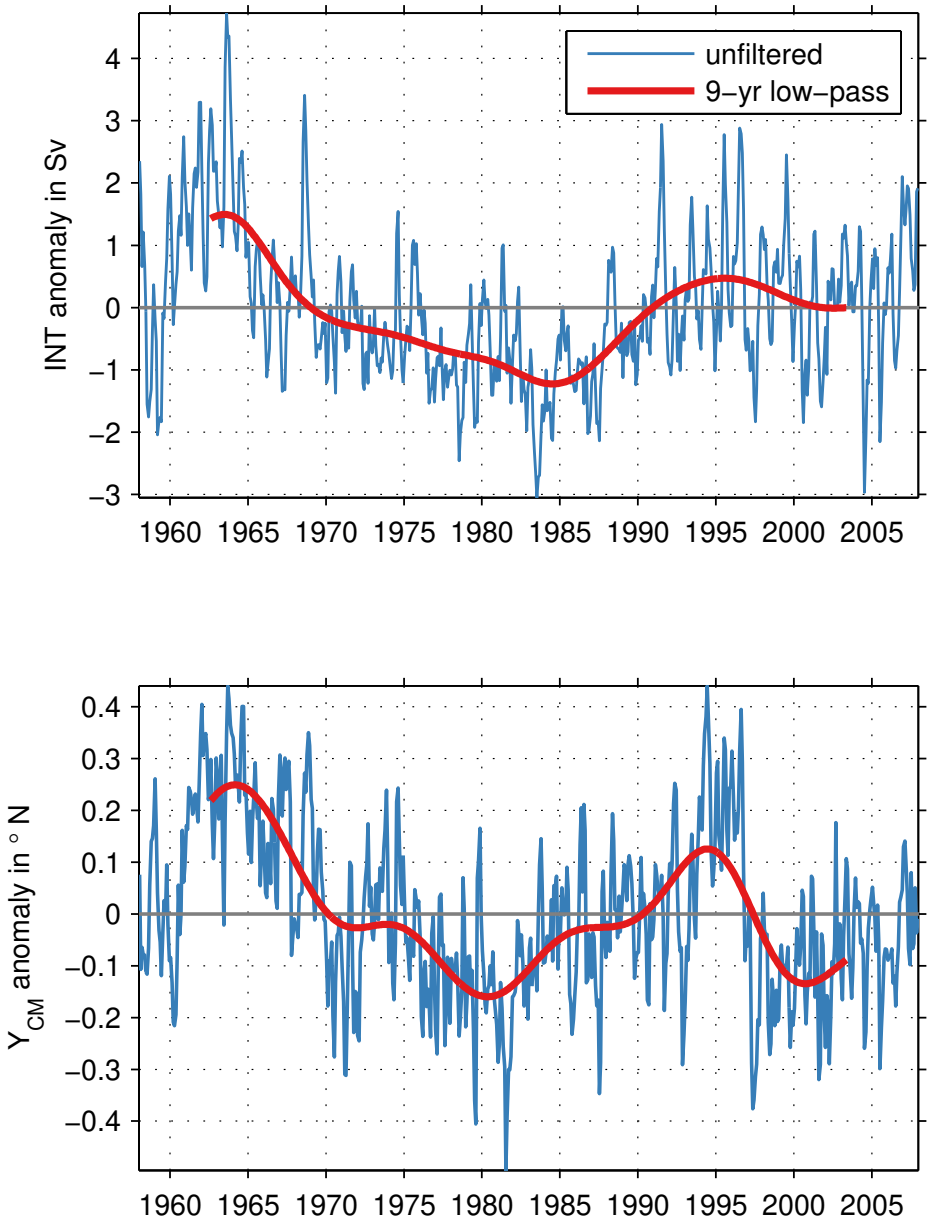

Figure 5.1: Zonal averaged (42-15°W) monthly mean NEUC Y_{CM} (Eq. 3.1) and INT (Eq. 3.2) anomaly with respect to the 1958-2007 seasonal cycle estimated from TRATL01 output (blue line). The red line shows the 9-yr low-pass filtered time series.

to 1985 and 1999 to 2008. In the core of the ETNA OMZ at about 400 m, they found stronger eastward and westward flows associated with higher oxygen concentrations between 4°N and 8°N for the earlier period and concluded, that changes in the zonal advection of oxygen may lead to changes of oxygen concentrations in the ETNA OMZ. In a more recent study, Hahn et al. (2017) observed a decrease of oxygen concentration in the upper ETNA OMZ (200-400 m) from 2006 to 2015 which the authors also link to changes in the zonal advection of oxygen.

In this chapter, the decadal to multidecadal variability of the NEUC and its relation to oxygen is analyzed based on the output of TRATL01 and the conceptual model used in chapter 3. In section 3.3.3, a decadal to multidecadal variability of the NEUC transport and core is evident in TRATL01 (Fig 5.1). In this chapter, potential drivers of this long-term variability of the NEUC, for example changes in the large scale wind field or the AMOC, are investigated in TRATL01. Unfortunately the multidedacal variability of oxygen within the NEUC region in TRATL01 can not be analyzed as the simulated oxygen concentrations drift (see section 3.2.2). Therefore, experiments based on the conceptual model used in chapter 3 are performed to investigate the impact of a decadal to multidecadal variability of the NEUC on the eastward advection of oxygen.

5.2 Data and Methods

For the analysis, the output of a global ocean circulation model TRATL01 is used, in wich a 1/10° nest covering the tropical Atlantic from 30°S to 30°N is embedded into a global 1/2° model (Duteil et al., 2014). For a more detailed description of TRATL01 see chapter 3.2.2.

Furthermore, a conceptual model is used to investigate the impact of NEUC variability on the oxygen distribution on decadal to multidecadal time scales. It is based on the advection-diffusion model described in Brandt et al. (2010) which simulates an eastward current and its westward return flows with an oxygen source at the western boundary (see section 3.2.4 for a detailed description). The experiments in this chapter are described in section 5.3.2. They are based on the simulation SIM 1 of the conceptual model (Eq. 3.3) with the horizontal eddy diffusivities $k_x = k_y = 800\,\mathrm{m^2\,s^{-1}}$ and the background flow field given by Eq. 3.4 with $u_0 = 0.055\,\mathrm{m\,s^{-1}}$. Note that this simulation of the conceptual model is closest to the observations and hence does not include a recirculation between the nSEC and the NEUC.

5.3 Results

In this section the decadal to multidecadal variability of the NEUC in TRATL01 and its potential impact on the oceanic oxygen distribution simulated with the conceptual model is investigated. First, the results of the NEUC variability in TRATL01 are presented. Afterwards, the experiments of the conceptual model are described and analyzed.

5.3.1 Multidecadal variability NEUC

In chapter 3, the NEUC transport INT (Eq. 3.2) and central position Y_{CM} (Eq. 3.1) of the NEUC core are calculated. Both time series exhibit seasonal to multidecadal variability. While chapter 3 investigates the seasonal to interannual variability of the NEUC, this chapter focusses on the decadal to multidecadal time scales (Fig. 5.1). Therefore, a 9-yr low-pass Butterworth filter order 4 is applied to the zonally averaged INT and Y_{CM} time series. For the low pass filtered time series, a significant positive correlation of $R = 0.72$ between NEUC transport and central position is found. The NEUC is stronger and displaced towards the north during the 1960s and 1990s, and it is weaker and more southward positioned between 1970 and 1990. On interannual time scales, the NEUC strength is associated with changes of the wind-field in the tropical Atlantic (Fig. 3.5). To investigate a possible relation of the NEUC and the wind-field on decadal to multidecadal time scales, a linear regression of the low-pass filtered NEUC INT onto the wind stress curl is performed and the anomalous Sverdrup streamfunction from the derived slope b times a unit transport of 1 Sv is calculated (Fig. 5.2). Maximum explained variance ($R = 0.9$) is found at 0 lag. For strong NEUC flow, a positive wind stress curl anomaly exists north and a negative wind stress curl anomaly exists south of about 4°N. This results in an anomalous Sverdrup streamfunction which is associated with eastward flow anomalies at about 5°N. Comparing the slope of the linear regression to the mean wind stress curl in TRATL01 averaged from 1958 to 2007, a meridional shift of the large-scale wind field is indicated.

The results of this section suggest, that the NEUC variability on decadal to multidecadal time scales is associated with changes of the large-scale wind field in the tropical Atlantic. Furthermore, the closure of the anomalous Sverdrup streamfunction suggests an anomalous northward transport at the western boundary across the equator during strong NEUC flow. This may lead to a better ventilation of the western boundary through the NBC. To investigate how a stronger NEUC flow or higher oxygen concentrations at the western boundary impacts the zonal distribution of oxygen on

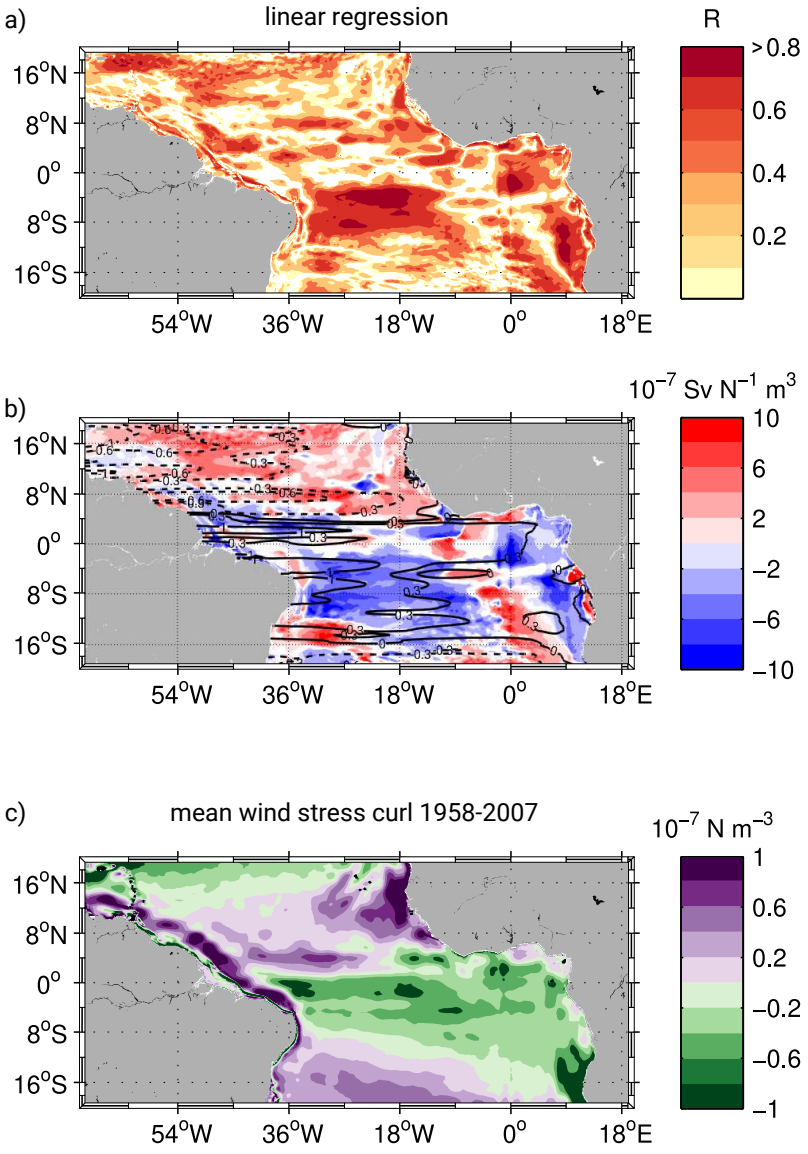

Figure 5.2: (a) Coefficient of correlation R and (b) slope of the linear regression of 9-years low-pass filtered NEUC INT onto wind stress curl. Contours in b) present the anomalous Sverdrup circulation forced by a wind stress curl anomaly that causes a NEUC transport anomaly of 1 Sv. The black solid lines mark the 0 Sv, 0.3 Sv and 1 Sv isoline and the black dashed lines mark the -0.3 Sv, -0.6 Sv and -1 Sv isoline. (c) Mean wind stress curl for the period 1958 to 2007 in TRATL01.

decadal to multidecadal time scales, different experiments with the conceptual model are performed which are presented in the next section.

5.3.2 Conceptual model

The conceptual model is used to investigate the potential impact of the decadal to multidecadal NEUC variability on the oxygen distribution in the tropical North Atlantic. Based on the reference experiment SIM 1, four experiments (VAR 1 decadal, VAR 1 multidecadal, VAR 3 decadal, VAR 3 multidecadal) are performed with the conceptual model. The oxygen response for the following scenarios are calculated: (i) A change of the mean NEUC strength that is associated with enhanced ventilation from the western boundary varying on decadal (i.e. 10 years; VAR 1 decadal) or multidecadal (i.e. 30 years; VAR 1 multidecadal) time scales. (ii) An oxygen variability of the source waters at the western boundary on decadal (VAR 3 decadal) or multidecadal (VAR 3 multidecadal) time scales which is then advected by the unchanged NEUC towards the east (Table 5.1).

Table 5.1: Overview over the decadal to multidecadal variability simulations performed with the conceptual model (Eq. 3.3).

simulation	flow field	velocity amplitude	O_2 at 45°W	period
SIM 1	Eq. 3.4	$u_0 = 0.055\,\mathrm{m\,s^{-1}}$	$C_0 = 147\mu\mathrm{mol\,kg^{-1}}$	
VAR 1 decadal	Eq. 3.4	$u_0 = 0.055\,\mathrm{m\,s^{-1}}+$ $0.04\,\mathrm{m\,s^{-1}} \cdot sin(t)$	$C_0 = 147\mu\mathrm{mol\,kg^{-1}}$	10 years
VAR 1 multidecadal	Eq. 3.4	$u_0 = 0.055\,\mathrm{m\,s^{-1}}+$ $0.04\,\mathrm{m\,s^{-1}} \cdot sin(t)$	$C_0 = 147\mu\mathrm{mol\,kg^{-1}}$	30 years
VAR 3 decadal	Eq. 3.4	$u_0 = 0.055\,\mathrm{m\,s^{-1}}$	$C_0 = 147\mu\mathrm{mol\,kg^{-1}}+$ $4\,\mu\mathrm{mol\,kg^{-1}} \cdot sin(t)$	10 years
VAR 3 multidecadal	Eq. 3.4	$u_0 = 0.055\,\mathrm{m\,s^{-1}}$	$C_0 = 147\mu\mathrm{mol\,kg^{-1}}+$ $4\,\mu\mathrm{mol\,kg^{-1}} \cdot sin(t)$	30 years

In the following, four time varying experiments performed with the conceptual model are discussed. The time variability is simulated by a simple sinusoid $A \cdot sin(t)$, where A is the amplitude and t is the time. The period of the sinusoid in the different experiments is given in Table 5.1.

VAR 1: Experiments VAR 1 decadal/multidecadal are based on SIM 1 (Eq. 3.3 combined with flow field defined by Eq. 3.4, no recirculation) and simulate oxy-

gen changes associated with a time varying mean flow on decadal/multidecadal time scales. Here, a sinusoid with $A = 0.04\,\mathrm{m\,s^{-1}}$ and a period of 10/30 years is superimposed on the velocity amplitude of the background flow field ($u_0 = 0.055\,\mathrm{m\,s^{-1}} + 0.04\,\mathrm{m\,s^{-1}} \cdot sin(t)$ in Eq. 3.4, Fig. 5.3a and 5.4a).

VAR 3: Experiments VAR 3 decadal/multidecadal are designed to study oxygen changes associated with time varying oxygen concentrations at the western boundary on decadal/multidecadal time scales. VAR 3 decadal/multidecadal are based on SIM 1 (Eq. 3.3 combined with flow field defined by Eq. 3.4, no recirculation). Here, a sinusoid with $A = 4\,\mu\mathrm{mol\,kg^{-1}}$ and a period of 10/30 years is superimposed on the oxygen source at the western boundary ($C_0 = 147\mu\mathrm{mol\,kg^{-1}} + 4\,\mu\mathrm{mol\,kg^{-1}} \cdot sin(t)$) while the velocity field is in steady state ($u_0 = 0.055\,\mathrm{m\,s^{-1}}$ in Eq. 3.4; Fig. 5.3b and 5.4b). Please note, that VAR 3 decadal/multidecadal simulations are also performed with higher amplitudes of oxygen variability at the western boundary.

To analyze the results of the time varying experiments, the horizontal distribution and magnitude of the simulated oxygen amplitude (oxygen maximum minus oxygen minimum, Fig. 5.3c,d and 5.4c,d) during one period of variability is investigated. The oxygen amplitude shows where maximum variability occurs in the basin. Additionally the phase of the simulated oxygen maximum is estimated (Fig. 5.3e,f and 5.4e,f). The phase of the oxygen maximum is defined as the time lag between the time of maximum amplitude of the forcing term (Fig. 5.3a,b and 5.4a,b) and the time of maximum simulated oxygen concentrations.

The structure of the maximum oxygen amplitude and its phase are quite similar between the same group of experiments (VAR 1 or VAR3) on decadal (Fig. 5.3) and multidecadal (Fig. 5.4) time scales. For the VAR 1 decadal/multidecadal experiments, the maximum oxygen concentrations occur along the eastward flow in the center of the basin after one to two years after maximum velocities occur (Fig. 5.3a,c,e and 5.4a,c,e), which is in general agreement with the experiments on interannual time scales (3 years, Fig. 3.11a,d,g). However, in contrast to the VAR 1 that varies on interannual time scale, the oxygen concentrations within the westward currents are not out of phase with the oxygen concentrations in the eastward current. In VAR 1 decadal/multidecadal, the oxygen concentrations in the westward flow regions reach their maximum in the central basin three to four years after maximum velocities. East of 15°W, the oxygen amplitude is weak (below $1\,\mu\mathrm{mol\,kg^{-1}}$). This is mainly due to the design of the flow field that has zero flow across the northern, southern and eastern boundary. As discussed in section 3.2.4, NEUC waters can exit the model domain towards all model boundaries in reality

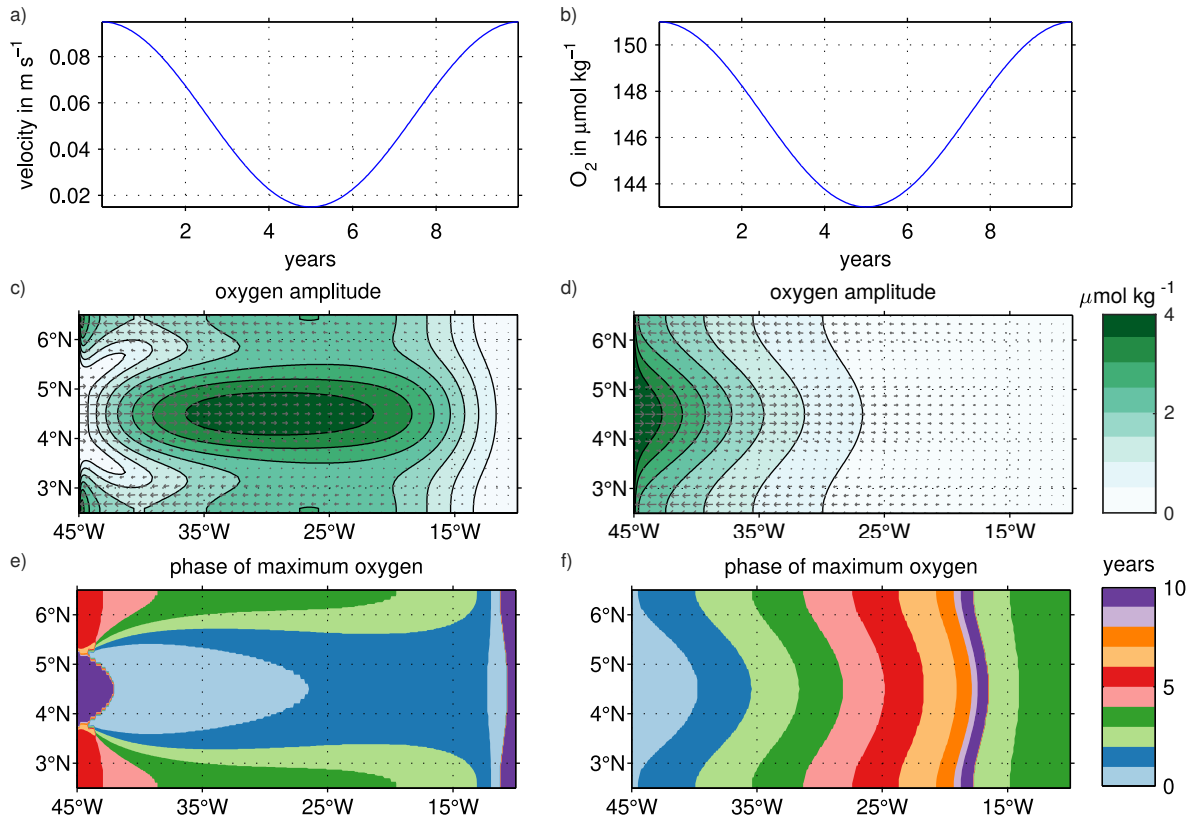

Figure 5.3: Results of VAR 1 decadal and VAR 3 decadal. (a,b) Amplitude of the time varying forcing, (c,d) distribution of oxygen amplitude (shading) and (e,f) distribution of phase of oxygen maximum simulated with the idealized experiments: (a,c,e) time varying background flow field and (b,d,f) time varying oxygen at 45°W . Gray arrows (c,d) show the mean horizontal flow field.

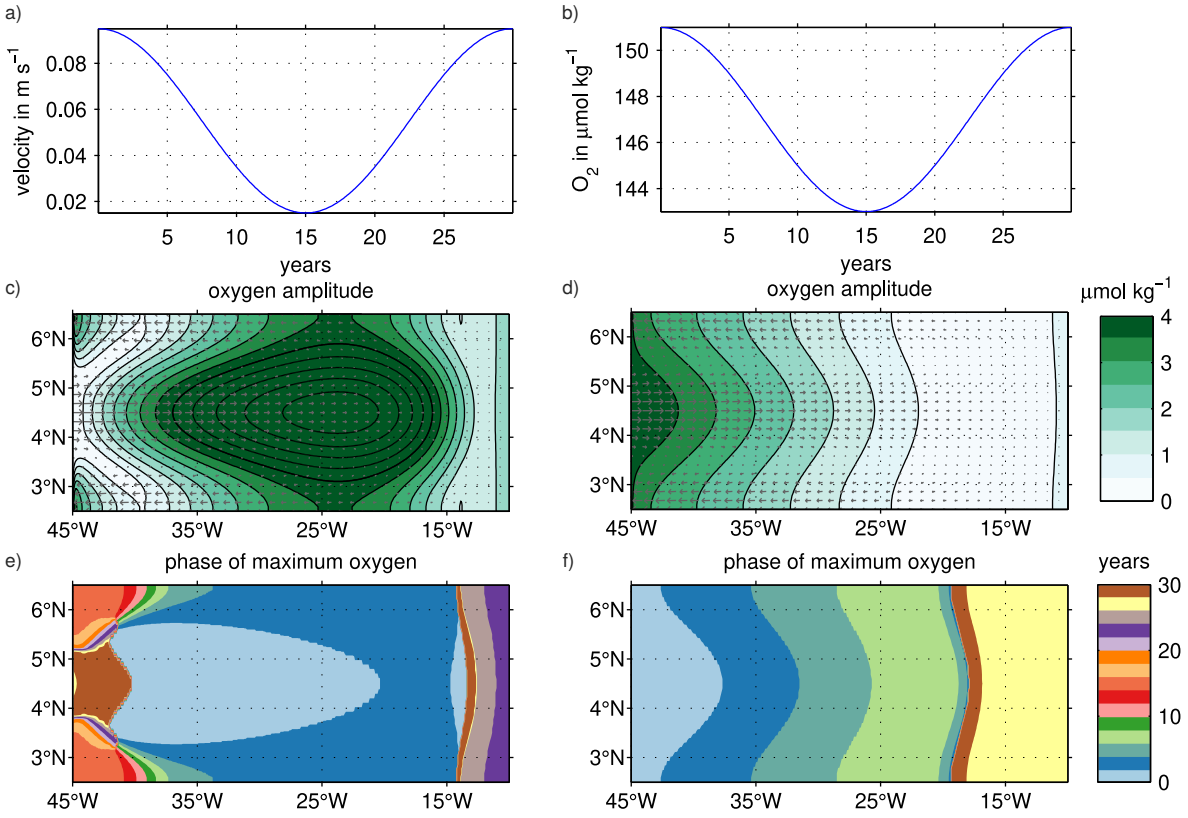

Figure 5.4: Results of VAR 1 multidecadal and VAR 3 multidecadal. (a,b) Amplitude of the time varying forcing, (c,d) distribution of oxygen amplitude (shading) and (e,f) distribution of phase of oxygen maximum simulated with the idealized experiments: (a,c,e) time varying background flow field and (b,d,f) time varying oxygen at 45°W . Gray arrows (c,d) show the mean horizontal flow field. The interval of black contours in c) is 0.5 μmol kg^{-1}, maximum values are between 6.5 μmol kg^{-1} and 7.0 μmol kg^{-1}.

and in TRATL01 in contrast to the design of the conceptunal model having closed boundaries.

In VAR 3 decadal/multidecadal, it takes about eight years to advect the oxygen anomaly from the western boundary as far east as 20°W (Fig. 5.3b,d,f and 5.4b,d,f). However, the oxygen anomaly is already dissipated during that time. Note that in VAR 3 decadal/multidecadal, a sudden phase shift occurs east of 20°W. Even if the oxygen amplitude at the western basin is increased, the oxygen amplitude does not change here similar to a node point of a standing wave. This is probably an artifact of the chosen basin geometry which limits the suitability of the conceptual model to investigate how changes in the source waters at the western boundary are advected within the NEUC towards the east on decadal to multidecadal time scales.

5.4 Summary and Discussion

In this chapter the sources of the decadal to multidecadal variability of the NEUC and its impact on the oxygen distribution in the ETNA are investigated based on the output of TRATL01 and experiments with a conceptual model, the latter simulating an eastward current and its westward return flows with an oxygen source at the western boundary (Brandt et al., 2010).

In TRATL01 the variability of the NEUC of about ± 1 Sv on decadal to multidecadal time scales is attributed to changes of the large-scale wind field in the tropical Atlantic. A stronger and more northward positioned NEUC is associated with a positive wind stress curl anomaly north of 4°N and a negative wind stress anomaly south of 4°N. This is associated with an anomalous Sverdrup function inducing anomalous eastward flow along the latitude of the NEUC. The closure of the anomalous Sverdrup function indicates anomalous northward flow across the equator at the western boundary during strong NEUC flow. This is in agreement with the model study of Rühs et al. (2015). They investigated the connection of the variability between the NBC and the AMOC using a model configuration similar to the global 1/2° host model in TRATL01. In their experiments, the NBC strengthens during the same periods when the NEUC is strengthening in TRATL01. Rühs et al. (2015) found the multidecadal variability of the NBC dominated by changes in the wind-driven circulation. Furthermore, they found that in the model, the large-scale wind field and the AMOC co-vary on decadal to multidecadal time scales. I.e., changes in the AMOC may impact the STCs and hence also contribute to the multidecadal variability of the NEUC in TRATL01. Another process that may impact the circulation system on decadal to multidecadal time scales

is the AMV (Ridder and England, 2014). In TRATL01 though, the NEUC leads the AMOC transports and the AMV index by a couple of years indicating that changes in the wind-field drives NEUC variability on decadal to multidecadal time scales in TRATL01 (Fig. 5.5).

As discussed in chapter 3, the mean NEUC in TRATL01 is stronger than in observations, which is linked to a stronger than observed recirculation between the NEUC and the northern branch of the South Equatorial Current (nSEC) in TRATL01. Furthermore, TRATL01 is driven by CORE.v2 wind forcing that includes NCEP winds. The CORE forcing as well as the NCEP wind is known to exhibit spurious multidecadal wind variability (Hurrell and Trenberth, 1998; Fiorino, 2000; He et al., 2016). Consequently, the multidecadal signal of the wind forcing may be unrealistic. However, the variation of the large-scale wind pattern in TRATL01 indicates a meridional shift of the wind field which results in wind-induced zonal velocity changes directly within the NEUC region. Such a meridional shift of the large-scale wind pattern may also occur in observations. For example, Martín-Rey et al. (2018) suggest a meridional shift of the large-scale wind pattern in the tropical Atlantic associated with the AMV.

Experiments with the conceptual model suggest that a zonally coherent strengthening of the NEUC mean flow on decadal to multidecadal time scales can result in a better ventilation of the eastern basin. However, changes of the oxygen concentrations at the western boundary have a minor impact on oxygen concentrations in the east. Keeping in mind that a change of the NEUC transport has not been observed throughout the last decade, the results of TRATL01 and the conceptual model indicate that a change in the large-scale wind field on decadal to multidecadal time scales may lead to a NEUC transport variability and associated changes of the ventilation of the ETNA OMZ.

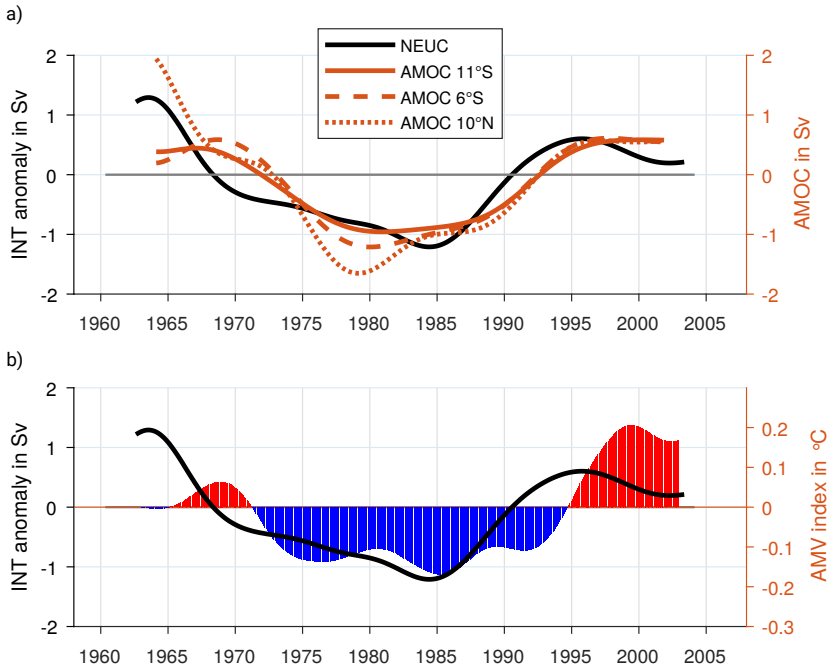

Figure 5.5: 9-years low-pass filtered NEUC *INT* anomaly (black line in a,b) with respect to the 1958-2007 seasonal cycle estimated from TRATL01 output.
(a) AMOC transport at 10°N (dotted brown line), 6°S (dashed brown line), and 11°S (solid brown line) derived according to (Rühs et al., 2015). First, the maximum zonally integrated streamfunction of meridional velocities below a depth of 500 m is estimated at each latitude. Afterwards, the time series is detrended and the temporal mean from 1958 to 2007 is removed. Then, a 139-months low-pass Butterworth filter order 4 is applied to the time series. The anomalous AMOC is shown at 10°N, 6°S and 11°S, where the temporal mean is 15.9±4.6 Sv, 15.4±3.7 Sv and 15.2±3.3 Sv, respectively.
(b) AMV index calculated according to Trenberth and Shea (2006). The calculation requires global averaged SST anomalies. Hence, the output of the global 1/2° host model is used for the calculation. Global SST anomalies are calculated with respect to the 1958-2007 climatology. Then, the SST anomalies are averaged at global scale (60°S-60°N) and in the entire North Atlantic basin (0°-80°W, 0°-60°N). The global averaged SST anomalies are then subtracted from the SST anomalies averaged in the North Atlantic basin. Finally, a 121-months low-pass Butterworth filter order 2 is applied to the time series.

6 Synthesis

In this thesis the role of intraseasonal to multidecadal NEUC variability for the oxygen supply towards the Eastern Tropical North Atlantic is investigated. The analysis is based on multiyear moored and shipboard observations and the output of an OGCM as well as experiments with a conceptual model simulating an eastward current and its westward return flows with an oxygen source at the western boundary. For the first time the NEUC transport is reconstructed from direct velocity observations providing new insights about its mean flow and its variability. Both, observations and model output suggest that, on intraseasonal to interannual time scales, a stronger NEUC is not necessarily associated with a higher oxygen supply of the eastern basin. Experiments with the conceptual model suggest, that a strengthening of the NEUC transport on decadal to multidecadal time scales results in a better ventilation of eastern basin. However, in this thesis no observational evidence for a change of the NEUC transports on decadal to multidecadal time scales is found. A general issue emphasized in this thesis is the problem of state-of-the-art OGCMs to realistically simulate off-equatorial current bands such as the NEUC. This results in an erroneous simulation of the current variability and tracer distribution which was already shown by Duteil et al. (2014). Unresolved transport processes are one of the key factors why state-of-the-art models may underestimate the oceanic deoxygenation (Oschlies et al., 2018). The new findings of this thesis about the NEUC, its variability and its role for the oxygen supply of the ETNA provides new possibilities for model validation.

6.1 Progress on research questions and its integration in the current state of research

The NEUC is an eastward flowing current centered at about 5°N in the tropical Atlantic. Although its core velocity is weak (below $0.3\,\mathrm{m\,s^{-1}}$) it is thought to act as important oxygen supply route towards the ETNA OMZ (Brandt et al., 2010, 2015; Hahn et al., 2017; Stramma et al., 2008a). Hahn et al. (2017) suggest that oxygen

trends in the upper ETNA OMZ (200-400 m) from 2006 to 2015 are linked to changes in the zonal advection of oxygen. This motivated the following research question of this thesis: What is the role of the NEUC variability for changes in the oxygen supply of the ETNA OMZ? However, the variability of the NEUC is not well understood as shipboard observations are obscured by mesoscale (Weisberg and Weingartner, 1988) or interannual variability (Hüttl-Kabus and Böning, 2008; Goes et al., 2013) and models have problems to realistically simulate currents like the NEUC (Duteil et al., 2014). Hence, two further research questions arose: What are the dominant time scales of NEUC variability and what are potential drivers of it? In the following the progress on the research questions and its integration in the current state of research is presented.

What are the dominant time scales of NEUC variability?

In this thesis, the NEUC transport was reconstructed from direct velocity observations (Jun 2006-Feb 2008, Nov 2009-Jan 2018) for the first time. This provides a more comprehensive view about the NEUC variability compared to previous observational and model studies. Hüttl-Kabus and Böning (2008) studied the NEUC in a high resolution (1/12°) OGCM. In their model the NEUC at 23°W is dominated by the seasonal cycle with an amplitude of about 3 Sv. They found that the interannual variability of the NEUC was phase locked to the seasonal cycle with a comparable amplitude (2 Sv). Goes et al. (2013) studied the seasonal to interannual variability of the NEUC. They derived the NEUC velocity, transport and core position at about 25°W by combining high-density expendable bathythermograph (XBT) temperature data with altimetric Sea Level Height Anomalys (SLAs). They found an annual cycle of the NEUC of about 1.0 to 2.5 Sv, which is dominating the transport time series over the semi-annual cycle. However, Goes et al. (2013) also note, that the relative low-percent variance of the annual harmonic (35%) suggests, that the NEUC is strongly modulated by mesoscale or interannual variability. The NEUC transport in the high resolution (1/10°) OGCM called TRATL01, that is used in this thesis (chapter 3 and 5), is also dominated by a seasonal cycle with an amplitude of 3.5 Sv at 23°W. In TRATL01, the interannual variability of the NEUC is also phase locked to its seasonal cycle with an amplitude of about 1 Sv. Furthermore, a decadal to multidecadal NEUC transport variability with an amplitude of about 1 Sv is found in TRATL01 (chapter 5). In contrast to the above mentioned studies, neither the multiyear velocity observations at 5°N, 23°W nor the reconstructed NEUC transport time series show a pronounced seasonal cycle or indications for an interannual to multidecadal variability (chapter 4). Both, moored velocity observations and reconstructed NEUC transport time series are dominated by intrasea-

sonal eastward events peaking without a clear seasonal preference. The eastward flow events last for about two to five months. The new insights about the NEUC variability obtained from direct velocity observations demonstrate that state-of-the-art OGCMs are not able to realistically simulate the NEUC. They also demonstrate, that temporal high-resolution observations are needed to capture the true variability of the NEUC. The direct velocity observations provides a completely new picture of NEUC variability and rises new questions about its potential driving processes, which will be discussed in the following.

What are potential drivers of NEUC variability?

This thesis discussed different processes which may contribute to the NEUC variability. In this paragraph, first potential mechanisms for the seasonal variability of zonal velocities at 5°N, 23°W will be considered before potential driving mechanism for the intraseasonal eastward flow events will be presented.

The dominance of intraseasonal variability in the reconstructed NEUC transport time series suggest that potential driving mechanism of the NEUC exhibiting a distinct seasonal variability themselves may not be of first order in forcing the observed NEUC variability. For example, McCreary et al. (2002) and Furue et al. (2007, 2009) suggested that the upwelling within the Guinea Dome may drive the NEUC. However, the Guinea dome upwelling exhibits a clear seasonal variability (Siedler et al., 1992; Stramma et al., 2005) and other observational and model studies do not find a distinct link between NEUC transports and the upwelling in the Guinea dome (Bourlès et al., 2002; Elmoussaoui et al., 2005; Hüttl-Kabus and Böning, 2008). Jochum and Malanotte-Rizzoli (2004) suggest that TIWs may impact the NEUC transport. However, TIWs along 5°N mainly occur during late boreal summer (Athie and Marin, 2008) leaving the observed semi-annual cycle of the zonal velocities within the NEUC region unexplained. This thesis investigated a new mechanism that may drive the annual and semi-annual cycle of the zonal velocities within the NEUC region. Section 4.9 investigated the role of resonant equatorial basin modes for the wind-driven seasonal variability of the zonal velocities at 5°N, 23°W using a shallow water model. The first five baroclinic modes of the gravest basin mode are able to realistically simulate the semi-annual cycle of zonal velocity, which dominates the seasonal variability over the annual cycle for the upper 100 m. The shallow water model simulations for the first five baroclinic modes fail to represent the observed annual cycle of the zonal velocities at 5°N, 23°W. However, the results indicate that the fourth baroclinic mode may contribute to it. This is in agreement with previous studies in the equatorial Atlantic which found that the

semiannual and annual variability of the zonal flow is attributed to the resonance period of the gravest basin mode for the second and the forth baroclinic modes, respectively (Thierry et al., 2004; Ding et al., 2009; Brandt et al., 2016).

Please note, that the upper part of the NEUC and the lower part of the NECC ar difficult to separate during most of the year, especially during boreal summer and fall (Bourlès et al., 1999b, 2002; Schott et al., 2003; Brandt et al., 2006; Urbano et al., 2008; Hüttl-Kabus and Böning, 2008; Jochum and Malanotte-Rizzoli, 2004). However, the NECC is directly wind-driven and its variability is dominated by the annual cycle with minimum transports during boreal spring and maximum transport during boreal summer and fall (Fonseca et al., 2004; Goes et al., 2013). Hence, the transports of NEUC and the NECC are dominated by variability on different time scales. This indicates that the here chosen upper limit of the NEUC provides a reasonable separation between the NEUC and NECC.

As mentioned above, the zonal velocities and the reconstructed NEUC transport time series at 5°N, 23°W are dominated by intraseasonal eastward flow events. With mean eastward velocities below $8\,\mathrm{cm\,s^{-1}}$ the NEUC appears as a weak current. Strong eastward transport events can generally be caused by different mechanisms triggering Rossby waves that alter the weak mean flow. Along that latitude, Rossby waves can be forced by a localized wind forcing or remotely generated by reflection of equatorial Kelvin waves at the eastern boundary as well as coastally trapped waves generated in the Gulf of Guinea. Chapter 4 indicates a relationship between the reconstructed NEUC transport time series and anomalous wind stress curl off the coast of Liberia. Furthermore, the eastward flow events coincides with equatorial upwelling Kelvin waves. However, a direct link between one of these processes and the intraseasonal eastward events could not be shown and further investigations are needed. Strikingly, previous studies (Hüttl-Kabus and Böning, 2008; Goes et al., 2013) did not explore a dominance of intraseasonal eastward events in the NEUC transport time series. In the study of Goes et al. (2013), the low temporal resolution of the used High-Density Expendable Bathythermograph (XBT) profiles may be one reason, why they could not observed the intraseasonal eastward flow events. A possible explanation why model studies do not simulate the intraseasonal eastward events may be that they overestimate the mean NEUC flow. A strong eastward current could meridionally deflect a Rossby wave towards a latitude of weak velocities as shown in a ray tracing experiment by Claus et al. (2014). Furthermore, in this thesis, the variability of the NEUC in TRATL01 is linked to variations of the large-scale wind-field whereas the observations suggest that localized wind stress curl anomalies may drive changes in the NEUC. This indicates

the importance of the spatial resolution of wind-stress forcing for a realistic simulation of NEUC variability. In the OGCM used in this thesis, the relative coarse horizontal resolution (2°) of the wind-forcing (COREv2) may simply not resolve local wind events which seem to be important drivers of the observed intraseasonal eastward flow events. For a better simulation of the NEUC and its variability, a promising approach is to increase the horizontal and temporal resolution of the wind forcing as done in the new JRA55-do surface data set (Tsujino et al., 2018).

What is the role of the NEUC variability for changes in the oxygen supply of the ETNA OMZ?

Both, the results of TRATL01 and observations suggest that the NEUC is not permanently connected to the western boundary. One of the main findings of the analysis of TRATL01 (chapter 3) is that the eastward oxygen supply due to the NEUC depends on the source water pathways. For example, a strengthening of the NEUC supplied out of the western boundary is associated with higher oxygen concentrations within the NEUC, while a strengthening of the NEUC driven by a stronger recirculation within the ocean interior results in a reduction of oxygen concentrations within the NEUC. That the variability of the NEUC is not zonally coherent was already suggested by the model study of Hüttl-Kabus and Böning (2008). The observations analyzed in this thesis support these findings. For example, a strengthening of the NEUC associated with higher oxygen concentrations at 23°W is only occasionally observed (only for 2 events in 2017, chapter 4). Additionally, oxygen anomalies can also occur independently from intraseasonal eastward flow events (chapter 4). This suggests that oxygen-rich water masses at the western boundary are advected eastward in some kind of bursts or filaments within the NEUC. Until these bursts reach 23°W, the velocity field may be already altered by other processes like mesoscale recirculations (chapter 3). However, the ventilation bursts seems to play an important role for setting the mean oxygen concentrations within the NEUC.

In addition to the intraseasonal eastward flow events, this thesis investigated how a change of the NEUC transport on decadal to multidecadal time scales may impact the oxygen concentrations in the ETNA (chapter 5). Therefore experiments with the conceptual model are performed regarding variations of the NEUC transport as well as changes of oxygen concentrations at the western boundary. Oxygen anomalies at the western boundary are advected as far as 20°W within eight years and seem to be of minor importance for changes in the oxygen supply of the eastern basin. The results indicate that a decadal or multidecadal strengthening of the NEUC transport results

in a better ventilation of the eastern basin within four years after maximum eastward flow. However, moored observations did not show any evidence for a change of the NEUC strength throughout the last decade.

6.2 Outlook

The results of this thesis arise the question, whether the ventilation of the NEUC region is set by eastward current bursts or by a mean eastward current as suggested in previous studies (Brandt et al., 2010; Stramma et al., 2008a; Hahn et al., 2014; Brandt et al., 2015; Hahn et al., 2017). This question aligns with a more general issue emphasized in this thesis; that is the connection of the zonal current system in the tropical Atlantic to the western boundary. As shown in this thesis, the supply pathways of eastward currents such as the NEUC play a key role for the zonal distribution of water masses in the tropical Atlantic (chapter 3,4). One possible supply pathway consists of the western boundary currents, which are thought to feed the eastward currents (Bourlès et al., 1999a; Hüttl-Kabus and Böning, 2008; Rosell-Fieschi et al., 2015; Stramma et al., 2005). The second water mass supply for the eastward currents are recirculations between the eastward currents and the westward flowing branches of the SEC (Fischer et al., 2008; Hüttl-Kabus and Böning, 2008; Jochum and Malanotte-Rizzoli, 2004). These recirculations can be directly wind or buoyancy driven or occur due to the passage of Tropical Instability Waves (TIWs) (chapter 3). However, the relative importance of the two different supply pathways for the eastward currents is still unclear. While observational studies suggest the supply via the western boundary to be of major importance (Brandt et al., 2015, 2010; Fischer et al., 2008; Stramma et al., 2008a), model studies favor the supply via the recirculations within the ocean interior (Hüttl-Kabus and Böning, 2008; Jochum et al., 2004).

The results of this thesis reveal the necessity to improve the understanding of the supply pathways of the eastward currents in the tropical Atlantic. Therefore both, improved model simulations as well as new observational data, are needed. Preliminary results of new OGCM simulations forced with the JRA55-do sea surface dataset (Tsujino et al., 2018) show a clearly improved representation of the tropical Atlantic current system compared to previous OGCM simulations. These model simulations might provide a more realistic picture about the role of eastward currents in ventilating the eastern tropical Atlantic. New insights may also be obtained by additional moored and shipboard velocity and oxygen observations close to the western boundary. As shown in this thesis, temporally high-resolution measurements are necessary to capture

the variability of weak currents such as the NEUC. Extending the PIRATA moorings along 38°W with oxygen sensors and ADCPs observing the upper 800 m plus deploying three additional moorings at for example 35°W, 5°S as well as 38°W, 6°N and 10°N would be of great value to investigate the role of oxygen and current variability at the western boundary in driving ventilation variability of the eastern tropical Atlantic and to unravel missing transport processes in state-of-the-art OGCMs.

Bibliography

Arévalo-Martínez, D. L., Kock, A., Löscher, C. R., Schmitz, R. A., and Bange, H. W. (2015). Massive nitrous oxide emissions from the tropical South Pacific Ocean. *Nat. Geosci.*, 8(7):530–533.

Artamonov, Y. V. (2006). Seasonal variability of geostrophic currents in the Atlantic Ocean according to the altimetry data. *Phys. Oceanogr.*, 16(3):177–187.

Ascani, F., Firing, E., Dutrieux, P., McCreary, J. P., and Ishida, A. (2010). Deep Equatorial Ocean Circulation Induced by a Forced–Dissipated Yanai Beam*. *J. Phys. Oceanogr.*, 40(5):1118–1142.

Ascani, F., Wang, D., and Firing, E. (2006). Equatorial deep jets in a simple ocean generation circulation model. In *Eos, Trans. Amer. Geophys. Union*, pages 87, Abstract OS33C–05 (Ocean Sciences Meeting Supp.

Athie, G. and Marin, F. (2008). Cross-equatorial structure and temporal modulation of intraseasonal variability at the surface of the Tropical Atlantic Ocean. *J. Geophys. Res. Ocean.*, 113(C8):1–17.

Ba, J., Keenlyside, N. S., Park, W., Latif, M., Hawkins, E., and Ding, H. (2013). A mechanism for Atlantic multidecadal variability in the Kiel Climate Model. *Clim. Dyn.*, 41(7-8):2133–2144.

Banyte, D., Tanhua, T., Visbeck, M., Wallace, D. W., Karstensen, J., Krahmann, G., Schneider, A., Stramma, L., and Dengler, M. (2012). Diapycnal diffusivity at the upper boundary of the tropical North Atlantic oxygen minimum zone. *J. Geophys. Res. Ocean.*, 117(C9):1–14.

Bentamy, A. and Fillon, D. C. (2012). Gridded surface wind fields from Metop/ASCAT measurements. *Int. J. Remote Sens.*, 33(6):1729–1754.

Biastoch, A., Böning, C. W., and Lutjeharms, J. R. E. (2008). Agulhas leakage dynamics affects decadal variability in Atlantic overturning circulation. *Nature*, 456(7221):489–492.

Bjerknes, J. (1969). Atmospheric Teleconnections From the Equatorial Pacific 1. *Mon. Weather Rev.*, 97(3):163–172.

Böning, C. W. and Kröger, J. (2005). Seasonal variability of deep currents in the equatorial Atlantic: a model study. *Deep Sea Res. Part I Oceanogr. Res. Pap.*, 52(1):99–121.

Böning, C. W., Scheinert, M., Dengg, J., Biastoch, A., and Funk, A. (2006). Decadal variability of subpolar gyre transport and its reverberation in the North Atlantic overturning. *Geophys. Res. Lett.*, 33(21):L21S01.

Booth, B. B., Dunstone, N. J., Halloran, P. R., Andrews, T., and Bellouin, N. (2012). Aerosols implicated as a prime driver of twentieth-century North Atlantic climate variability. *Nature*, 484(7393):228–232.

Bourlès, B., D'Orgeville, M., Eldin, G., Gouriou, Y., Chuchla, R., DuPenhoat, Y., and Arnault, S. (2002). On the evolution of the thermocline and subthermocline eastward currents in the Equatorial Atlantic. *Geophys. Res. Lett.*, 29(16):32–1–32–4.

Bourlès, B., Gouriou, Y., and Chuchla, R. (1999a). On the circulation in the upper layer of the western equatorial Atlantic. *J. Geophys. Res. Ocean.*, 104(C9):21151–21170.

Bourlès, B., Molinari, R. L., Johns, E., Wilson, W. D., and Leaman, K. D. (1999b). Upper layer currents in the western tropical North Atlantic (1989-1991). *J. Geophys. Res. Ocean.*, 104(C1):1361–1375.

Brandt, P., Bange, H. W., Banyte, D., Dengler, M., Didwischus, S.-H., Fischer, T., Greatbatch, R. J., Hahn, J., Kanzow, T., Karstensen, J., Körtzinger, A., Krahmann, G., Schmidtko, S., Stramma, L., Tanhua, T., and Visbeck, M. (2015). On the role of circulation and mixing in the ventilation of oxygen minimum zones with a focus on the eastern tropical North Atlantic. *Biogeosciences*, 12(2):489–512.

Brandt, P., Caniaux, G., Bourlès, B., Lazar, A., Dengler, M., Funk, A., Hormann, V., Giordani, H., and Marin, F. (2011). Equatorial upper-ocean dynamics and their interaction with the West African monsoon. *Atmos. Sci. Lett.*, 12(1):24–30.

Brandt, P., Claus, M., Greatbatch, R. J., Kopte, R., Toole, J. M., Johns, W. E., and Böning, C. W. (2016). Annual and Semiannual Cycle of Equatorial Atlantic Circulation Associated with Basin-Mode Resonance. *J. Phys. Oceanogr.*, 46(10):3011–3029.

Brandt, P. and Eden, C. (2005). Annual cycle and interannual variability of the mid-depth tropical Atlantic Ocean. *Deep. Res. Part I Oceanogr. Res. Pap.*, 52(2):199–219.

Brandt, P., Funk, A., Tantet, A., Johns, W. E., and Fischer, J. (2014). The Equatorial Undercurrent in the central Atlantic and its relation to tropical Atlantic variability. *Clim. Dyn.*, 43(11):2985–2997.

Brandt, P., Hormann, V., Körtzinger, A., Visbeck, M., Krahmann, G., Stramma, L., Lumpkin, R., and Schmid, C. (2010). Changes in the Ventilation of the Oxygen Minimum Zone of the Tropical North Atlantic. *J. Phys. Oceanogr.*, 40(8):1784–1801.

Brandt, P., Schott, F. A., Provost, C., Kartavtseff, A., Hormann, V., Bourlès, B., and Fischer, J. (2006). Circulation in the central equatorial Atlantic: Mean and intraseasonal to seasonal variability. *Geophys. Res. Lett.*, 33(7):1–4.

Brewer, P. G. and Peltzer, E. T. (2017). Depth perception: the need to report ocean biogeochemical rates as functions of temperature, not depth. *Philos. Trans. R. Soc. A Math. Phys. Eng. Sci.*, 375(2102):20160319.

Buckley, M. W., Ferreira, D., Campin, J.-M., Marshall, J., and Tulloch, R. (2012). On the Relationship between Decadal Buoyancy Anomalies and Variability of the Atlantic Meridional Overturning Circulation. *J. Clim.*, 25(23):8009–8030.

Buckley, M. W. and Marshall, J. (2015). Observations, inferences, and mechanisms of the Atlantic Meridional Overturning Circulation: A review. *Rev. Geophys.*, 54:5–63.

Bunge, L. and Clarke, A. J. (2009). Seasonal Propagation of Sea Level along the Equator in the Atlantic. *J. Phys. Oceanogr.*, 39(4):1069–1074.

Bunge, L., Provost, C., and Kartavtseff, A. (2007). Variability in horizontal current velocities in the central and eastern equatorial Atlantic in 2002. *J. Geophys. Res. Ocean.*, 112(C2):C02014.

Burmeister, K., Brandt, P., and Lübbecke, J. F. (2016). Revisiting the cause of the eastern equatorial Atlantic cold event in 2009. *J. Geophys. Res. Ocean.*, 121(7):4777–4789.

Burmeister, K., Lübbecke, J. F., Brandt, P., and Duteil, O. (2019). Interannual variability of the Atlantic North Equatorial Undercurrent and its impact on oxygen. *J. Geophys. Res. Ocean.*, pages 1–26.

Cabré, A., Marinov, I., Bernardello, R., and Bianchi, D. (2015). Oxygen minimum zones in the tropical Pacific across CMIP5 models: mean state differences and climate change trends. *Biogeosciences*, 12(18):5429–5454.

Cane, M. A. and Moore, D. W. (1981). A Note on Low-Frequency Equatorial Basin Modes. *J. Phys. Oceanogr.*, 11(11):1578–1584.

Carton, J. A., Cao, X., Giese, B. S., and Da Silva, A. M. (1996). Decadal and Interannual SST Variability in the Tropical Atlantic Ocean. *J. Phys. Oceanogr.*, 26(7):1165–1175.

Chang, P., Saravanan, R., Ji, L., and Hegerl, G. C. (2000). The Effect of Local Sea Surface Temperatures on Atmospheric Circulation over the Tropical Atlantic Sector. *J. Clim.*, 13(13):2195–2216.

Chang, P., Zhang, R., Hazeleger, W., Wen, C., Wan, X., Ji, L., Haarsma, R. J., Breugem, W. P., and Seidel, H. (2008). Oceanic link between abrupt changes in the north Atlantic ocean and the African monsoon. *Nat. Geosci.*, 1(7):444–448.

Claus, M., Greatbatch, R. J., and Brandt, P. (2014). Influence of the Barotropic Mean Flow on the Width and the Structure of the Atlantic Equatorial Deep Jets. *J. Phys. Oceanogr.*, 44(9):2485–2497.

Claus, M., Greatbatch, R. J., Brandt, P., and Toole, J. M. (2016). Forcing of the Atlantic Equatorial Deep Jets Derived from Observations. *J. Phys. Oceanogr.*, 46(12):3549–3562.

Cunningham, S. a., Kanzow, T., Rayner, D., Baringer, M. O., Johns, W. E., Marotzke, J., Longworth, H. R., Grant, E. M., Hirschi, J. J., Beal, L. M., Meinen, C. S., and Bryden, H. L. (2007). Temporal Variability of the. 317(August):935–938.

Cushman-Roisin, B. and Beckers, J. (2006). *Introduction to Geophysical Fluid Dynamics: Physical and Numerical Aspects*. Academic press.

Danabasoglu, G. (2008). On Multidecadal Variability of the Atlantic Meridional Overturning Circulation in the Community Climate System Model Version 3. *J. Clim.*, 21(21):5524–5544.

Delworth, T., Manabe, S., and Stouffer, R. J. (1993). Interdecadal Variations of the Thermohaline Circulation in a Coupled Ocean-Atmosphere Model. *J. Clim.*, 6(11):1993–2011.

Delworth, T. L. and Greatbatch, R. J. (2000). Multidecadal Thermohaline Circulation Variability Driven by Atmospheric Surface Flux Forcing. *J. Clim.*, 13(9):1481–1495.

Dietze, H. and Loeptien, U. (2013). Revisiting "nutrient trapping" in global coupled biogeochemical ocean circulation models. *Global Biogeochem. Cycles*, 27(2):265–284.

Ding, H., Keenlyside, N. S., and Latif, M. (2009). Seasonal cycle in the upper equatorial Atlantic Ocean. *J. Geophys. Res.*, 114(C9):C09016.

D'Orgeville, M., Hua, B. L., and Sasaki, H. (2007). Equatorial deep jets triggered by a large vertical scale variability within the western boundary layer. *J. Mar. Res.*, 65(1):1–25.

Duteil, O., Schwarzkopf, F. U., Böning, C. W., and Oschlies, A. (2014). Major role of the equatorial current system in setting oxygen levels in the eastern tropical Atlantic Ocean: A high-resolution model study. *Geophys. Res. Lett.*, 41:2033–2040.

Eden, C. and Willebrand, J. (2001). Mechanism of Interannual to Decadal Variability of the North Atlantic Circulation. *J. Clim.*, 14(10):2266–2280.

Ekman, V. W. (1905). *On the influence of the earth's rotation on ocean-currents.* Almqvist & Wiksells boktryckeri, A.-B.,.

Eliassen, A. and Palm, E. (1960). On the Transfer of Energy in the Electromagnetic Field. *Geofis. Puvlikasjoner Geophys. Nor.*, 22(3):343–361.

Elmoussaoui, A., Arhan, M., and Treguier, A. M. (2005). Model-inferred upper ocean circulation in the eastern tropics of the North Atlantic. *Deep. Res. Part I Oceanogr. Res. Pap.*, 52(7):1093–1120.

Enfield, D. B., Mestas-Nuñez, A. M., and Trimble, P. J. (2001). The Atlantic multidecadal oscillation and its relation to rainfall and river flows in the continental U.S. *Geophys. Res. Lett.*, 28(10):2077–2080.

Fiorino, M. (2000). The impact of the satellite observing system on low-fre- quency temperature variability in the ECMWF and NCEP reanalyses. In *Proc. Second WCRP Int. Conf. Reanalyses*, pages 65–68.

Fischer, J., Brandt, P., Dengler, M., Müller, M., and Symonds, D. (2003). Surveying the upper ocean with the ocean surveyor: A new phased array Doppler current profiler. *J. Atmos. Ocean. Technol.*, 20(5):742–751.

Fischer, J., Hormann, V., Brandt, P., Schott, F. A., Rabe, B., and Funk, A. (2008). South Equatorial Undercurrent in the western to central tropical Atlantic. *Geophys. Res. Lett.*, 35(21):1–5.

Fischer, T., Banyte, D., Brandt, P., Dengler, M., Krahmann, G., Tanhua, T., and Visbeck, M. (2013). Diapycnal oxygen supply to the tropical North Atlantic oxygen minimum zone. *Biogeosciences*, 10(7):5079–5093.

Folland, C. K., Palmer, T. N., and Parker, D. E. (1986). Sahel rainfall and worldwide sea temperatures, 1901-85. *Nature*, 320(6063):602–607.

Foltz, G. R. and McPhaden, M. J. (2008). Trends in Saharan dust and tropical Atlantic climate during 1980-2006. *Geophys. Res. Lett.*, 35(20):1–5.

Foltz, G. R. and McPhaden, M. J. (2010a). Abrupt equatorial wave-induced cooling of the Atlantic cold tongue in 2009. *Geophys. Res. Lett.*, 37(24):1–5.

Foltz, G. R. and McPhaden, M. J. (2010b). Interaction between the Atlantic meridional and Nio modes. *Geophys. Res. Lett.*, 37(18):1–5.

Fonseca, C. A., Goni, G. J., Johns, W. E., and Campos, E. J. D. (2004). Investigation of the North Brazil Current retroflection and North Equatorial Countercurrent variability. *Geophys. Res. Lett.*, 31(21):L21304.

Fratantoni, D. M., Johns, W. E., Townsend, T. L., and Hurlburt, H. E. (2000). Low-Latitude Circulation and Mass Transport Pathways in a Model of the Tropical Atlantic Ocean*. *J. Phys. Oceanogr.*, 30(8):1944–1966.

Furue, R., McCreary, J. P., Yu, Z., and Wang, D. (2007). Dynamics of the Southern Tsuchiya Jet*. *J. Phys. Ocean.*, 37(3):531–553.

Furue, R., McCreary Jr., J. P., and Yu, Z. (2009). Dynamics of the Northern Tsuchiya Jet*. *J. Phys. Oceanogr.*, 39(9):2024–2051.

Gill, A. E. (1982). *Atmosphere-Ocean Dynamics,*. Academic Press, San Diego.

Goes, M., Goni, G., Hormann, V., and Perez, R. C. (2013). Variability of the Atlantic off-equatorial eastward currents during 1993-2010 using a synthetic method. *J. Geophys. Res. Ocean.*, 118(6):3026–3045.

Gray, J. S., Wu, R., and Or, Y. (2002). Effects of hypoxia and organic enrichment on the coastal marine environment. *Mar. Ecol. Prog. Ser.*, 238:249–279.

Greatbatch, R. J., Brandt, P., Claus, M., Didwischus, S.-H., and Fu, Y. (2012). On the Width of the Equatorial Deep Jets. *J. Phys. Oceanogr.*, 42(10):1729–1740.

Griffies, S. M., Biastoch, A., Böning, C., Bryan, F., Danabasoglu, G., Chassignet, E. P., England, M. H., Gerdes, R., Haak, H., Hallberg, R. W., Hazeleger, W., Jungclaus, J., Large, W. G., Madec, G., Pirani, A., Samuels, B. L., Scheinert, M., Gupta, A. S., Severijns, C. A., Simmons, H. L., Treguier, A. M., Winton, M., Yeager, S., and Yin, J. (2009). Coordinated Ocean-ice Reference Experiments (COREs). *Ocean Model.*, 26(1-2):1–46.

Hahn, J., Brandt, P., Greatbatch, R. J., Krahmann, G., and Körtzinger, A. (2014). Oxygen variance and meridional oxygen supply in the Tropical North East Atlantic oxygen minimum zone. *Clim. Dyn.*, 43(11):2999–3024.

Hahn, J., Brandt, P., Schmidtko, S., and Krahmann, G. (2017). Decadal oxygen change in the eastern tropical North Atlantic. *Ocean Sci.*, 13(4):551–576.

Hazeleger, W. and Drijfhout, S. (2006). Subtropical cells and meridional overturning circulation pathways in the tropical Atlantic. *J. Geophys. Res. Ocean.*, 111(3):1–13.

He, Y. C., Drange, H., Gao, Y., and Bentsen, M. (2016). Simulated Atlantic Meridional Overturning Circulation in the 20th century with an ocean model forced by reanalysis-based atmospheric data sets. *Ocean Model.*, 100:31–48.

Helly, J. J. and Levin, L. A. (2004). Global distribution of naturally occurring marine hypoxia on continental margins. *Deep. Res. Part I Oceanogr. Res. Pap.*, 51(9):1159–1168.

Helm, K. P., Bindoff, N. L., and Church, J. A. (2011). Observed decreases in oxygen content of the global ocean. *Geophys. Res. Lett.*, 38(23):1–6.

Hsin, Y. C. and Qiu, B. (2012). Seasonal fluctuations of the surface North Equatorial Countercurrent (NECC) across the Pacific basin. *J. Geophys. Res. Ocean.*, 117(6):1–17.

Hua, B. L., Marin, F., and Schopp, R. (2003). Three-Dimensional Dynamics of the Subsurface Countercurrents and Equatorial Thermostad. Part II: Influence of the Large-Scale Ventilation and of Equatorial Winds. *J. Phys. Oceanogr.*, 33(i):2588–2609.

Hurrell, J. W. and Trenberth, K. E. (1998). Difficulties in obtaining reliable temperature trends: reconciling the surface and satellite microwave sounding unit records. *J. Clim.*, 11(5):945–967.

Hüttl, S. and Böning, C. W. (2006). Mechanisms of decadal variability in the shallow subtropical-tropical circulation of the Atlantic Ocean: A model study. *J. Geophys. Res. Ocean.*, 111(7):1–20.

Hüttl-Kabus, S. and Böning, C. W. (2008). Pathways and variability of the off-equatorial undercurrents in the Atlantic Ocean. *J. Geophys. Res. Ocean.*, 113(10):1–14.

Intergovernmental Panel on Climate Change (IPCC) (2013) (2014). *Climate Change 2013 - The Physical Science Basis*. Cambridge University Press, Cambridge.

Jansen, M. F., Dommenget, D., and Keenlyside, N. (2009). Tropical atmosphere - Ocean interactions in a conceptual framework. *J. Clim.*, 22(3):550–567.

Jochum, M. and Malanotte-Rizzoli, P. (2003). On the generation of North Brazil Current rings. *J. Mar. Res.*, 61(2):147–173.

Jochum, M. and Malanotte-Rizzoli, P. (2004). A New Theory for the Generation of the Equatorial Subsurface Countercurrents. *J. Phys. Oceanogr.*, 34(4):755–771.

Jochum, M., Malanotte-Rizzoli, P., and Busalacchi, A. (2004). Tropical instability waves in the Atlantic Ocean. *Ocean Model.*, 7(1-2):145–163.

Johnson, G. C. and Moore, D. W. (1997). The Pacific Subsurface Countercurrents and an Inertial Model*. *J. Phys. Oceanogr.*, 27(11):2448–2459.

Joyce, T. M., Frankignoul, C., Yang, J., and Phillips, H. E. (2004). Ocean Response and Feedback to the SST Dipole in the Tropical Atlantic*. *J. Phys. Oceanogr.*, 34(11):2525–2540.

Karstensen, J., Stramma, L., and Visbeck, M. (2008). Oxygen minimum zones in the eastern tropical Atlantic and Pacific oceans. *Prog. Oceanogr.*, 77(4):331–350.

Keenlyside, N. S. and Latif, M. (2007). Understanding equatorial atlantic interannual variability. *J. Clim.*, 20(1):131–142.

Kerr, R. A. (2000). A North Atlantic Climate Pacemaker for the Centuries. *Science (80-.).*, 288(5473):1984–1985.

Knight, J. R., Allan, R. J., Folland, C. K., Vellinga, M., and Mann, M. E. (2005). A signature of persistent natural thermohaline circulation cycles in observed climate. *Geophys. Res. Lett.*, 32(20):L20708.

Knight, J. R., Folland, C. K., and Scaife, A. A. (2006). Climate impacts of the Atlantic multidecadal oscillation. *Geophys. Res. Lett.*, 33(17):2–5.

Kock, A., Schafstall, J., Dengler, M., Brandt, P., and Bange, H. W. (2012). Sea-to-air and diapycnal nitrous oxide fluxes in the eastern tropical North Atlantic Ocean. *Biogeosciences*, 9(3):957–964.

Köllner, M., Visbeck, M., Tanhua, T., and Fischer, T. (2016). Diapycnal diffusivity in the core and oxycline of the tropical North Atlantic oxygen minimum zone. *J. Mar. Syst.*, 160:54–63.

Kopte, R., Brandt, P., Claus, M., Greatbatch, R. J., and Dengler, M. (2018). Role of Equatorial Basin-Mode Resonance for the Seasonal Variability of the Angola Current at 11S. *J. Phys. Oceanogr.*, 48(2):261–281.

Kriest, I., Khatiwala, S., and Oschlies, A. (2010). Towards an assessment of simple global marine biogeochemical models of different complexity. *Prog. Oceanogr.*, 86(3-4):337–360.

Kushnir, Y. (1994). Interdecadal Variations in North Atlantic Sea Surface Temperature and Associated Atmospheric Conditions. *J. Clim.*, 7(1):141–157.

Large, W. G. and Yeager, S. (2004). Diurnal to decadal global forcing for ocean and sea-ice models: The data sets and flux climatologies. Technical report, NCAR Technical Note NCAR/TN-460+STR,.

Latif, M., Böning, C., Willebrand, J., Biastoch, A., Dengg, J., Keenlyside, N., Schweckjendiek, U., and Madec, G. (2006). Is the thermohaline circulation changing? *J. Clim.*, 19(18):4631–4637.

Latif, M., Böning, C. W., Willebrand, J., Biastoch, A., Alvarez-Garcia, F., Keenlyside, N., and Pohlmann, H. (2007). Decadal to multidecadal variability of the Atlantic MOC: Mechanisms and predictability. pages 149–166.

Legeckis, R. (1977). Long Waves in the Eastern Equatorial Pacific Ocean: A View from a Geostationary Satellite. *Science (80-.).*, 197(4309):1179–1181.

Legeckis, R. and Reverdin, G. (1987). Long waves in the equatorial Atlantic Ocean during 1983. *J. Geophys. Res.*, 92(C3):2835.

Li, T. and Philander, S. G. (1997). On the seasonal cycle of the equatorial Atlantic Ocean. *J. Clim.*, 10(4):813–817.

Liu, C. and Wang, Z. (2014). On the response of the global subduction rate to global-warming in coupled climate models. *Adv. Atmos. Sci.*, 31(1):211–218.

Lozier, M. S. (2010). Deconstructing the conveyor belt. *Science (80-.).*, 328(5985):1507–1511.

Lozier, M. S., Li, F., Bacon, S., Bahr, F., Bower, A. S., Cunningham, S. A., de Jong, M. F., de Steur, L., DeYoung, B., Fischer, J., Gary, S. F., Greenan, B. J. W., Holliday, N. P., Houk, A., Houpert, L., Inall, M. E., Johns, W. E., Johnson, H. L., Johnson, C., Karstensen, J., Koman, G., Le Bras, I. A., Lin, X., Mackay, N., Marshall, D. P., Mercier, H., Oltmanns, M., Pickart, R. S., Ramsey, A. L., Rayner, D., Straneo, F., Thierry, V., Torres, D. J., Williams, R. G., Wilson, C., Yang, J., Yashayaev, I., and Zhao, J. (2019). A sea change in our view of overturning in the subpolar North Atlantic. *Science (80-.).*, 363(6426):516–521.

Lübbecke, J. F. and McPhaden, M. J. (2012). On the inconsistent relationship between Pacific and Atlantic Niños. *J. Clim.*, 25(12):4294–4303.

Lübbecke, J. F., Rodríguez-Fonseca, B., Richter, I., Martín-Rey, M., Losada, T., Polo, I., and Keenlyside, N. S. (2018). Equatorial Atlantic variability—Modes, mechanisms, and global teleconnections. *Wiley Interdiscip. Rev. Clim. Chang.*, 9(4):e527.

Luyten, J., Pedlosky, J., and Stommel, H. (1983). Climatic inferences from the ventilated thermocline. *Clim. Change*, 5(2):183–191.

Madec, G. (2008). *"NEMO ocean engine"*. 27, Inst. Pierre-Simon Laplace, Paris.

Marin, F., Hua, B. L., and Wacongne, S. (2000). The equatorial thermostad and subsurface countercurrents in the light of the dynamics of atmospheric Hadley cells. *J. Mar. Res.*, 58(3):405–437.

Marin, F., Schopp, R., and Hua, B. L. (2003). Three-dimensional dynamics of the subsurface countercurrents and equatorial thermostad. Part II: Influence of the large-scale ventilation and of equatorial winds. *J. Phys. Oceanogr.*, 33(12):2610–2626.

Martín-Rey, M., Polo, I., Rodríguez-Fonseca, B., Losada, T., and Lazar, A. (2018). Is there evidence of changes in tropical Atlantic variability modes under AMO phases in the observational record? *J. Clim.*, 31(2):515–536.

Matear, R. J. and Hirst, A. C. (2003). Long-term changes in dissolved oxygen concentrations in the ocean caused by protracted global warming. *Global Biogeochem. Cycles*, 17(4):1125.

Maximenko, N. A., Bang, B., and Sasaki, H. (2005). Observational evidence of alternating zonal jets in the world ocean. *Geophys. Res. Lett.*, 32(12):1–4.

McCreary, J. P. and Lu, P. (1994). Interaction between the subtropical and equatorial ocean circulations: The subtropical cell. *J. Phys. Oceanogr.*, 24:466–497.

McCreary, J. P., Lu, P., and Yu, Z. (2002). Dynamics of the Pacific Subsurface Countercurrents. *J. Phys. Oceanogr.*, 32:2379–2404.

Mélice, J. L. and Arnault, S. (2017). Investigation of the intra-annual variability of the north equatorial countercurrent/North Brazil current eddies and of the instability waves of the north tropical Atlantic Ocean using satellite altimetry and empirical mode decomposition. *J. Atmos. Ocean. Technol.*, 34(10):2295–2310.

Molinari, R. L., Bauer, S., Snowden, D., Johnson, G. C., Bourles, B., Gouriou, Y., and Mercier, H. (2003). A comparison of kinematic evidence for tropical cells in the Atlantic and Pacific oceans. *Elsevier Oceanogr. Ser.*, 68(C):269–286.

Montes, I., Dewitte, B., Gutknecht, E., Paulmier, A., Dadou, I., Oschlies, A., and Garçon, V. (2014). High-resolution modeling of the Eastern Tropical Pacific oxygen minimum zone: Sensitivity to the tropical oceanic circulation. *J. Geophys. Res. Ocean.*, 119(8):5515–5532.

Msadek, R. and Frankignoul, C. (2009). Atlantic multidecadal oceanic variability and its influence on the atmosphere in a climate model. *Clim. Dyn.*, 33(1):45–62.

Munk, W. H. (1950). On the Wind-Driven Ocean Circulation. *J. Meteorol.*, 7(2):80–93.

Nnamchi, H. C., Li, J., Kucharski, F., Kang, I.-S., Keenlyside, N. S., Chang, P., and Farneti, R. (2016). An Equatorial–Extratropical Dipole Structure of the Atlantic Niño. *J. Clim.*, 29(20):7295–7311.

Nobre, P. and Shukla, J. (1996). Variation of Sea surface Temperature, Wind Stress, and Rainfall over the Tropical Atlantic and South America. *J. Clim.*, 9(10):2464–2479.

Okumura, Y. and Xie, S. P. (2004). Interaction of the Atlantic equatorial cold tongue and the African monsoon. *J. Clim.*, 17(18):3589–3602.

Ollitrault, M. and Colin de Verdière, A. (2014). The Ocean General Circulation near 1000-m Depth. *J. Phys. Oceanogr.*, 44(1):384–409.

Oschlies, A., Brandt, P., Stramma, L., and Schmidtko, S. (2018). Drivers and mechanisms of ocean deoxygenation. *Nat. Geosci.*, 11(7):467–473.

Oschlies, A., Duteil, O., Getzlaff, J., Koeve, W., Landolfi, A., and Schmidtko, S. (2017). Patterns of deoxygenation: Sensitivity to natural and anthropogenic drivers. *Philos. Trans. R. Soc. A Math. Phys. Eng. Sci.*, 375(2102).

Paulmier, A. and Ruiz-Pino, D. (2009). Oxygen minimum zones (OMZs) in the modern ocean. *Prog. Oceanogr.*, 80(3-4):113–128.

Peña-Izquierdo, J., Van Sebille, E., Pelegrí, J. L., Sprintall, J., Mason, E., Llanillo, P. J., and Machín, F. (2015). Water mass pathways to the North Atlantic oxygen minimum zone. *J. Geophys. Res. Ocean.*, 120(5):3350–3372.

Perez, R. C., Hormann, V., Lumpkin, R., Brandt, P., Johns, W. E., Hernandez, F., Schmid, C., and Bourlès, B. (2014). Mean meridional currents in the central and eastern equatorial Atlantic. *Clim. Dyn.*, 43(11):2943–2962.

Perez, R. C., Lumpkin, R., Johns, W. E., Foltz, G. R., and Hormann, V. (2012). Interannual variations of Atlantic tropical instability waves. *J. Geophys. Res. Ocean.*, 117(C3):1–13.

Philander, S. G. H. (1978). Instabilities of zonal equatorial currents, 2. *J. Geophys. Res.*, 83(C7):3679.

Polo, I., Lazar, A., Rodriguez-Fonseca, B., and Mignot, J. (2015). Growth and decay of the equatorial Atlantic SST mode by means of closed heat budget in a coupled general circulation model. *Front. Earth Sci.*, 3.

Pozo Buil, M. and Di Lorenzo, E. (2017). Decadal dynamics and predictability of oxygen and subsurface tracers in the California Current System. *Geophys. Res. Lett.*, 44(9):4204–4213.

Qiu, B., Chen, S., and Sasaki, H. (2013). Generation of the North Equatorial Undercurrent Jets by Triad Baroclinic Rossby Wave Interactions. *J. Phys. Oceanogr.*, 43(12):2682–2698.

Richter, I., Behera, S. K., Masumoto, Y., Taguchi, B., Sasaki, H., and Yamagata, T. (2013). Multiple causes of interannual sea surface temperature variability in the equatorial Atlantic Ocean. *Nat. Geosci.*, 6(1):43–47.

Ridder, N. N. and England, M. H. (2014). Sensitivity of ocean oxygenation to variations in tropical zonal wind stress magnitude. *Global Biogeochem. Cycles*, 28(9):909–926.

Robson, J., Sutton, R., Lohmann, K., Smith, D., and Palmer, M. D. (2012). Causes of the Rapid Warming of the North Atlantic Ocean in the Mid-1990s. *J. Clim.*, 25(12):4116–4134.

Rosell-Fieschi, M., Pelegrí, J. L., and Gourrion, J. (2015). Zonal jets in the equatorial Atlantic Ocean. *Prog. Oceanogr.*, 130:1–18.

Rühs, S., Getzlaff, K., Durgadoo, J. V., Biastoch, A., and Böning, C. W. (2015). On the suitability of North Brazil Current transport estimates for monitoring basin-scale AMOC changes. *Geophys. Res. Lett.*, 42(19):8072–8080.

Schlesinger, M. E. and Ramankutty, N. (1994). An oscillation in the global climate system of period 65–70 years. *Nature*, 367(6465):723–726.

Schmidtko, S., Stramma, L., and Visbeck, M. (2017). Decline in global oceanic oxygen content during the past five decades. *Nature*, 542(7641):335–339.

Schott, F. A., Dengler, M., Brandt, P., Affler, K., Fischer, J., Bourlès, B., Gouriou, Y., Molinari, R. L., and Rhein, M. (2003). The zonal currents and transports at 35W in the tropical Atlantic. *Geophys. Res. Lett.*, 30(7):35–38.

Schott, F. A., McCreary Jr., J. P., and Johnson, G. C. (2004). Shallow Overturning Circulations of the Tropical-Subtropical Oceans. *Earth's Clim.*, 147:261–304.

Schott, F. A., Stramma, L., and Fischer, J. (1995). The warm water inflow into the western tropical Atlantic boundary regime , spring 1994. *J. Geophys. Res.*, 100(C12):24745 – 24760.

Semenov, V. A., Latif, M., Dommenget, D., Keenlyside, N. S., Strehz, A., Martin, T., and Park, W. (2010). The Impact of North Atlantic–Arctic Multidecadal Variability on Northern Hemisphere Surface Air Temperature. *J. Clim.*, 23(21):5668–5677.

Servain, J. (1991). Simple climatic indices for the tropical Atlantic Ocean and some applications. *J. Geophys. Res.*, 96(C8):15137.

Siedler, G., Zangenberg, N., Onken, R., and Morlière, A. (1992). Seasonal changes in the tropical Atlantic circulation: Observation and simulation of the Guinea Dome. *J. Geophys. Res.*, 97(C1):703.

Srokosz, M. A. and Bryden, H. L. (2015). Observing the Atlantic Meridional Overturning Circulation yields a decade of inevitable surprises. *Science (80-.).*, 348(6241).

Stommel, H. (1948). The westward intensification of wind-driven ocean currents. *Trans. Am. Geophys. Union*, 29(2):202.

Stramma, L., Brandt, P., Schafstall, J., Schott, F., Fischer, J., and Körtzinger, A. (2008a). Oxygen minimum zone in the North Atlantic south and east of the Cape Verde Islands. *J. Geophys. Res. Ocean.*, 113(4):1–15.

Stramma, L., Hüttl, S., and Schafstall, J. (2005). Water masses and currents in the upper tropical northeast Atlantic off northwest Africa. *J. Geophys. Res. Ocean.*, 110(12):1–18.

Stramma, L., Johnson, G. C., Sprintall, J., and Mohrholz, V. (2008b). Expanding oxygen-minimum zones in the tropical oceans. *Science (80-.).*, 320(5876):655–658.

Stramma, L., Oschlies, A., and Schmidtko, S. (2012). Mismatch between observed and modeled trends in dissolved upper-ocean oxygen over the last 50 yr. *Biogeosciences*, 9(10):4045–4057.

Stramma, L., Schmidtko, S., Levin, L. A., and Johnson, G. C. (2010). Ocean oxygen minima expansions and their biological impacts. *Deep. Res. Part I Oceanogr. Res. Pap.*, 57(4):587–595.

Sverdrup, H. U. (1947). Wind-Driven Currents in a Baroclinic Ocean; with Application to the Equatorial Currents of the Eastern Pacific. *Proc. Natl. Acad. Sci.*, 33(11):318–326.

Thierry, V., Treguier, A. M., and Mercier, H. (2004). Numerical study of the annual and semi-annual fluctuations in the deep equatorial Atlantic Ocean. *Ocean Model.*, 6(1):1–30.

Trenberth, K. E. and Shea, D. J. (2006). Atlantic hurricanes and natural variability in 2005. *Geophys. Res. Lett.*, 33(12):1–4.

Tsujino, H., Urakawa, S., Nakano, H., Small, R. J., Kim, W. M., Yeager, S. G., Danabasoglu, G., Suzuki, T., Bamber, J. L., Bentsen, M., Böning, C. W., Bozec, A., Chassignet, E. P., Curchitser, E., Boeira Dias, F., Durack, P. J., Griffies, S. M., Harada, Y., Ilicak, M., Josey, S. A., Kobayashi, C., Kobayashi, S., Komuro, Y., Large, W. G., Le Sommer, J., Marsland, S. J., Masina, S., Scheinert, M., Tomita, H., Valdivieso, M., and Yamazaki, D. (2018). JRA-55 based surface dataset for driving ocean–sea-ice models (JRA55-do). *Ocean Model.*, 130:79–139.

Tuchen, F. P., Brandt, P., Claus, M., and Hummels, R. (2018). Deep Intraseasonal Variability in the Central Equatorial Atlantic. *J. Phys. Oceanogr.*, 48(12):2851–2865.

Urbano, D. F., De Almeida, R. A., and Nobre, P. (2008). Equatorial undercurrent and North equatorial countercurrent at 38W: A new perspective from direct velocity data. *J. Geophys. Res. Ocean.*, 113(4):1–16.

Vagner, M., Lefrançois, C., Ferrari, R. S., Satta, A., and Domenici, P. (2008). The effect of acute hypoxia on swimming stamina at optimal swimming speed in flathead grey mullet Mugil cephalus. *Mar. Biol.*, 155(2):183–190.

Vergara, O., Dewitte, B., Montes, I., Garçon, V., Ramos, M., and Pizarro, O. (2016). Seasonal variability of the oxygen minimum zone off Peru in a high-resolution regional coupled model. *Biogeosciences*, 13(15):4389–4410.

Visbeck, M. (2002). Deep velocity profiling using lowered acoustic Doppler current profilers: Bottom track and inverse solutions. *J. Atmos. Ocean. Technol.*, 19(5):794–807.

von Schuckmann, K., Brandt, P., and Eden, C. (2008). Generation of tropical instability waves in the Atlantic Ocean. *J. Geophys. Res. Ocean.*, 113(C08034):1–12.

Wang, C. (2005). Subthermocline tropical cells and equatorial subsurface countercurrents. *Deep. Res. Part I Oceanogr. Res. Pap.*, 52(1):123–135.

Weisberg, R. H. and Weingartner, T. J. (1988). Instability Waves in the Equatorial Atlantic Ocean. *J. Phys. Oceanogr.*, 18(11):1641–1657.

Xie, S. and Carton, J. (2004). Tropical Atlantic variability: Patterns, mechanisms, and impacts. *Geophys. Monogr. Ser.*, 147:121–142.

Yan, X., Zhang, R., and Knutson, T. R. (2019). A multivariate AMV index and associated discrepancies between observed and CMIP5 externally forced AMV. *Geophys. Res. Lett.*, page 2019GL082787.

Yang, S., Gruber, N., Long, M. C., and Vogt, M. (2017). ENSO-Driven Variability of Denitrification and Suboxia in the Eastern Tropical Pacific Ocean. *Global Biogeochem. Cycles*, 31(10):1470–1487.

Zebiak, S. E. (1993). Air-sea interaction in the equatorial Atlantic region. *J. Clim.*, 6(8):1567–1586.

Zhang, D., McPhaden, M. J., and Johns, W. E. (2003). Observational Evidence for Flow between the Subtropical and Tropical Atlantic: The Atlantic Subtropical Cells. *J. Phys. Oceanogr.*, 33(8):1783–1797.

Zhang, R. (2017). On the persistence and coherence of subpolar sea surface temperature and salinity anomalies associated with the Atlantic multidecadal variability. *Geophys. Res. Lett.*, 44(15):7865–7875.

Zhang, R. and Delworth, T. L. (2006). Impact of Atlantic multidecadal oscillations on India/Sahel rainfall and Atlantic hurricanes. *Geophys. Res. Lett.*, 33(17):L17712.

Zhang, R., Delworth, T. L., and Held, I. M. (2007). Can the Atlantic Ocean drive the observed multidecadal variability in Northern Hemisphere mean temperature? *Geophys. Res. Lett.*, 34(2):L02709.

Zhu, X., Greatbatch, R. J., and Claus, M. (2017). Interannual variability of tropical Pacific sea level from 1993 to 2014. *J. Geophys. Res. Ocean.*, 122(1):602–616.

Acknowledgments

Zuerst möchte ich mich bei Joke F. Lübbecke bedanken. Für ihre Geduld und Unterstützung in den letzten Jahren sowohl bei der wissenschaftlichen Arbeit, als auch bei all den anderen Aktivitäten im Rahmen meiner Rolle als Doktorandenvertretung. Sie war stets eine aufmerksame und verlässliche Betreuerin, die gerne ihr Fachwissen teilte und mir aufmunternd und mit Rat zur Seite stand.

Des Weiteren möchte ich Peter Brandt für seine Hilfsbereitschaft und die zahlreichen fachlichen Diskussionen danken, angefangen bei der Hilfe ein einfaches Strömungsfeld zu modellieren bis hin zum Erkläutern komplexer Zusammenhänge im Ozean.

Vielen Dank auch an Richard Greatbatch und Martin Claus, die mir während meiner ISOS Komitee Treffen mit Rat zur Seite standen. Insbesondere an Martin Claus für die langen Diskussionen über mögliche Antriebsmechanismen der Variabilität des nördlichen äquatorialen Unterstroms.

Vielen Dank auch an alle Wissenschaftler, insbesondere Markus Dengler, und den Technikern der Arbeitsgruppe, die ihr Wissen über Ozeanbeobachtungen bereitwillig teilten und die Ausfahrten zu lehrreichen und einzigartigen Erlebnissen machten.

Ein großes Dankeschön geht an meine Freunde und Kollegen aus der PO, ohne die meine Doktorandenzeit nur halb so schön und lustig gewesen wäre. Danke für die fachlichen und nicht ganz so fachlichen Diskussionen, das Last-Minute-Korrekturlesen, und alles andere: Flo, Robert, FPT, Jan, Johannes H., Rebecca, Tim, Paddel und Fine. Danke an Franziska und Christina für die Tipps bei der Verwendung von Ozeanmodelldaten. Vielen Dank Daniela, für die schönen Mittagspausen auf der Dachterrasse. Auch vielen Dank ans ehemalige DokTeam für die gemeinsame Zeit bei den Helmholtz Juniors und die gemeinsamen Aktionen.

Ich möchte mich auch bei der "Kieler Gruppe", meinen Freunden aus dem Studium, für die seelische und moralische Unterstützung bedanken. Ein besonderer Dank geht an Annika und Daniel. An Annika für die stetige Motivation trotz aller Höhen und Tiefen, die so eine beste Freundschaft mit sich bringt. Und an Daniel für sprachliche Korrekturen sowie emotionale Unterstützung und Nervenkraft.

Zum Schluss möchte ich meiner Familie danken. Dafür, dass sie sind wie sie sind und für ihre zuverlässige Unterstützung egal wo man sich aufhält. Solch eine Unterstützung und solch ein starker Zusammenhalt sind nicht selbstverständlich. Ein besonderer Dank an meine Schwestern, Jana und Alexa, für die sprachlichen Korrekturen und an meine Eltern, die mich immer auf allen Wegen bedingungslos unterstützt haben.

Declaration

I hereby declare that this work is my own work apart from my supervisors' guidance and acknowledged assistance. This thesis has not been submitted for a degree to any other examining body. This thesis was prepared in accordance with the Rules of Good Scientific Practice of the German Research Foundation. An academic degree has never been withdrawn from me.

Kiel, June 2019, _____

(Kristin Burmeister)